Title
Nanoscale metals and semiconductors for the storage of solar energy in chemical bonds

Author
Manthiram, Karthish

Publication Date
2015

Peer reviewed|Thesis/dissertation

Nanoscale metals and semiconductors for the storage of solar energy in chemical bonds

By

Karthish Manthiram

A dissertation submitted in partial satisfaction of the

requirements for the degree of

Doctor of Philosophy

in

Chemical Engineering

in the

Graduate Division

Of the

University of California, Berkeley

Committee in charge:

Professor A. Paul Alivisatos, Co-Chair
Professor Roya Maboudian, Co-Chair
Professor Nitash Balsara
Professor Tanja Cuk

Summer 2015

Nanoscale metals and semiconductors for the storage of solar energy in chemical bonds

By

Karthish Manthiram

Abstract

Nanoscale metals and semiconductors for the storage of solar energy in chemical bonds

By

Karthish Manthiram

Doctor of Philosophy in Chemical Engineering

University of California, Berkeley

Professor A. Paul Alivisatos, Co-Chair

Professor Roya Maboudian, Co-Chair

The transduction of electrical energy into chemical bonds represents one potential strategy for storing energy derived from intermittent sources such as solar and wind. Driving the electrochemical reduction of carbon dioxide using light requires (1) developing light absorbers which convert photons into electron-hole pairs and (2) catalysts which utilize these electrons and holes to reduce carbon dioxide and oxidize water, respectively. For both the light absorbers and catalysts, the use of nanoscale particles is advantageous, as charge transport length scales are minimized in the case of nanoscale light absorbers and catalytic surface-area-to-volume ratio is maximized for nanoscale catalysts. In many cases, although semiconductors and metals in the form of thin films and foils are increasingly well-characterized as photoabsorbers and electrocatalysts for carbon dioxide reduction, respectively, the properties of their nanoscale counterparts remain poorly understood.

This dissertation explores the nature of the light absorption mode of non-stoichiometric semiconductors which are utilized as light absorbers and the development of catalysts with enhanced stability, activity, and selectivity for carbon dioxide reduction. Chapter 1 provides an overview of the state of development of methods of transducing the energy of photons into chemical bonds.

Chapters 2 and 3 investigate the development of stable, active, and selective catalysts for the electrochemical reduction of carbon dioxide. Chapter 2 examines how copper nanoparticles have enhanced activities and selectivities for methanation compared to copper foils. Chapter 3 focuses on the development of strategies to stabilize high-surface-area catalysts to prevent surface area loss during electrochemical carbon dioxide reduction.

Chapters 4 and 5 entail a fundamental understanding of the light absorption mode of nanoscale photoabsorbers used in both photoelectrochemical cells and in photovoltaics. Chapter 4 focuses on the nature of the light absorption mode of non-stoichiometric tungsten oxide, a material which has been explored as a photoanode for the photon driven

oxidation of water. Chapter 5 examines the tunability of the light absorption mode of nanoscale copper sulfide, a material which has been explored as a photoabsorber for photovoltaics. An understanding of the light absorption mode of non-stoichiometric oxides and sulfides at the nanoscale is critical for the use of these materials in redox active environments.

Dedicated to my loving parents and sister.

Table of Contents

List of Figures

List of Tables

Acknowledgements

My adviser has always reminded us that graduate school is a very personal journey in which we each make discoveries that lead to our personal development. I cannot imagine a better guide on this journey than my own adviser. Paul places an enormous amount of trust in every graduate student by treating us as colleagues in full, providing each of us with the intellectual freedom and space that we need to grow on this journey. While giving us this freedom, he still continues to invest significant time into each student to assist them in learning how to ask the right questions. He has a rare style of patient curiosity and a unique ability to drive Socratic dialogue that I can only strive to emulate.

I have much gratitude for my committee members Roya Maboudian, Nitash Balsara, and Tanja Cuk, who have always made themselves available and engaged with me in many scientific discussions. Several of my mentors have gone far beyond what anyone could expect of any mentor to help me on this journey. Yi Cui taught me the power of sharing one's enthusiasm for science – we do our best work when we are happy. Prashant Jain showed me how to break down a complex problem into simple, addressable questions that can be tackled day-to-day. Yogi Surendranath shared with me his love for electrochemistry and displayed an inquisitiveness that drove all around him to be more discerning scientists. Rachel Segalman showed me that making an investment of time in developing one's scientific talent requires an investment in them as a person.

The Alivisatos group has a wonderful, collaborative environment that I benefited from enormously. I would like to thank our group administrator Negest Williams for all her support and for promptly taking care of all our questions and concerns; we are truly lucky to have an administrator who cares so deeply about the well-being of the group.

During nearly the past decade in the Bay Area, I have had the fortune of making several friends that are like family. In addition to several of the mentors I mentioned above, I would especially like to thank Brandon Beberwyck, Anton Dam, Khang Dinh, Danny Hellebusch, Boris Russ, and Genia Vogman for their support and thoughtfulness as friends. They epitomize what it means to be selfless in friendship.

My parents and sister have done more to mold me than anyone else. My mom has an unparalleled ability to make all around her feel cherished and precious. My mom taught me the joy of working with my hands and we have always made a great team for building new things. My mom and dad showed me by example that one's intrinsic skills mean little without clarity of mind and an ability to get things done through hard work. My dad taught me the importance of freedom of thought and how important it is to love what you do everyday such that it blurs the lines of work and hobby. My sister, who is rare in how much she cared for me as a little brother, taught me the joy of imparting knowledge and engaging in creative thought. From a young age, she enthusiastically taught me a wide range of subjects and invented exciting games for us to play. I am lucky that the three people that I most want to be like I have had at my side since I was born: my mom, dad, and sister. I hope that I can give back to them even a small amount of the joy of living they have given me.

Chapter 1.

Introduction: Synthesis of fuels and feedstocks using solar energy

The solar-driven electrochemical synthesis of hydrocarbons fuels and chemical feedstocks from carbon dioxide represents one potential strategy for mitigating carbon dioxide emissions. This strategy can allow for the utilization of existing infrastructure for the distribution and consumption of electrosynthesized products. We provide an overview of the projected need for mitigating carbon dioxide emissions, reactions involved in chemically reducing carbon dioxide via thermochemical and electrochemical routes, and strategies for driving electrochemical CO_2 reduction via solar energy, through integrated photoelectrochemical cells and photovoltaics linked to electrolyzers. We conclude with an overview of the challenges addressed in this dissertation, including (1) understanding the stability, selectivity, and activity of nanoscale metals used to catalyze electrochemical CO_2 reduction and (2) understanding the light absorption modes of non-stoichiometric semiconductors used in photoelectrochemical cells and photovoltaics.

1.1. Mitigating carbon dioxide emissions

Even with increasing use of energy sources which do not emit carbon dioxide in the United States, it is projected that use of carbon dioxide emitting sources of energy will continue to increase in the decades to come (Figure 1.1). At present, approximately 80 quadrillion BTUs of domestic energy consumption are from carbon dioxide emitting sources, such as natural gas, coal, and petroleum, while only 16 quadrillion BTUs are from sources which do not emit carbon dioxide, including biofuels, solar, and wind; by 2040, it is projected that these numbers will increase to 86 and 20 quadrillion BTUs, respectively.[1] In large part, the increased use of energy sources which emit carbon dioxide is driven by improved domestic availability of natural gas.

Hence, even with increasing penetration of clean energy sources, there will still be a need to contend with significant CO_2 generation, which will contribute to global warming if emitted.[2] There are numerous strategies that one may consider to prevent generated CO_2 from being emitted, which generally fall into two categories: (1) methods of effectively removing the carbon dioxide from the global carbon cycle and (2) methods of closing the carbon cycle by converting the carbon dioxide into fuels. The former could involve sequestration of carbon dioxide by injection into underground reservoirs[3] or chemical conversion of carbon dioxide into plastics such as polyethylene. The latter could involve chemical conversion of carbon dioxide into hydrocarbon fuels, which when later burned, emit carbon dioxide that was originally captured. The chemical conversion of carbon dioxide[4] is attractive because if done in an efficient manner, it could present a route to mitigate CO_2 emissions while producing useful products.

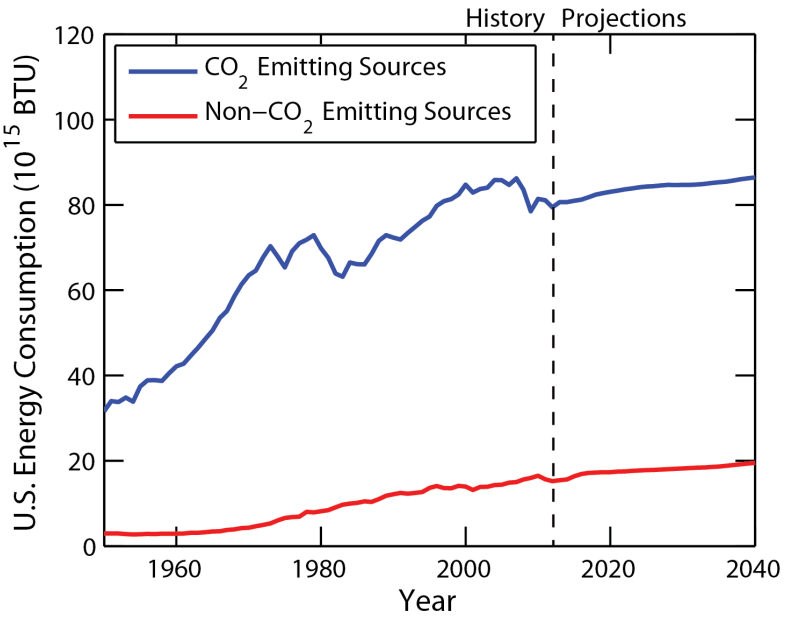

Figure 1.1. Historical and projected United States energy consumption. Energy consumption is categorized based on whether it is from CO_2 emitting sources or non-CO_2 emitting sources, using data tabulated by the Energy Information Administration.[1]

1.2. Chemical reactions involved in the reduction of carbon dioxide

There are a variety of thermochemical routes for reducing carbon dioxide, including the reverse water-gas shift for reducing CO_2 to CO and the Sabatier process for reducing CO_2 to methane. The reverse water-gas shift reaction involves reacting carbon dioxide and hydrogen over a copper on alumina catalyst at temperatures above 500 K:

$$CO_2 + H_2 \rightarrow CO + H_2O \qquad (1.1)$$

The generated CO can then be utilized for the synthesis of a wide range of industrial feedstocks, including alcohols, aldehydes, and hydrocarbons. Alternatively, the CO_2 may also be thermochemically reduced to more reduced products, such as methane. The Sabatier process[5] involves thermochemical reduction of carbon dioxide using hydrogen over a nickel catalyst at temperatures above 550 K to generate methane:

$$CO_2 + 4\ H_2 \rightarrow CH_4 + 2\ H_2O \qquad (1.2)$$

The vast majority of hydrogen is currently derived from steam reforming of methane (eq. 1.3) and the water-gas shift reaction[6] (eq. 1.4):

$$CH_4 + H_2O \rightarrow CO + 3H_2 \qquad (1.3)$$

$$CO + H_2O \rightarrow CO_2 + H_2 \qquad (1.4)$$

If hydrogen derived from the above process were used for CO_2 reduction, this would defeat the purpose of mitigating CO_2 emissions since there is no useful net conversion. Instead, it is necessary to produce the hydrogen through splitting water, which can be achieved via thermochemical and electrochemical routes.[7] Electrochemical routes are appealing because they can be conducted at low temperatures that impose less severe materials requirements compared to thermochemical routes.

The electrochemical water splitting reaction consists of two half-reactions: oxygen evolution (eq. 1.5) and hydrogen evolution (eq. 1.6). The overall reaction (eq. 1.7) requires input of 237 kJ/mol of water.[8]

$$H_2O \rightarrow \frac{1}{2} O_2 + 2e^- + 2H^+ \quad (1.5)$$

$$2H^+ + 2e^- \rightarrow H_2 \quad (1.6)$$

$$H_2O \rightarrow H_2 + \frac{1}{2} O_2 \quad (1.7)$$

This two-step process involving electrochemical generation of hydrogen followed by thermochemical reduction of CO_2 to CH_4 in the Sabatier process is practiced at a pilot plant in Germany at the 6 MW scale.[9] An alternative to the two-step route described above is to directly, electrochemically reduce the carbon dioxide at the surface of an electrode, to products such as CO (eq. 1.8) and CH_4 (eq. 1.9):

$$CO_2 + 2e^- + 2H^+ \rightarrow CO + H_2O \quad (1.8)$$

$$CO_2 + 8e^- + 8H^+ \rightarrow CH_4 + 2H_2O \quad (1.9)$$

These cathodic reactions are coupled to the oxygen evolution reaction (eq. 1.5) at the anode. The direct electrochemical reduction of carbon dioxide is of interest because fewer unit operations are required compared to the two-step process.

Of the various target products, it may appear that methane is the least attractive given the increased domestic availability of natural gas.[1] Methane is the simplest hydrocarbon product; once an understanding of routes which can lead to its efficient synthesis are developed, then routes to more complex, energy-dense fuels can be devised. In addition, if methane does eventually become the energy carrier of choice, there exists significant infrastructure for the distribution and consumption of natural gas.

1.3. Light harvesting for solar-driven chemical conversion of carbon dioxide

Because the conversion of carbon dioxide into fuels is thermodynamically uphill, input of energy is required. Since the core motivation for this conversion is the mitigation of carbon dioxide emissions, it is essential that the process be driven by a source of energy which does not lead to carbon dioxide emissions, such as solar. Nature has developed

robust reaction pathways, collectively known as photosynthesis, for storing the energy delivered by sunlight in chemical fuels. The simplest inorganic analogue of photosynthesis is a semiconductor which absorbs sunlight to generate electron-hole pairs that are consumed by two electrochemical half reactions to form a fuel of interest.[10] The light absorption process and the electrochemical reactions may either be integrated on a single device, known as a photoelectrochemical cell, or conducted on separate devices, with a photovoltaic cell connected to an electrolyzer.[11]

A photoelectrochemical cell conducts both the light absorption and electrochemical fuel synthesis processes. The two half reactions may be driven by the same semiconductor if the valence and conduction bands are sufficiently oxidizing and reducing, respectively. However, this has the consequence that the bandgap must be very large, leading to poor absorption of visible light. To overcome this limitation, the two half reactions are often conducted on separate semiconductors referred to as the photoanode, where the oxidation reaction occurs, and the photocathode, where the reduction reaction occurs (Figure 1.2).[12]

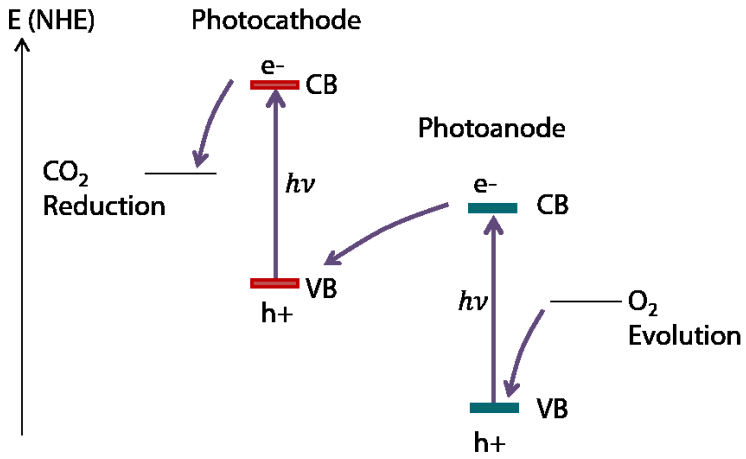

Figure 1.2. **Motion of charge carriers in a photoelectrochemical cell.** Both the photoanode and photocathode each absorb a photon ($h\nu$), leading to the generation of two electron-hole (e^--h+) pairs. The conduction band (CB) electron in the photoanode is annihilated by the valence band (VB) hole in the photocathode. The hole in the photoanode and electron in the photocathode participate in the electrochemical half reactions of interest.

An alternative approach is to utilize separate photovoltaic cells and electrolyzers (Figure 1.3).[13] In this method, electricity generation and fuel synthesis occur in separate devices which alleviate many of the concurrent materials constraints that exist in an integrated photoelectrochemical device. In addition, the power may be conditioned between the photovoltaic and the electrolyzer to achieve the current and potential which provide the desired selectivity for the electrochemical process.

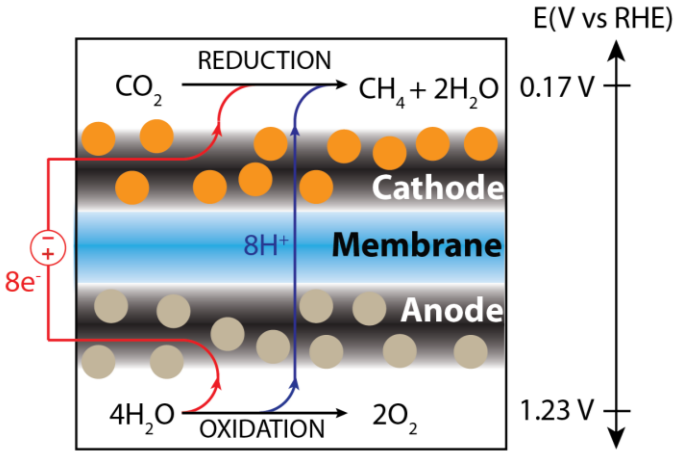

Figure 1.3. Electrolyzer for converting water and carbon dioxide into methane and oxygen. The electrolyzer contains a membrane electrode assembly, consisting of an anode and cathode on either side of a membrane. Water is oxidized at the anode, liberating protons, which traverse the membrane, and electrons, which pass through the external circuit and are raised in chemical potential by a potentiostat. The electrons and protons react with CO_2 at the cathode, producing methane and water. The thermodynamic potential difference for the anodic and cathodic reactions is 1.06 V, leading to storage of 818 kJ/mol of methane.

1.4. Challenges associated with solar-driven electrochemical reduction of carbon dioxide

In this dissertation, we address challenges associated both with the development of (1) nanoscale metals for electrochemical CO_2 reduction and (2) light absorbers for photoelectrochemical cells and photovoltaics.

1.4.1. Activity, selectivity, and stability of nanoscale metals for electrochemical carbon dioxide reduction

The vast majority of research on electrochemical carbon dioxide reduction has been conducted on foil cathodes, leading to in-depth understanding of their product distributions (Figure 1.4).[14–16] Because CO_2 is electrochemically reduced from an aqueous solution that serves as the source of protons, hydrogen evolution is a competing reaction at the potentials at which CO_2 reduction occurs. For this reason, metals which have relatively low hydrogen evolution reaction overpotentials and high adsorbate binding energies, such as titanium, iron, nickel, and platinum, predominantly evolve hydrogen and very little CO_2 is reduced at their surface; the small amount of CO_2 that is reduced at their surface is converted to CO which poisons many of the active sites.[17] On the other hand, metals with high hydrogen evolution reaction overpotential and low adsorbate binding energies, such as cadmium, indium, tin, mercury, tantalum, lead, and bismuth, are effective at outer-sphere reduction of carbon dioxide to produce formic acid. Metals with intermediate hydrogen evolution reaction overpotentials and adsorbate

binding energies, such as zinc, gallium, palladium, silver, and gold, reduce CO_2 to CO; the CO is bound strongly enough that it is stabilized as a product but weakly enough that it desorbs rather than being further reduced. Copper has a slightly higher CO binding enthalpy compared to these metals that evolve CO as a terminal product, such that the CO is also further reduced; the product distribution is a mixture of CO, CH_4, C_2H_4, $HCOO^-$, and H_2.[17]

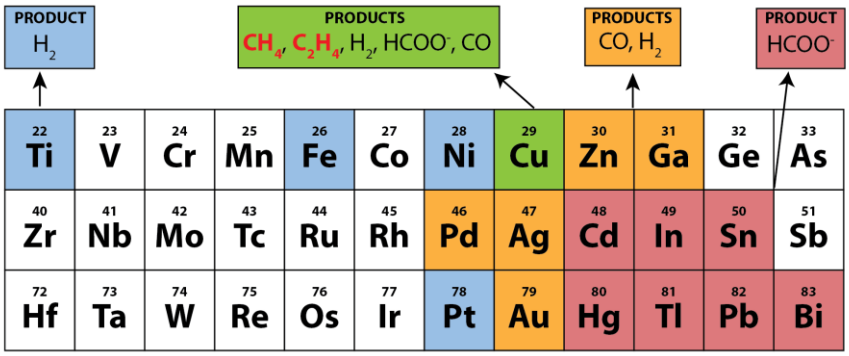

Figure 1.4. Product distribution of various metal foils for electrochemical CO_2 reduction. Copper is unique in its ability to produce hydrocarbon products but with poor selectivity for any single product.[14]

Although foils are a useful architecture for benchmarking a wide range of metals, practical electrolyzers require dispersible, high surface area catalysts; the high surface areas enable high current densities per unit geometric area and the use of a dispersible material allows for the catalyst to be incorporated into a gas-diffusion-layer and deposited on either side of a membrane in order to minimize the ionic resistance (Figure 1.5).[18,19] In a gas diffusion layer, it is difficult to deconvolute kinetic and transport limitations since the catalysts are embedded within an electrically and ionically conductive matrix. As a result, we utilize a model system for dispersible catalysts in which the catalysts are deposited in a monolayer on the surface of a glassy carbon electrode, which provides a uniformly accessible catalytic surface.

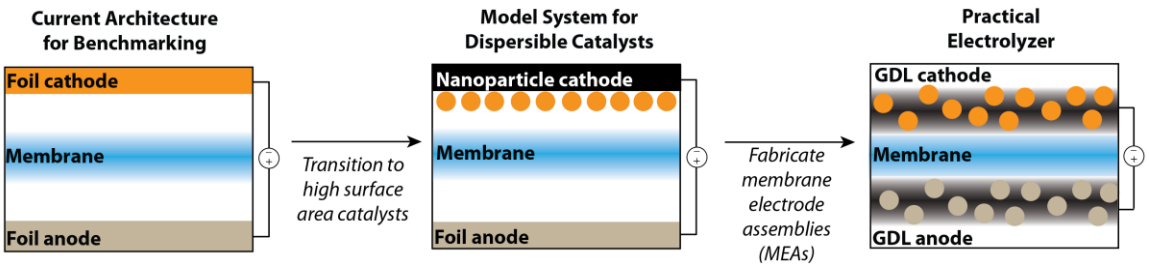

Figure 1.5. Architectures for electrolyzers. Transitioning from foil based electrodes to high surface area, dispersible catalysts incorporated into a membrane electrode assembly, will enable high current densities and minimize ionic resistance.

In Chapter 2, we investigate how the activity and selectivity of copper nanoparticles differ from copper foils for electrochemical carbon dioxide reduction. In Chapter 3, we study the stability of gold nanoparticles during electrochemical CO_2 reduction and develop a mechanism to explain how gold nanoparticles lose surface area during electrochemical CO_2 reduction. Altogether, these studies represent a first step towards integrating highly dispersed catalysts into practical electrolyzers for CO_2 reduction.

1.4.2. Impact of non-stoichiometry of semiconductors used in photoelectrochemical cells and photovoltaics on their light absorption properties

Despite the apparent simplicity of the inorganic photocatalytic scheme (Figure 1.2), nature's photosynthetic scheme excels as a method of energy harvesting because of its scalability and operational robustness.[20] Current inorganic schemes are not scalable due to high costs, as particular materials exhibit either poor photostability, contain expensive raw materials, or are inefficient. The vast majority of investigations of photocatalysts have been conducted on transition-metal oxides (TMOs), as many TMOs exhibit excellent photostability.[21] However, TMOs tend to have large bandgaps which limit visible light absorption, leading to low external quantum efficiency.[22] For instance, the first material identified for semiconductor photocatalysis, TiO_2, has excellent photostability and can be produced cheaply, but it has a very low external quantum efficiency for conversion of sunlight into a chemical fuel because it has a large bandgap (3.2 eV) which limits visible light absorption.[23] Like TiO_2, $WO_{3-\delta}$ also exhibits excellent photostability and can be produced cheaply but is unusual among transition metal oxides for its smaller bandgap (2.6 eV – 3 eV, depending on the oxygen stoichiometry δ) which improves visible light absorption.[24] The valence band position of $WO_{3-\delta}$ is sufficiently oxidizing that a catalyst is generally not necessary to enhance the rate of the oxygen evolution reaction on a bare $WO_{3-\delta}$ surface, while the conduction band position of $WO_{3-\delta}$ is not reducing enough for the hydrogen evolution reaction. As a result, $WO_{3-\delta}$ is employed as a photoanode and must be combined with a photocathode for overall water splitting.[25] One of the key shortcomings of tungsten oxide as a photoanode is that it is a weak light absorber, such that thick layers are necessary for significant light absorption. In Chapter 4, we investigate the light absorption mode of oxygen deficient phases of

tungsten oxide to understand how oxygen deficiency impacts the light absorption properties.

Non-stoichiometry also impacts the light absorption properties of semiconductors employed in photovoltaic cells. Copper chalcogenides have been extensively explored as light absorbers,[26,27] and these materials can experience copper deficiency due to the tendency for copper to be extracted from the host lattice. In Chapter 5, we explore how chemical reductants and oxidants can be used to insert and extract copper from copper sulfide and how this impacts the light absorption mode and electrical properties of this material.

1.5. References

(1) *Annual Energy Outlook 2014*; Energy Information Agency: Washington, DC, 2014.

(2) *Climate Change 2013: The Physical Science Basis*; 2013.

(3) *IPCC Special Report on Carbon Dioxide Capture and Storage*; Metz, B.; Davidson, O.; Coninck, H.; Loos, M.; Meyer, L., Eds.; Cambridge University Press: Cambridge, 2005.

(4) Appel, A. M.; Bercaw, J. E.; Bocarsly, A. B.; Dobbek, H.; Dubois, D. L.; Dupuis, M.; Ferry, J. G.; Fujita, E.; Hille, R.; Kenis, P. J. A.; Kerfeld, C. A.; Morris, R. H.; Peden, C. H. F.; Portis, A. R.; Ragsdale, S. W.; Rauchfuss, T. B.; Reek, J. N. H.; Seefeldt, L. C.; Thauer, R. K.; Waldrop, G. L. *Chem. Rev.* **2013**, *113*, 6621.

(5) Sabatier, P.; Senderens, J. B. *C. R. Acad. Sci.* **1902**, *134*, 689.

(6) Ratnasamy, C.; Wagner, J. P. *Catal. Rev.* **2009**, *51*, 325.

(7) Grimes, C. A.; Varghese, O. K.; Ranjan, S. In *Light, Water, Hydrogen*; Springer: New York, 2008; pp. 35–113.

(8) Amouyal, E. *Sol. Energy Mater. Sol. Cells* **1995**, *38*, 249.

(9) Schiebahn, S.; Grube, T.; Robinus, M.; Zhao, L.; Otto, A.; Kumar, B.; Weber, M.; Stolten, D. In *Transition to Renewable Energy Systems*; Stolten, D.; Scherer, V., Eds.; Wiley: Weinheim, Germany, 2013; pp. 813–847.

(10) Tan, M. X.; Laibinis, P. E.; Nguyen, S. T.; Kesselman, J. M.; Stanton, C. E.; Lewis, N. S. *Prog. Inorg. Chemisry* **1994**, *41*, 21.

(11) Jacobsson, T. J.; Fjällström, V.; Edoff, M.; Edvinsson, T. *Energy Environ. Sci.* **2014**, *7*, 2056.

(12) Somorjai, G. A.; Turner, J. E. *Naturwissenschaften* **1984**, *71*, 575.

(13) Winkler, M. T.; Cox, C. R.; Nocera, D. G.; Buonassisi, T. *Proc. Natl. Acad. Sci.* **2013**, *110*, E1076.

(14) Hori, Y.; Wakebe, H.; Tsukamoto, T.; Koga, O. *Electrochim. Acta* **1994**, *39*, 1833.

(15) Hori, Y.; Kikuchi, K.; Suzuki, S. *Chem. Lett.* **1985**, *11*, 1695.

(16) Kuhl, K. P.; Hatsukade, T.; Cave, E. R.; Abram, D. N.; Kibsgaard, J.; Jaramillo, T. F. *J. Am. Chem. Soc.* **2014**, *136*, 14107.

(17) Hori, Y. In *Modern Aspects of Electrochemistry*; Vayenas, C. G.; White, R. E.; Gamboa-Aldeco, M. E., Eds.; Springer: New York, 2008; pp. 89–189.

(18) Weidner, J. W.; Sethuraman, V. A.; Van Zee, J. W. *Interface* **2003**, *12*, 40.

(19) Zhu, W.; Michalsky, R.; Metin, O.; Lv, H.; Guo, S.; Wright, C. J.; Sun, X.; Peterson, A. A.; Sun, S. *J. Am. Chem. Soc.* **2013**, *135*, 16833.

(20) Singhal, G. S.; Renger, G.; Sopory, S. K.; Irrgang, K. D. *Concepts in Photobiology*; Kluwer: Boston, 1999.

(21) Walter, M. G.; Warren, E. L.; McKone, J. R.; Boettcher, S. W.; Mi, Q.; Santori, E. A.; Lewis, N. S. *Chem. Rev.* **2010**, *110*, 6446.

(22) Chen, X.; Shen, S.; Guo, L.; Mao, S. S. *Chem. Rev.* **2010**, *110*, 6503.

(23) Fujishima, A.; Honda, K. *Nature* **1972**, *238*, 37.

(24) Hodes, G.; Cahen, D.; Manassen, J. *Nature* **1976**, *260*, 312.

(25) Hu, C. C.; Nian, J. N.; Teng, H. *Sol. Energy Mater. Sol. Cells* **2008**, *92*, 1071.

(26) Guo, Q.; Ford, G. M.; Yang, W. C.; Walker, B. C.; Stach, E. A.; Hillhouse, H. W.; Agrawal, R. *J. Am. Chem. Soc.* **2010**, *132*, 17384.

(27) Todorov, T. K.; Reuter, K. B.; Mitzi, D. B. *Adv. Mater.* **2010**, *22*, 156.

Chapter 2.

Enhanced electrochemical methanation of carbon dioxide with a dispersible nanoscale copper catalyst

Reproduced in part with permission from: Karthish Manthiram, Brandon J. Beberwyck, and A. Paul Alivisatos, "Enhanced electrochemical methanation of carbon dioxide with a dispersible nanoscale copper catalyst," *Journal of the American Chemical Society* **2014**, *136*, 13319-13325.

Although the vast majority of hydrocarbon fuels and products are presently derived from petroleum, there is much interest in the development of routes for synthesizing these same products by hydrogenating CO_2. The simplest hydrocarbon target is methane, which can utilize existing infrastructure for natural gas storage, distribution, and consumption. Electrochemical methods for methanizing CO_2 currently suffer from a combination of low activities and poor selectivities. We demonstrate that copper nanoparticles supported on glassy carbon (n-Cu/C) achieve up to 4 times greater methanation current densities compared to high-purity copper foil electrodes. The n-Cu/C electrocatalyst also exhibits an average Faradaic efficiency for methanation of 80% during extended electrolysis, the highest Faradaic efficiency for room-temperature methanation reported to date. We find that the level of copper catalyst loading on the glassy carbon support has an enormous impact on the morphology of the copper under catalytic conditions and the resulting Faradaic efficiency for methane. The improved activity and Faradaic efficiency for methanation involves a mechanism that is distinct from what is generally thought to occur on copper foils. Electrochemical data indicate that the early steps of methanation on n-Cu/C involve a pre-equilibrium one-electron transfer to CO_2 to form an adsorbed radical, followed by a rate-limiting non-electrochemical step in which the adsorbed CO_2 radical reacts with a second CO_2 molecule from solution. These nanoscale copper electrocatalysts represent a first step toward the preparation of practical methanation catalysts that can be incorporated into membrane-electrode assemblies in electrolyzers.

2.1. Single-step reduction of carbon dioxide to methane

The conversion of CO_2 into hydrocarbons is an alternative route for synthesizing fuels and feedstocks that are typically derived from oil or natural gas, representing one potential strategy to store electrical energy derived from intermittent sources of clean energy, such as wind and solar.[1,2] Although electrosynthetic pathways for converting CO_2 into hydrocarbon products are not economically feasible at present,[3] expected decreases in the price of electricity derived from clean energy sources[4] and policy changes regarding greenhouse gas emissions[5] may alter the economics of reducing CO_2 dramatically. In fact, growing use of intermittent renewable energy sources in certain regions has accelerated the deployment of small-scale electrical energy storage systems, including pilot plants for methanizing CO_2.[6] These pilot plants utilize a two-step process, in which electrical energy is used to power an electrolyzer that splits water to produce hydrogen and oxygen. The hydrogen is then used in the Sabatier reaction,[7] in which CO_2 and H_2 are reacted over a heterogeneous nickel catalyst at temperatures of 250 - 400 ^oC

and pressures of 1 - 80 bar to produce methane, which can be injected into existing natural gas networks. A single-step electrochemical process that can directly convert CO_2 to methane under conditions of ambient pressure and temperature may represent an attractive alternative.

2.2. Limitations of existing catalysts

Of the metals explored as catalysts for electrochemical CO_2 reduction,[8] the most active and selective identified to date are gold, silver, and bismuth,[9–14] which produce CO as their terminal product. Copper is attractive in comparison, as it produces more reduced hydrocarbon products.[8,15–17] One of the hydrocarbon products formed on copper electrocatalysts is methane, which forms through the following half-reaction:

$$CO_2 + 8H^+ + 8e^- \rightarrow \quad CH_4 + 2H_2O \qquad (2.1)$$

Because the reaction involves eight electron-transfer steps at 0.17 V (all potentials reported versus reversible hydrogen electrode (RHE)) that can easily bifurcate to form a wide range of products, the process exhibits poor selectivity for any single product, forming a mixture of methane, ethylene, hydrogen, carbon monoxide, and formic acid.[18,19] The highest Faradaic efficiencies for methane reported to date are 64% on a (210) copper single crystal[18,20] and 73% on an electrodeposited copper electrode.[21] Although studies conducted on high-purity foils, single crystals, and electrodeposited materials have served as benchmarks and provide fundamental insights into how copper catalyzes the reduction of CO_2, these model materials are impractical for electrolyzers as they have low surface areas, cannot be incorporated into the membrane electrode assemblies[22] that are needed to achieve high current densities with low ionic resistances, or are expensive. From the point of view of cost and ease of manufacturing, highly dispersed nanoparticle catalysts are much better suited for electrolyzers.[23] Here, we demonstrate that well-dispersed copper nanoparticles supported on glassy carbon show high activities and Faradaic efficiencies for methanation, comparable to those of much more expensive single-crystal electrodes. Systematic studies of nanoparticle loading on the glassy carbon support and electrochemical analysis indicate that the altered reactivity of the copper nanoparticles is due to distinct catalytic sites present on isolated nanoparticle catalysts supported on glassy carbon.

2.3. Morphological evolution

We colloidally synthesized copper nanoparticles capped with tetradecylphosphonate of diameter 7.0 ± 0.4 nm (Figure 2.1a,b).[24] These particles were spin-coated onto glassy carbon plates (Figure 2.1c), hereafter referred to as n-Cu/C, which served as the working electrode in a three-electrode setup containing CO_2-saturated 0.1 M sodium bicarbonate electrolyte, pH 6.8. As a control, we also used high-purity copper foils as the working electrode. All current densities for nanoparticle electrodes are surface-area normalized.

During the course of electrochemical CO_2 reduction, the morphology of the copper nanoparticles changes significantly, growing in size to 23 ± 8 nm in diameter (Figure

2.1d). The nanoparticles that form are highly polycrystalline, as revealed using high-resolution transmission electron microscopy (Figure 2.1e,f). We find that irrespective of the initial size of the nanoparticles on glassy carbon, the particles evolve in size to form particles which are ~25 nm in diameter, even if we begin with larger particles. For instance, if we treat the initially cast particles (Figure 2.1c) with trimethylsilyl chloride, the tetradecylphosphonate ligand is stripped off of the surface of the particles, causing the particles to ripen to a diameter of 52 ± 21 nm prior to polarization (Figure 2.1g). These large, irregular particles then evolve in size and shape during the course of electrochemical CO_2 reduction to form smaller, uniform, roughly spherical particles which are 25 ± 8 nm in diameter (Figure 2.1h). Similar changes in size are also observed in the absence of CO_2 (Figure A.1.1). The morphological evolution observed, which may be due to a combination of particle coalescence and dissolution-redeposition, points toward the importance of verifying if size distributions are maintained in studies of size-dependent electrocatalysis.[25]

2.4. Catalytic behavior

Although the n-Cu/C electrodes and copper foil electrodes exhibit comparable current densities at lower overpotentials, the current densities for n-Cu/C electrodes are over twice as high at more reducing potentials (Figure 2.2a). Of this increased current, a much greater fraction from the n-Cu/C electrode goes toward methane compared to the copper foil (Figure 2.2b). The Faradaic efficiency for methane is improved at more reducing potentials for n-Cu/C, reaching 76% at -1.35 V. This is significantly higher than the Faradaic efficiency of 44% achieved on a polycrystalline copper foil at the same potential (Figure 2.2b). The combined enhancement in both the overall current density and Faradaic efficiency for methanation on n-Cu/C leads to partial current densities for methane that are four times higher for n-Cu/C compared to the copper foil at -1.35 V (Figure 2.2c). Hydrogen evolution, which is undesirable since the intended reduction target is CO_2, is also suppressed on n-Cu/C compared to the copper foil. The Faradaic efficiency for hydrogen is 13% at -1.25 V on n-Cu/C, half that of a polycrystalline copper foil at the same potential (Figure 2.2d).

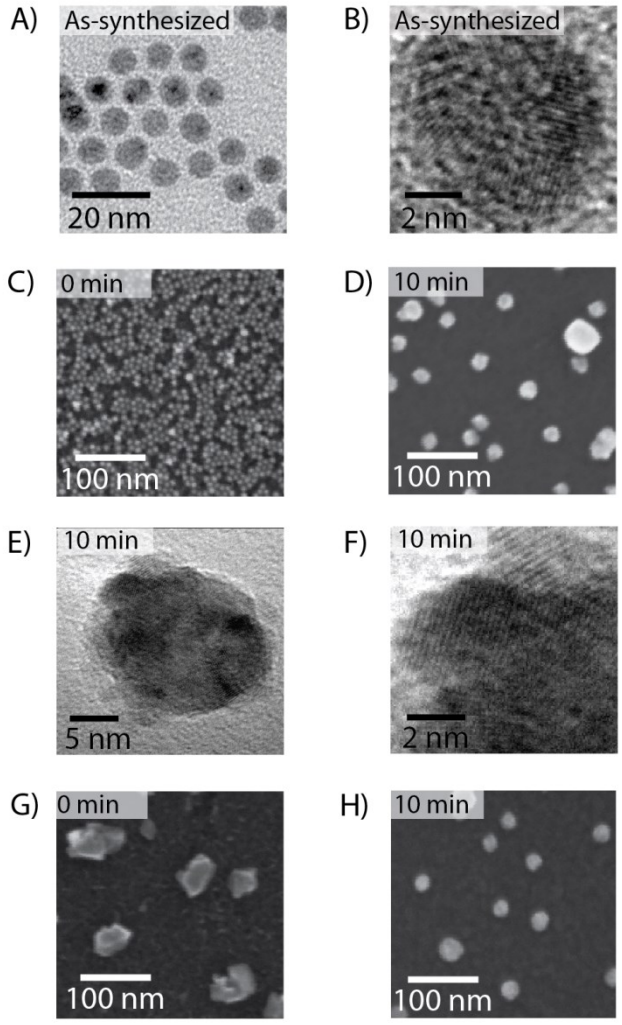

Figure 2.1. Morphological evolution of copper nanoparticles during the course of electrochemical CO_2 reduction. Transmission electron microscopy (TEM) images of as-synthesized copper nanoparticles of diameter 7.0 ± 0.4 nm at (a) low magnification and (b) high magnification, showing that the initial particles are highly polycrystalline. (c) Scanning electron microscopy (SEM) of n-Cu/C electrode, consisting of copper nanoparticles supported on glassy carbon substrate. (d) SEM of n-Cu/C electrode following polarization for 10 min at -1.25 V under CO_2 electroreduction conditions, demonstrating that the average particle diameter grows to 23 ± 8 nm. TEM images of copper nanoparticle transferred from glassy carbon substrate following polarization onto TEM grid at (e) low magnification and (f) high magnification, in which it is evident that the particles that form under polarization are highly polycrystalline. (g) SEM of trimethylsilyl chloride-treated n-Cu/C electrode prior to polarization, in which particles have an average diameter of 52 ± 21 nm. (H) SEM of the same electrode following polarization for 10 min at -1.25 V, in which the particles that form are 25 ± 8 nm in diameter.

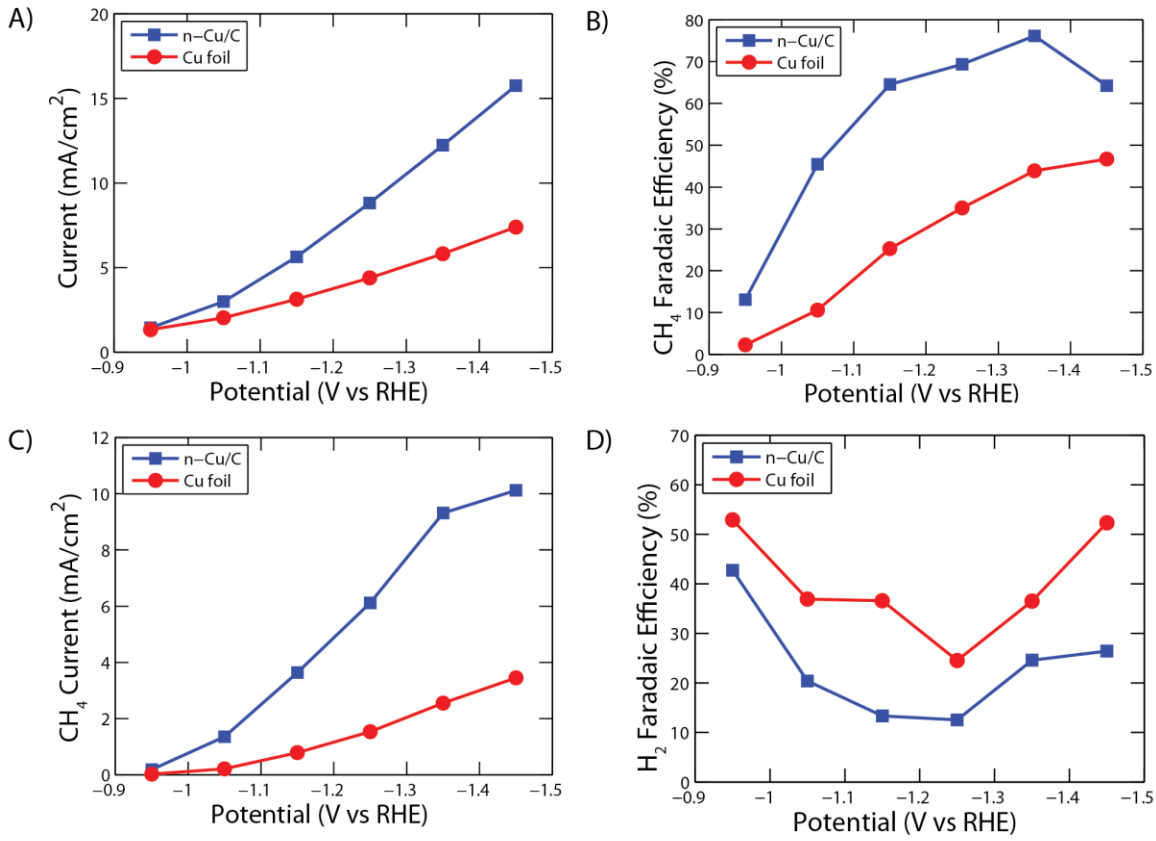

Figure 2.2. Comparison of current densities and Faradaic efficiencies for n-Cu/C and copper foil electrodes. (a) Total current density, demonstrating that n-Cu/C has greater overall reduction activity than the copper foil. (b) Faradaic efficiency for methane, in which it is evident that n-Cu/C is more selective for methane than the copper foil. (c) Methanation current density, in which the combined effect of the improved current density and Faradaic efficiency on n-Cu/C is apparent. (d) Faradaic efficiency for hydrogen as a function of potential, showing suppressed hydrogen evolution on the n-Cu/C catalyst.

The current densities for n-Cu/C are relatively stable at -1.25 V during extended periods of CO_2 reduction (Figure 2.3a), decaying only 3% over the course of 1 h, indicating a stability surpassing copper foil electrodes, for which the current density decays by 11% (Figure A.1.2). The Faradaic efficiency for methane on n-Cu/C does not decay during extended periods of CO_2 reduction (Figure 2.3b), remaining in the range of 71-90%, with an average yield of 80% over 1 h, which is the highest Faradaic efficiency for methanation reported to date.

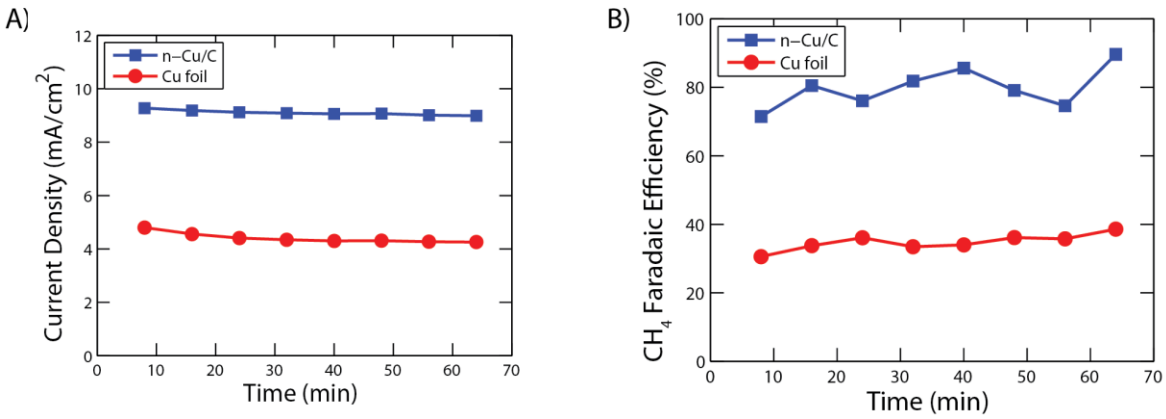

Figure 2.3. Stability of the n-Cu/C and copper foil catalysts. (a) Total current density and (b) Faradaic efficiency for methanation as a function of time for both n-Cu/C and copper foil polarized at -1.25 V, demonstrating that the n-Cu/C catalyst is stable.

2.5. Continuum from nanoparticle-like to foil-like behavior

There are many structural, morphological, and chemical differences between the copper nanoparticles supported on glassy carbon and copper foil electrodes, which could hypothetically be responsible for the increased Faradaic efficiencies for methanation. Some sources of the differences include the presence of tetradecylphosphonate ligand capping the nanoparticles and impurities present in the initial nanoparticles, since they are prepared from a 97% pure copper precursor. In order to determine the effect of these various factors, we utilized a distinctly different method of preparation of the electrocatalyst, by evaporating a thin film of copper onto glassy carbon using a high-purity copper source. For a 3 nm film (Figure 2.4a), we find that a Faradaic efficiency for methanation of 76% can be achieved (Figure 2.4e), allowing us to conclusively exclude the possibility that the presence of ligands and impurities in the starting material influence the observed improvement in Faradaic efficiency for methanation on n-Cu/C.

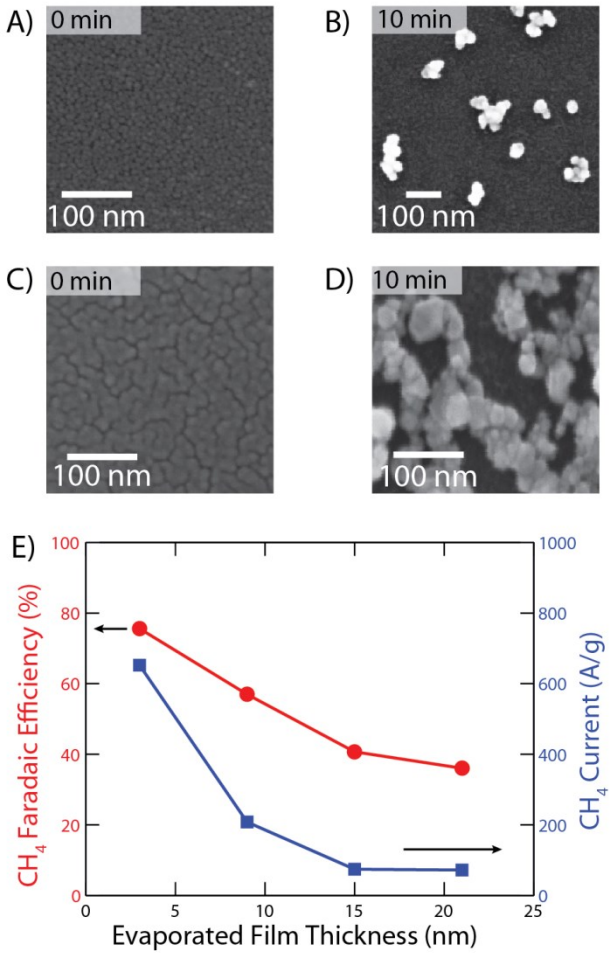

Figure 2.4. Continuum of catalytic behavior between nanoparticle-like and foil-like electrodes. 3 nm evaporated copper film (a) prior to and (b) following polarization at -1.25 V for 10 min, and 15 nm evaporated copper film (c) prior to and (d) following polarization at -1.25 V for 10 min. (e) Methanation Faradaic efficiency and gravimetric methanation current as a function of evaporated copper film thickness, from which it is evident that thin evaporated films behave like the n-Cu/C electrodes while thick evaporated films behave like copper foils.

The thickness of the initially evaporated copper film has a dramatic impact on the Faradaic efficiency for methane. Evaporated films that are relatively thin (Figure 2.4a) produce isolated nanoscale aggregates upon polarization on the electrode (Figure 2.4b) which somewhat resemble the n-Cu/C electrodes (Figure 2.1d); these electrodes have high methanation yields (Figure 2.4e). In contrast, thicker films (Figure 2.4c) produce highly connected networks of fused nanoparticles upon polarization (Figure 2.4d); these electrodes have low Faradaic efficiencies for methanation (Figure 2.4e), as we would expect for an architecture that resembles a polycrystalline foil. This possibly explains why previous studies of dense films of copper nanoparticles have not observed enhanced methanation yields.[26–28] A systematic study of single crystal electrodes for CO_2 reduction has put forth the possibility that the introduction of a particular step-edge present on a (210) single crystal can enhance methanation yields.[20] This suggests that more isolated nanoparticles expose catalytic sites that are more effective for methanation, which are lost as they fuse to form dense aggregates. Structural differences have also been implicated in the enhanced selectivity for CO observed on copper foil catalysts which are oxidized and then reduced.[27,29] Our results demonstrate a continuum of catalytic behavior that exists between electrodes that exhibit nanoparticle-like and foil-like behavior, and that this behavior can be systematically tuned by adjusting the mass loading of copper on glassy carbon (Figure 2.4e).

2.6. Mechanism of CO_2 reduction

In order to glean mechanistic insights regarding the altered catalytic behavior of n-Cu/C compared to copper foils, we measured the Tafel slope of the n-Cu/C catalyst. In the region of Tafel linearity, the Tafel slope for methanation is 60 ± 4.2 mV/decade for n-Cu/C (Figure 2.5a), close to a value of 59 mV/decade, indicative of a one-electron pre-equilibrium step prior to a rate-limiting non-electrochemical step.[11,12,30,31] Tafel slopes for methanation on copper foils vary widely depending on surface preparation, ranging from as low as 86 ± 4.6 mV/decade (Figure 2.5a) to as high as 175 mV/decade.[32] It is generally thought that the rate-limiting step for methanation on copper foils involves a single electron transfer to CO_2 on copper foils,[18] which would correspond to a Tafel slope of 120 mV/decade. The reduced Tafel slope on n-Cu/C is advantageous because smaller excursions in potential are needed to drive logarithmic gains in methanation current.

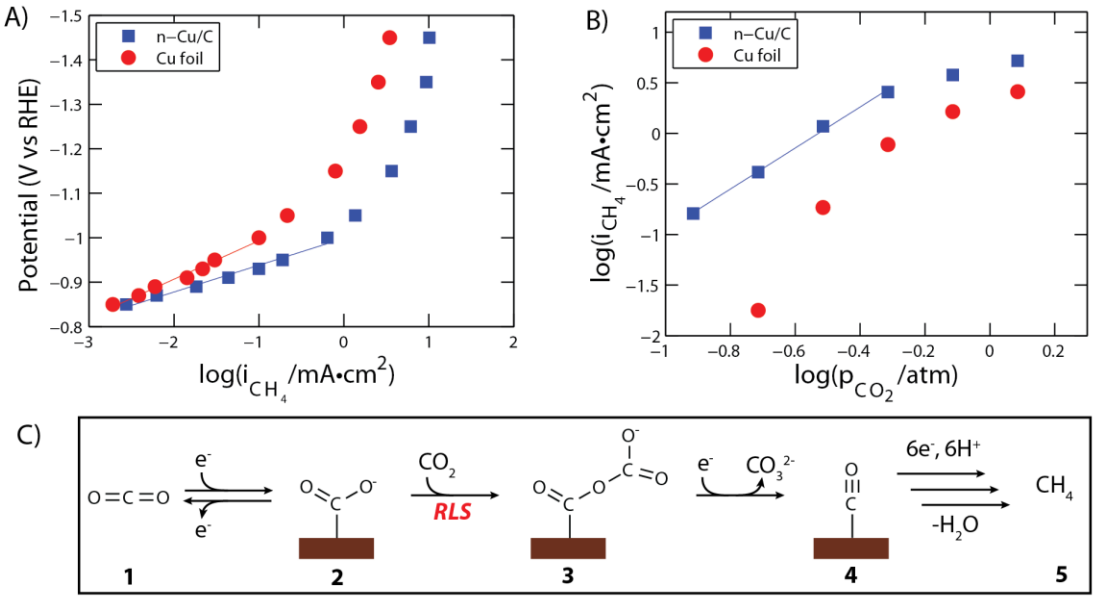

Figure 2.5. **Mechanistic insights from Tafel analysis.** (a) Tafel plot for n-Cu/C and copper foil, with linear fit at low current densities demonstrating that these catalysts have Tafel slopes of 60 ± 4.2 and 86 ± 4.6 mV/decade, respectively. The Tafel slope for n-Cu/C indicates a one electron pre-equilibrium step precedes a non-electrochemical rate limiting step. (b) Methanation current density as a function of partial pressure of CO_2 at -1.25 V, demonstrating that methanation current density has a 2.03 ± 0.08 order dependence on the partial pressure of CO_2 at lower CO_2 partial pressures. (c) Proposed mechanism for the electrochemical reduction of CO_2 to methane, including the rate-limiting step (RLS). This mechanism is consistent with the gathered electrochemical data and known intermediates for CO_2 reduction that have been identified in the literature.

While the Tafel slope provides general insights into the nature of the possible rate-limiting and pre-equilibrium steps, the order dependence of the methanation current on reactants provides a more detailed picture of the rate-limiting step. We find an unusual second-order (2.03 ± 0.08) dependence of methanation current on CO_2 partial pressure for the n-Cu/C catalyst (Figure 2.5b).[33] Based on work on other metals, such as gold[9] and mercury,[34] it is often assumed that CO_2 reduction on copper foils proceeds with a first-order dependence on CO_2 in aqueous electrolytes,[35,36] although we observe an ill-defined order (Figure 2.5b). The methanation current on the n-Cu/C catalyst exhibits no clear order dependence on sodium bicarbonate concentration (Figure A.1.3), although optimization of the buffer concentration can further enhance Faradaic efficiencies for methanation by approximately 10% (Appendix A.1).

Combining the insights provided by the preceding electrochemical analysis, we propose early steps in a possible mechanism that could lead to methane formation (Figure 2.5c). In this proposed mechanism, the CO_2 **1** reacts in a one-electron transfer pre-equilibrium step to form a surface adsorbed CO_2 radical **2**. The CO_2 radical has been experimentally observed on other metals, and it is inferred that it also forms on copper.[18,34,37,38] If we assume that the surface coverage of the CO_2 radical $\theta \ll 1$, consistent with the

observation that copper surfaces are predominantly covered in CO under CO_2 reduction conditions,[39–41] then θ is related to the overpotential η and CO_2 partial pressure p_{CO2} as:

$$\theta = K_1 p_{CO_2} \exp\left(\frac{F\eta}{RT}\right) \tag{2.2}$$

where K_1 is the equilibrium constant for the conversion of **1** to **2**, F is Faraday's constant, R is the gas constant, and T is temperature (Appendix A.1).[30] Following the pre-equilibrium step, the adsorbed CO_2 radical **2** is proposed to undergo rate-limiting carbon-oxygen coupling with a Lewis acid CO_2 molecule from solution to form a CO_2-$CO_2^{-\bullet}$ adduct **3**, which could be either a transition state or a genuine intermediate. Such an adduct has been postulated for electrochemical reduction of CO_2 in non-aqueous solvents on other metals.[38,42–44] The rate of the CO_2-$CO_2^{-\bullet}$ adduct formation step, expressed as a methanation current, is:

$$i_{CH_4} = nFk_2 p_{CO_2}\theta \tag{2.3}$$

where n is the total number of electron transfers needed to convert CO_2 **1** to methane **5** and k_2 is the rate constant for the conversion of **2** to **3**. Combining equations 2.2 and 2.3, we obtain:

$$i_{CH_4} = nFk_2K_1 p_{CO_2}^2 \exp\left(\frac{F\eta}{RT}\right) \tag{2.4}$$

This rate law is consistent with the second-order dependence on CO_2 partial pressure that we experimentally observe. The Tafel slope is given by the partial derivative of the overpotential η with respect to the logarithm of current,[30] which we apply to equation 2.4, yielding:

$$\left(\frac{\partial\eta}{\partial \log i_{CH_4}}\right)_{p_{CO_2}} = \frac{2.3RT}{F} = 59\ mV/decade \tag{2.5}$$

Hence, the theoretical Tafel slope of 59 mV/decade for the proposed mechanism is consistent with our experimental measurement of 60 ± 4.2 mV/decade (Figure 2.5a). The preceding analysis involving the Tafel slope and order-dependence on p_{CO2} has also allowed us to exclude several alternative mechanisms, such as the self-coupling of two $CO_2^{-\bullet}$ and rate-limiting electron transfer to CO_2 (Appendix A.1).

Based on mechanistic understanding of CO_2 reduction on other metals, we may also propose downstream steps for the conversion of CO_2-$CO_2^{-\bullet}$ into methane. In studies done on mercury and lead in dimethylformamide,[38,42–44] the CO_2-$CO_2^{-\bullet}$ adduct **3** is believed to reductively disproportionate to yield both CO_3^{2-} and CO, which is a terminal product on these electrodes. Our experimental observation of CO as a minor product on n-Cu/C electrodes (Figure A.1.4) is consistent with its appearance as an intermediate in our proposed mechanism. Given CO is known to bind to copper with an adsorption enthalpy of ~20 kcal/mol,[45] we may expect it to bind to the copper and further react. The downstream steps in which the adsorbed CO molecule **4** reacts to form methane **5** may be

similar to what has been previously proposed for copper foil electrodes based on detailed studies of their reactivity with CO.[36,46]

2.7. Conclusion

These nanoscale copper electrocatalysts represent a first step toward the development of a dispersed electrochemical methanation catalyst that can be used in practical electrolyzers.[22] Copper nanoparticles are ideal for preparing gas diffusion layers for membrane-electrode assemblies which minimize polarization losses, maximizing the energy efficiency of electrolyzers. In addition, these colloidally-prepared copper nanoparticles have catalytic properties that rival those of much more expensive high-purity foils and single-crystal electrodes. The finding of improved methanation activity and Faradaic efficiency for copper nanoparticle catalysts on glassy carbon through a unique mechanism paves the way for complementary computational and spectroscopic studies to develop a more detailed mechanistic understanding of the origin of the improved catalytic properties.

2.8. References

(1) Nocera, D. G. *ChemSusChem* **2009**, *2*, 387.

(2) Lewis, N.; Nocera, D. *Proc. Natl. Acad. Sci.* **2006**, *104*, 15729.

(3) Banholzer, W.; Jones, M. *AIChE J.* **2013**, *59*, 2708.

(4) Reichelstein, S.; Yorston, M. *Energy Policy* **2013**, *55*, 117.

(5) *Climate Change 2014: Mitigation of Climate Change*; Intergovernmental Panel on Climate Change: Geneva, 2014.

(6) Schiebahn, S.; Grube, T.; Robinus, M.; Zhao, L.; Otto, A.; Kumar, B.; Weber, M.; Stolten, D. In *Transition to Renewable Energy Systems*; Stolten, D.; Scherer, V., Eds.; Wiley: Weinheim, Germany, 2013; pp. 813–847.

(7) Sabatier, P.; Senderens, J. B. *C. R. Acad. Sci.* **1902**, *134*, 689.

(8) Hori, Y.; Kikuchi, K.; Suzuki, S. *Chem. Lett.* **1985**, *11*, 1695.

(9) Hori, Y.; Murata, A.; Kikuchi, K.; Suzuki, S. *J. Chem. Soc. Chem. Commun.* **1987**, 728.

(10) Zhu, W.; Michalsky, R.; Metin, O.; Lv, H.; Guo, S.; Wright, C. J.; Sun, X.; Peterson, A. A.; Sun, S. *J. Am. Chem. Soc.* **2013**, *135*, 16833.

(11) Lu, Q.; Rosen, J.; Zhou, Y.; Hutchings, G. S.; Kimmel, Y. C.; Chen, J. G.; Jiao, F. *Nat. Commun.* **2014**, *5*, 3242.

(12) Chen, Y.; Li, C. W.; Kanan, M. W. *J. Am. Chem. Soc.* **2012**, *134*, 19969.

(13) DiMeglio, J. L.; Rosenthal, J. *J. Am. Chem. Soc.* **2013**, *135*, 8798.

(14) Medina-Ramos, J.; Dimeglio, J. L.; Rosenthal, J. *J. Am. Chem. Soc.* **2014**, *136*, 8361.

(15) Hori, Y.; Murata, A.; Takahashi, R. *J. Chem. Soc. Faraday Trans.* **1989**, *85*, 2309.

(16) Peterson, A. A.; Abild-Pedersen, F.; Studt, F.; Rossmeisl, J.; Nørskov, J. K. *Energy Environ. Sci.* **2010**, *3*, 1311.

(17) Peterson, A.; Nørskov, J. *J. Phys. Chem. Lett.* **2012**, *2*, 251.

(18) Hori, Y. In *Modern Aspects of Electrochemistry*; Vayenas, C. G.; White, R. E.; Gamboa-Aldeco, M. E., Eds.; Springer: New York, 2008; pp. 89–189.

(19) Kuhl, K. P.; Cave, E. R.; Abram, D. N.; Jaramillo, T. F. *Energy Environ. Sci.* **2012**, *5*, 7050.

(20) Hori, Y.; Takahashi, I.; Koga, O.; Hoshi, N. *J. Phys. Chem. B* **2002**, *106*, 15.

(21) Cook, R.; MacDuff, R.; Sammells, A. *J. Electrochem. Soc.* **1988**, *135*, 1320.

(22) Weidner, J. W.; Sethuraman, V. A.; Van Zee, J. W. *Interface* **2003**, *12*, 40.

(23) Rand, D.; Dell, R. *Hydrogen Energy: Challenges and Prospects*; Hunt, J., Ed.; 1st ed.; RSC Publishing: Cambridge, 2007.

(24) Hung, L.-I.; Tsung, C.-K.; Huang, W.; Yang, P. *Adv. Mater.* **2010**, *22*, 1910.

(25) Manthiram, K.; Surendranath, Y.; Alivisatos, A. P. *J. Am. Chem. Soc.* **2014**, *136*, 7237.

(26) Tang, W.; Peterson, A.; Varela, A. *Phys. Chem. Chem. Phys.* **2012**, *4*, 76.

(27) Li, C. W.; Kanan, M. W. *J. Am. Chem. Soc.* **2012**, *134*, 7231.

(28) Reske, R.; Mistry, H.; Behafarid, F.; Roldan Cuenya, B.; Strasser, P. *J. Am. Chem. Soc.* **2014**, *136*, 6978.

(29) Li, C. W.; Ciston, J.; Kanan, M. W. *Nature* **2014**, *508*, 504.

(30) Gileadi, E. *Physical Electrochemistry: Fundamentals, Techniques and Applications*; 1st ed.; Wiley-VCH: Weinheim, Germany, 2011.

(31) Chen, Y.; Kanan, M. W. *J. Am. Chem. Soc.* **2012**, *134*, 1986.

(32) Kim, J. J.; Summers, D. P.; Frese, K. W. *J. Electroanal. Chem.* **1988**, *245*, 223.

(33) Hammouche, M.; Lexa, D.; Momenteau, M.; Saveant, J. M. *J. Am. Chem. Soc.* **1991**, *113*, 8455.

(34) Paik, W.; Andersen, T.; Eyring, H. *Electrochim. Acta* **1969**, *14*, 1217.

(35) Gattrell, M.; Gupta, N.; Co, A. *J. Electroanal. Chem.* **2006**, *594*, 1.

(36) Schouten, K. J. P.; Kwon, Y.; van der Ham, C. J. M.; Qin, Z.; Koper, M. T. M. *Chem. Sci.* **2011**, *2*, 1902.

(37) Jordan, J.; Smith, P. T. *Proc. Chem. Soc.* **1960**, 246.

(38) Aylmer-Kelly, A.; Bewick, A. *Faraday Discuss. Chem. Soc.* **1973**, *56*, 96.

(39) Hori, Y.; Murata, A.; Yoshinami, Y. *J. Chem. Soc., Faraday Trans.* **1991**, *87*, 125.

(40) Hori, Y.; Murata, A.; Tsukamoto, T.; Wakebe, H.; Koga, O.; Yamazaki, H. *Electrochim. Acta* **1994**, *39*, 2495.

(41) Hori, Y.; Koga, O.; Yamazaki, H.; Matsuo, T. *Electrochim. Acta* **1995**, *40*, 2617.

(42) Amatore, C.; Saveant, J. M. *J. Am. Chem. Soc.* **1981**, *103*, 5021.

(43) Amatore, C.; Saveant, J. M. *J. Electroanal. Chem.* **1981**, *126*, 1.

(44) Gennaro, A.; Isse, A. A.; Severin, M.-G.; Vianello, E.; Bhugun, I.; Saveant, J.-M. *J. Chem. Soc. Faraday Trans.* **1996**, *92*, 3963.

(45) Toyoshima, I.; Somorjai, G. A. *Catal. Rev.* **1979**, *19*, 105.

(46) Hori, Y.; Takahashi, R. *J. Phys. Chem. B* **1997**, *5647*, 7075.

Chapter 3.

Dendritic assembly of gold nanoparticles during fuel-forming electrocatalysis

Reproduced in part with permission from: Karthish Manthiram, Yogesh Surendranath, and A. Paul Alivisatos, "Dendritic assembly of gold nanoparticles during fuel-forming electrocatalysis," *Journal of the American Chemical Society* **2014**, *136*, 7237-7240.

We observe the dendritic assembly of alkanethiol-capped gold nanoparticles on a glassy carbon support during electrochemical reduction of protons and CO_2. We find that the primary mechanism by which surfactant-ligated gold nanoparticles lose surface area is by taking a random walk along the support, colliding with their neighbors, and fusing to form dendrites, a type of fractal aggregate. A random walk model reproduces the fractal dimensionality of the dendrites observed experimentally. The rate at which the dendrites form is strongly dependent on the solubility of the surfactant in the electrochemical double layer under the conditions of electrolysis. Since alkanethiolate surfactants reductively desorb at potentials close to the onset of CO_2 reduction, they do not poison the catalytic activity of the gold nanoparticles. Although catalyst mobility is typically thought to be limited for room-temperature electrochemistry, our results demonstrate that nanoparticle mobility is significant under conditions at which they electrochemically catalyze gas evolution, even in the presence of a high surface area carbon and binder. A careful understanding of the electrolyte- and polarization-dependent nanoparticle aggregation kinetics informs strategies for maintaining catalyst dispersion during fuel-forming electrocatalysis.

3.1. Factors contributing to loss of nanoparticle catalyst surface area during electrocatalysis

Critical catalytic transformations, such as the electrochemical reduction of carbon dioxide, require the development of high surface area catalysts that maintain their dispersion over time. Practical electrocatalysts typically consist of nanoscale crystallites, which provide high surface-area-to-volume ratios and can be easily incorporated into membrane electrode assemblies.[1] Nanocrystalline catalysts also exhibit unique electronic and surface structures compared to their bulk counterparts.[2] However, highly dispersed nanocrystals are thermodynamically unstable relative to their corresponding bulk crystalline phase because of the high degree of coordinative unsaturation of their surface atoms. This provides a strong driving force for reducing catalyst dispersion, which occurs via two principal mechanisms: (1) diffusion of atomic species between nanoparticles, commonly referred to as Ostwald ripening,[3] or (2) diffusion, collision, and coalescence of entire nanoparticles.[4] Limiting these two transport processes is critical for maintaining high catalyst dispersion and preserving high activity per unit mass of the material.

Noble metals, such as gold, are attractive for electrocatalysis because they exhibit increased resistance to Ostwald ripening compared to other metals.[5] Gold, in the form of

foils,[6,7] nanoparticles,[8,9] and clusters,[10] is a selective catalyst for reducing CO_2 to CO. For gold under reducing conditions, the primary mechanism available for surface area loss is the diffusion and fusion of entire nanoparticles. At elevated temperature, successive diffusion of individual atoms along the surface of the nanoparticle collectively leads to a random walk of the entire nanoparticle along the support. At room temperature, though, there is insufficient thermal energy to drive such a process for gold.[11,12] Despite this, we find that during the electrochemical reduction of protons and CO_2, a gold nanoparticle electrocatalyst takes a random walk along the support, fuses with its neighbors, and forms dendrites.

As a model catalytic system, we use gold nanoparticles supported on glassy carbon to electrochemically reduce CO_2. Dodecanethiol-capped gold nanoparticles[13] of diameter 4.2 ± 0.5 nm were spin-coated onto a glassy carbon plate (Appendix A.2). This deposition method gives rise to a random array of individual gold nanoparticles at an areal density of $\sim 3 \times 10^{11}$ particles/cm^2 (Figure 3.1a). Gold nanoparticle-coated glassy carbon plates prepared in this fashion served as the working electrode in a three-electrode electrochemical cell containing saturated CO_2/0.1 M $NaHCO_3$ electrolyte (hereafter referred to as 0.1 M $NaHCO_3$ buffer) (Appendix A.2). Experiments were conducted potentiostatically by polarizing to a desired potential and measuring the current versus time (Figures A.2.1). All potentials are reported versus the reversible hydrogen electrode (RHE). Alkanethiols are a convenient ligand for synthesizing gold nanoparticles[14] but are generally thought to poison catalytic sites by blocking access to reactants.[15] The thiol is not a poison for electrochemical CO_2 reduction because it is desorbed from the gold surface at potentials at which we observe appreciable current densities. Indeed, we observe comparable current densities for CO_2 reduction on our gold nanoparticle electrodes and gold foils when we normalize for surface area (Figure A.2.3), although the Faradaic efficiency for CO_2 reduction to CO is lower for our dodecanethiol-capped gold nanoparticle electrodes (Appendix A.2).

3.2. Experimentally-observed dendritic assembly of nanoparticles during electrocatalysis

Upon polarization at −1.2 V, small dendrites with an average diameter of 13 nm formed after 10 min (Figure 3.1b) and even larger dendrites with an average diameter of 140 nm formed after 100 min (Figure 3.1c) of electrolysis, as found using *ex situ* scanning electron microscopy (SEM). Transmission electron microscopy (TEM) analysis reveals that the initially spherical particles (Figure 3.1d) fused into branched dendritic structures (Figure 3.1e).

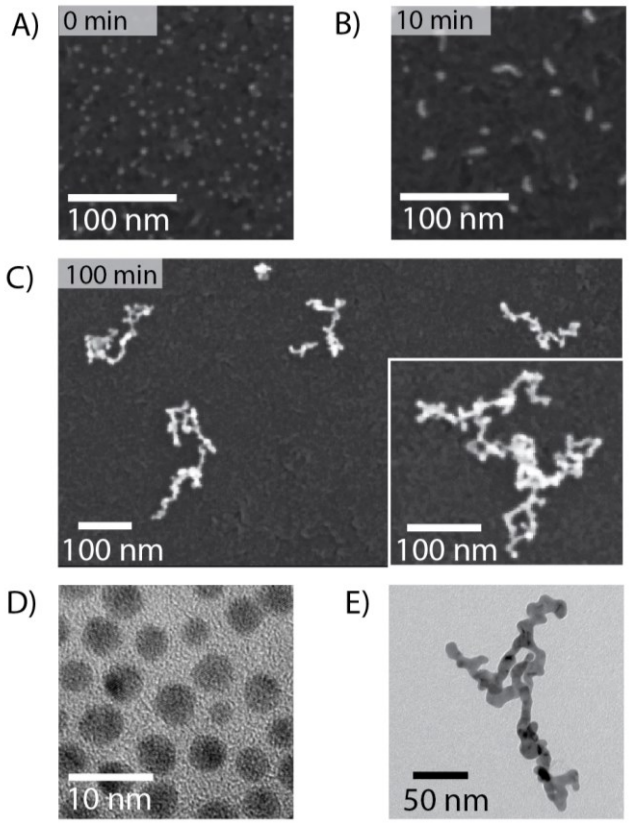

Figure 3.1. SEM and TEM of gold nanoparticles supported on glassy carbon. SEM taken after **(**a) 0, (b) 10, and (c) 100 min of polarization at -1.2 V in 0.1 M $NaHCO_3$ buffer. TEM of (d) as-synthesized gold nanoparticles and e) a dendrite formed after 100 min of polarization.

3.3. Random walk simulations of dendritic assembly of nanoparticles

To further examine the mechanism by which dendrites form, we modeled the diffusion and coalescence of nanoparticles using a random walk algorithm (Appendix A.2). Simulations of this type are well suited to modeling dendrite formation as they have been shown to reproduce the patterns that arise from colloid aggregation.[16,17] For each simulation, the initial state consists of a square lattice with periodic boundary conditions that is randomly populated with particles (Figure 3.2a) at the areal density that we experimentally observe by SEM (Appendix A.2). In each iteration of the simulation, a randomly chosen particle moves randomly by one unit in any direction. When two particles occupy neighboring sites, they fuse irreversibly to form an aggregate with a probability given by the sticking coefficient p_s, which we briefly assume to be unity. If the system is constrained such that fused particles remain immobile on the substrate, small unbranched aggregates result from the simulation when no more individual particles remain (Figure 3.2b). In order to form the larger, highly branched structures observed experimentally (Figure 3.1c), this constraint must be lifted. When the initially formed aggregates are also allowed to move, much larger dendrites are produced (Figure 3.2c) if the simulation is allowed to run until the average diameter of the dendrites is

equal to that observed experimentally after 100 min of electrolysis (Figure 3.1c). While this model suggests that small aggregates remain mobile over the course of electrolysis, the forces that drive this motion remain unclear. In addition to Brownian motion, bubble formation and particle charging may contribute, particularly at very negative applied potentials.

If we impose a kinetic barrier to particle fusion by decreasing the sticking coefficient to p_s=0.1, we observe that dendrites composed of thicker segments of approximately two initial particle diameters form (Figure 3.2d), more closely matching the dendrite filament thickness of two to three initial particle diameters obtained experimentally (Figure 3.1e).

The dendrites formed upon electrolysis can be viewed as fractal structures, which are self-similar on multiple length scales.[21,22] Fractals are characterized by a non-integer dimensionality, which is given by the slope of a linear fit to a plot of the logarithm of the area occupied by a dendrite versus the logarithm of the maximum caliper diameter of the same dendrite (Appendix A.2). We expect fractal dimensionalities between the Euclidean dimensions of 1 and 2, with larger values denoting more space-filling structures.

We first calculate the fractal dimensionality of dendrites produced after 100 min of polarization at -1.2 V. Then, random walk simulations of dendrite formation are allowed to proceed until the average of the maximum caliper diameters of the simulated dendrites is the same as that measured experimentally. Figure 3.2e plots the logarithm of area versus the logarithm of maximum caliper diameter for experimental and simulated dendrites. Both sets of dendrites span a similar range and display a roughly linear trend. The fractal dimensionality of the experimentally produced dendrites is 1.5 ± 0.1, which is comparable to the fractal dimensionalities of 1.4 ± 0.1 and 1.3 ± 0.1 for reaction-limited and diffusion-limited dendrite formation, respectively. This analysis further suggests that a diffusion-collision model is sufficient to describe the pathway for dendrite formation during electrolysis.

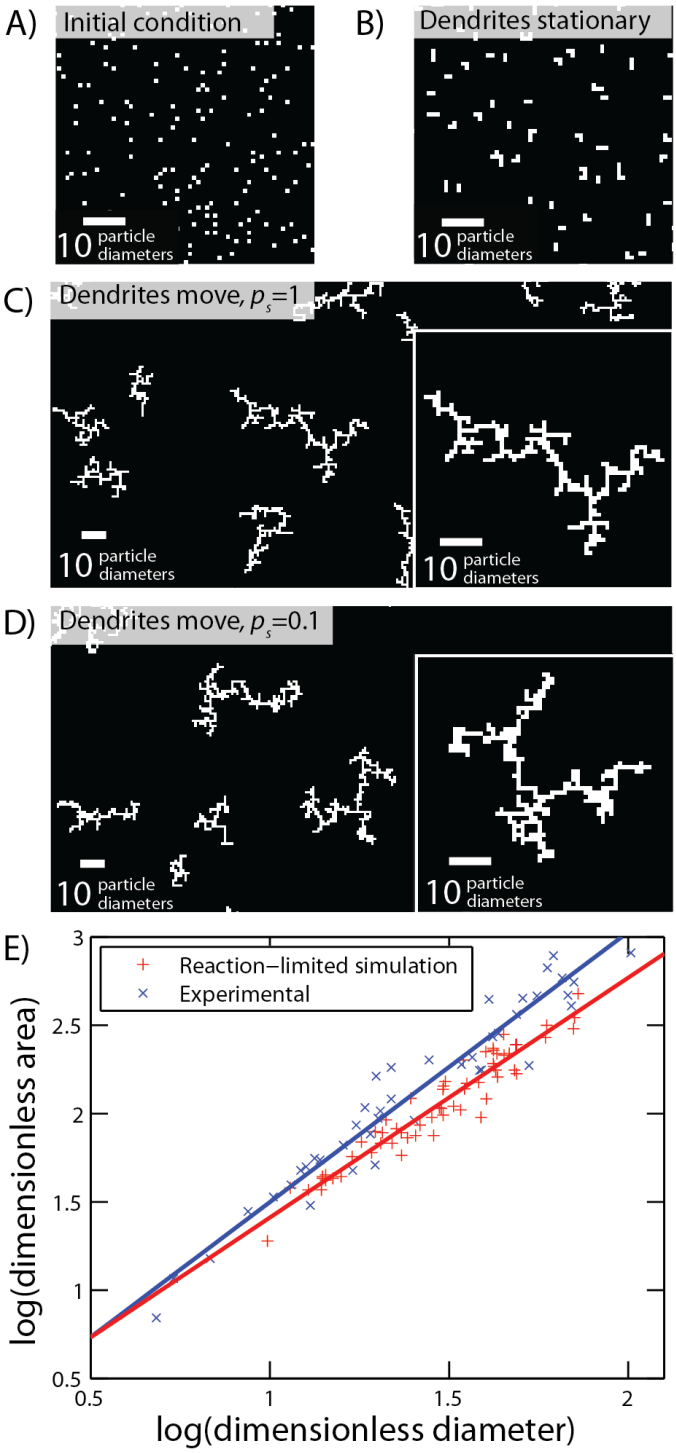

Figure 3.2. Random walk simulations of dendrite formation. (a) Initial condition. (b) Simulated dendrites if only individual particles move with a sticking coefficient of p_s=1. Simulated dendrites if dendrites also move with a sticking coefficient of (c) p_s=1 and (d) p_s=0.1. (e) Dendrite area versus diameter. The solid line indicates a linear fit to the data. The dendrite diameter and area were non-dimensionalized using the particle diameter and square of the particle diameter, respectively.

3.4. Impact of electrode potential and electrolyte on dendritic assembly

The course of dendrite formation is strongly dependent on electrode potential. At -0.2 V, there is no observable dendritic assembly (Figure 3.3a), and the electrode appears identical to the unpolarized electrode (Figure 3.1a). However, dendritic assembly is observed at -0.6 V (Figure 3.3b) and at more negative potentials (Figure 3.1b). Importantly, the potential of this transition coincides with the alkanethiolate reductive desorption potential of -0.6 V,[23,24] suggesting that productive particle fusion occurs more readily when thiols are no longer chemisorbed to the gold nanoparticle surface.

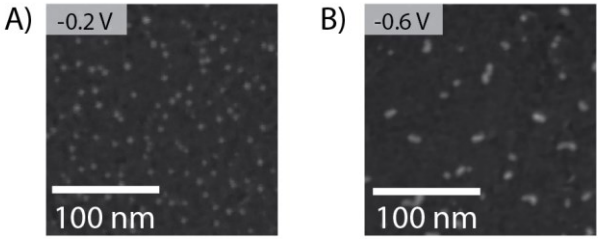

Figure 3.3. Impact of electrode potential on dendritic assembly. SEM of electrodes after polarization for 10 min in 0.1 M $NaHCO_3$ buffer at (a) -0.2 V and (b) -0.6 V.

Surprisingly, dodecanethiol also influences the nanoparticle assembly behavior well beyond its reductive desorption potential. At potentials beyond -0.6 V, the thiolate-gold chemisorption bond is ruptured; however, the dissociated thiolate may remain physisorbed to the gold surface or carbon support. Indeed, X-ray photoelectron spectroscopy of gold nanoparticle decorated electrodes subjected to exhaustive polarization beyond -1.2 V reveals that thiolates remain on the surface (Figures A.2.4 and A.2.5).[25] The degree to which the alkanethiol physisorbs is related to its solubility in the electrolyte, which can be modulated by changing the pH.[23,26] To interrogate the impact of physisorbed ligands, we examined the dendritic assembly in acidic and basic electrolytes under argon gas in the absence of CO_2. Although only H_2 is evolved under these conditions, the pH dependence of dendritic assembly provides insights into the role of the physisorbed thiolates. There is no observable dendritic assembly in 0.1 M H_2SO_4, pH 1, but rapid dendritic assembly is observed during electrolysis in both 0.1 M $NaHCO_3$, pH 6.8, and 0.1 M KOH, pH 12 (Figures 3.4a, 3.4c, and 3.4e). This pH dependence is in line with the significantly higher solubility of dodecanethiolate relative to dodecanethiol in aqueous electrolytes.[27] As dodecanethiol has a pK_a of ~10.5, reductive desorption is accompanied with protonation to form a surface adsorbed thiol in acidic media. These adsorbed thiols sterically impede productive gold nanoparticle fusion events; thus, the sticking coefficient is sufficiently low such that we observe essentially no dendritic assembly (Figure 3.4a). In contrast, in alkaline media, in which the thiolate is not protonated upon reductive desorption, there is rapid dendritic assembly (Figure 3.4e). At a nearly neutral pH of 6.8, the observation of dendritic assembly (Figure 3.4c) appears contrary to what we would expect on the basis of the thiol pK_a of 10.5; however, under reductive polarization, the electrolyte can become significantly more basic in the vicinity of the electrode, especially in electrolytes with low buffer capacity. We believe that the increased local pH under polarization is responsible for increasing the local solubility of

the thiolate and driving dendritic assembly at intermediate pHs. Consistent with this hypothesis, we observe reduced dendritic assembly in 0.5 M $NaHCO_3$ buffer (Figure 3.4d), in which the increased electrolyte strength diminishes local pH gradients at the electrode surface. Additionally, the increased ionic strength may serve to screen charge–charge repulsion between the physisorbed thiolates, inhibiting their dissociation from the surface.[26] We also observe that dendritic assembly is suppressed upon going from 0.1 M KOH to 0.5 M KOH (Figure 3.4f), suggesting that dielectric screening may also play a role in alkaline media; the reduced dendritic assembly also improves activity for hydrogen evolution (Figure A.2.2). Solubility arguments can also be used to rationalize why dodecanethiol is a more effective ligand for retarding dendritic assembly relative to dodecylamine (Figure A.2.6). Together, these results indicate that the electrolyte composition is the primary determinant of the rate of dendritic assembly by modulating the solubility of physisorbed surfactants.

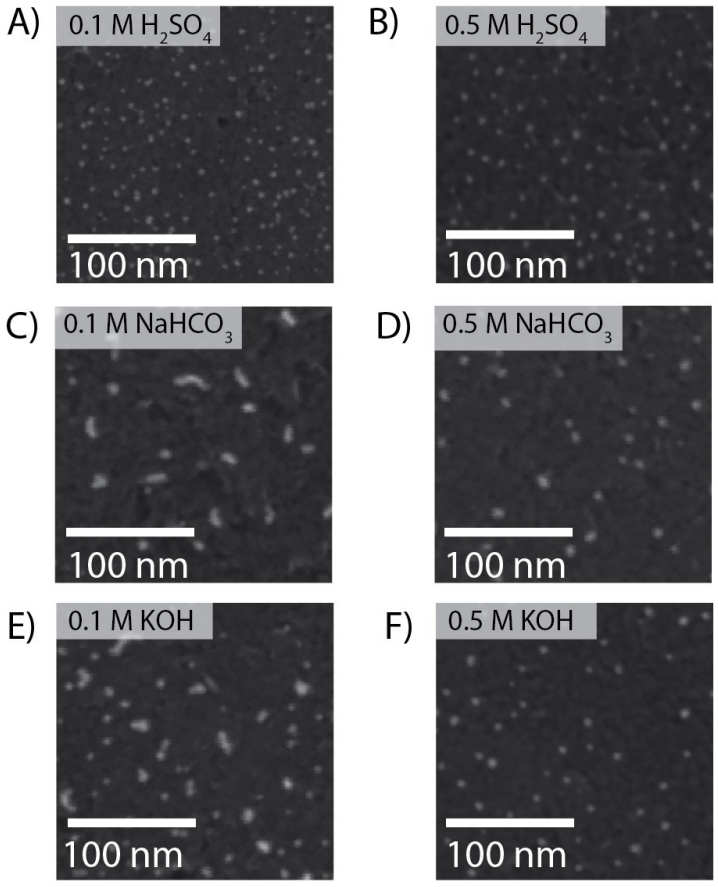

Figure 3.4. Impact of pH and ionic strength on dendritic assembly. SEMs of electrodes after polarization at -1.2 V for 10 min in (a) 0.1 M H_2SO_4, (b) 0.5 M H_2SO_4, (c) 0.1 M $NaHCO_3$, (d) 0.5 M $NaHCO_3$, (e) 0.1 M KOH, and (f) 0.5 M KOH.

3.5. Assembly of nanoparticles embedded in practical catalyst architectures

The mobility of nanoparticles electrochemically catalyzing gas evolution is a fundamental process that occurs even when the nanoparticles are encapsulated in a binder, as is common in practical catalytic systems. To demonstrate this, we have examined the nanoparticle mobility and fusion events in a composite system, comprised of acetylene black and poly(vinyledene fluoride). In this binder, dendritic assembly still occurred (Figure 3.5) but at a slower rate than in the absence of these additives. This suggests that the additives simply act to provide steric hindrance between the diffusing particles, thereby reducing the collision frequency. To block the diffusion-aggregation process completely would require that the nanoparticles be bound to the substrate tightly enough to perturb the nanoparticles themselves. What we have found here is that the diffusion-aggregation process can be controlled by tuning the ligand chemistry in such a way as to allow aggregation to proceed up to a point, while retaining functional catalytic activity.

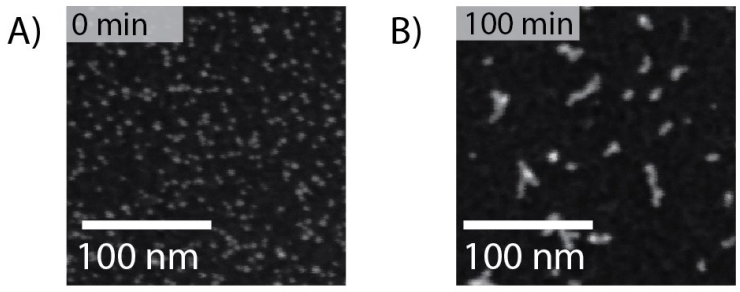

Figure 3.5. Comparison of model system and practical electrode. SEM of electrodes consisting of gold nanoparticles, acetylene black, and poly(vinylidene fluoride) (a) prior to polarization and (b) following 100 min of polarization at -1.2 V in 0.1 M $NaHCO_3$ buffer.

3.6. Conclusion

Our work demonstrates that carbon supported nanoparticles are subject to diffusion, collision, and fusion to form dendritic assemblies under reductive polarization, even at room temperature and in the presence of a high surface area carbon and binder. A simple random walk model is sufficient to describe the formation of dendrites with agreement between the simulated and experimental fractal dimensionalities. Additionally, this study highlights the critical role of electrolyte- and polarization-dependent surface chemistry in mediating nanoparticle aggregation during electrocatalysis. By giving an improved understanding of the mechanism by which gold nanoparticles lose surface area via dendritic assembly, these studies inform strategies for preserving catalyst dispersion in order to maintain activity under harsh electrochemical conditions.

3.7. References

(1) Weidner, J. W.; Sethuraman, V. A.; Van Zee, J. W. *Interface* **2003**, *12*, 40.

(2) *Catalysis and Electrocatalysis at Nanoparticle Surfaces*; Wieckowski, A.; Savinova, E. R.; Vayenas, C. G., Eds.; Marcel Dekker: New York, 2003.

(3) Ostwald, W. *Z. Phys. Chem* **1900**, *34*, 495.

(4) Smoluchowski, M. *Z. Phys. Chem* **1917**, *1210*, 129.

(5) Pourbaix, M. *Atlas of Electrochemical Equilibria in Aqueous Solutions*; 2nd ed.; National Association of Corrosion Engineers: Houston, 1974.

(6) Hori, Y.; Kikuchi, K.; Suzuki, S. *Chem. Lett.* **1985**, *11*, 1695.

(7) Hori, Y. In *Modern Aspects of Electrochemistry*; Vayenas, C. G.; White, R. E.; Gamboa-Aldeco, M. E., Eds.; Springer: New York, 2008; pp. 89–189.

(8) Zhu, W.; Michalsky, R.; Metin, O.; Lv, H.; Guo, S.; Wright, C. J.; Sun, X.; Peterson, A. A.; Sun, S. *J. Am. Chem. Soc.* **2013**, *135*, 16833.

(9) Chen, Y.; Li, C. W.; Kanan, M. W. *J. Am. Chem. Soc.* **2012**, *134*, 19969.

(10) Kauffman, D. R.; Alfonso, D.; Matranga, C.; Qian, H.; Jin, R. *J. Am. Chem. Soc.* **2012**, *134*, 10237.

(11) Wynblatt, P.; Gjostein, N. *Prog. Solid State Chem.* **1975**, *9*, 21.

(12) Baker, R. *J. Catal.* **1982**, *78*, 473.

(13) Hussain, I.; Graham, S.; Wang, Z.; Tan, B.; Sherrington, D. C.; Rannard, S. P.; Cooper, A. I.; Brust, M. *J. Am. Chem. Soc.* **2005**, *127*, 16398.

(14) Love, J. C.; Estroff, L. A.; Kriebel, J. K.; Nuzzo, R. G.; Whitesides, G. M. *Chem. Rev.* **2005**, *105*, 1103.

(15) Kuhl, K. P.; Cave, E. R.; Abram, D. N.; Jaramillo, T. F. *Energy Environ. Sci.* **2012**, *5*, 7050.

(16) Brust, M.; Walker, M.; Bethell, D.; Schiffrin, D. J.; Whyman, R. *J. Chem. Soc., Chem. Commun.* **1994**, *7*, 801.

(17) Oudar, J. *Catal. Rev. Eng.* **1980**, *22*, 37.

(18) Witten, T.; Sander, L. *Phys. Rev. Lett.* **1981**, *47*, 1400.

(19) Meakin, P. *Phys. Rev. Lett.* **1983**, *51*, 1119.

(20) Meakin, P. *Phys. Lett. A* **1985**, *107A*, 269.

(21) Mandelbrot, B. B. *The Fractal Geometry of Nature*; W. H. Freeman and Company: New York, 1982.

(22) Meakin, P. *Annu. Rev. Phys. Chem.* **1988**, *39*, 237.

(23) Yang, D.; Wilde, C.; Morin, M. *Langmuir* **1996**, *12*, 6570.

(24) Widrig, C.; Chung, C.; Porter, M. *J. Electroanal. Chem.* **1991**, *310*, 335.

(25) Byloos, M.; Al-Maznai, H.; Morin, M. *J. Phys. Chem. B* **1999**, 6554.

(26) Yabroff, D. *Ind. Eng. Chem.* **1940**, *32*, 257.

(27) Emmet, E. E. *Organic Chemistry of Bivalent Sulphur*; Chemical Publishing Company: New York, 1958.

Chapter 4.

Tunable localized surface plasmon resonances in tungsten oxide nanocrystals

Reproduced in part with permission from: Karthish Manthiram and A. Paul Alivisatos, "Tunable Localized Surface Plasmon Resonances in Tungsten Oxide Nanocrystals," *Journal of the American Chemical Society* **2012**, *134*, 3995-3998.

Transition-metal oxide nanocrystals are interesting candidates for localized surface plasmon resonance hosts because they exhibit fascinating properties arising from the unique character of their outer-d valence electrons. $WO_{3-\delta}$ nanoparticles are known to have intense visible and near-IR absorption, but the origin of the optical absorption has remained unclear. Here we demonstrate that metallic phases of $WO_{3-\delta}$ nanoparticles exhibit a strong and tunable localized surface plasmon resonance, which opens up the possibility of rationally designing plasmonic tungsten oxide nanoparticles for light harvesting, bioimaging, and sensing.

4.1. Free charge-carriers confined in nanoscale transition metal oxides

Free charge-carriers that are dielectrically confined to a nanoparticle at sufficient density participate in resonant, collective oscillations known as localized surface plasmon resonances (LSPRs). There is a dramatic enhancement in the optical field in the vicinity of a plasmonic nanoparticle, which provides for unprecedented control over light-induced excitations at length scales smaller than the diffraction limit. This control has led to the development of plasmonic nanoparticles tailored for applications as diverse as biosensing,[1] cancer photothermal therapy,[2] and light-harvesting in photovoltaics.[3]

The vast majority of investigations of LSPRs have been conducted on noble metals, as they are stable under a wide range of conditions and have a high charge carrier density. LSPRs have also been reported in heavily doped semiconductor nanocrystals, including tin oxide,[4 - 7] copper chalcogenides,[8 - 11] and zinc oxide.[12] LSPRs in heavily doped semiconductors are unique because the LSPR energy may be tuned by adjusting the doping or stoichiometry, providing an additional means of tuning the optical properties that is not as readily available in metals.[13]

Transition-metal oxides (TMOs) are interesting candidates for LSPR hosts because they exhibit fascinating properties arising from the unique character of the outer-d valence electrons.[14] Some of the hallmarks of TMOs include metal-insulator transitions, high-temperature superconductivity, fast ionic transport, and colossal magnetoresistance, which have led to unique applications in the areas of microelectronics, quantum computing, spintronics, and energy conversion and storage. We expect that the exotic properties of TMOs will lead to distinctive plasmonic effects at the nanoscale. For instance, metal-insulator transitions, which have been well-studied in TMOs, may be leveraged to generate LSPRs that are switchable in response to a variety of stimuli,

including temperature, pressure, and composition. In fact, a temperature-switchable LSPR has been identified in vanadium dioxide.[15] An LSPR has also been identified in rhenium trioxide,[16] but the tunability of its charge carrier density has not been demonstrated; in addition, rhenium is among the most expensive metals, which limits practical applications.

4.2. Polaronic and plasmonic absorption in tungsten oxide

Tungsten oxide nanocrystals are a system of particular interest for the study of tunable plasmon resonances in nanoparticles, as tungsten oxide is stable under a wide range of conditions and has a band gap of 2.6 eV, which is ideal for absorption of visible light. These properties have led to the use of tungsten oxide as an anode in photoelectrochemical cells for water splitting.[17] In the bulk, tungsten oxide exhibits a strong color change upon intercalation of small ions such as Li^+ or H^+ or due to oxygen deficiency.[18] In the case of $WO_{3-\delta}$, which generally has a strong blue color, a variety of oxygen-deficient stoichiometries can be obtained, e.g., $WO_{2.72}$ ($W_{18}O_{49}$), $WO_{2.8}$ (W_5O_{14}), $WO_{2.83}$ ($W_{24}O_{68}$), and $WO_{2.9}$ ($W_{20}O_{58}$). These are ordered phases with precise stoichiometries. For $0 < \delta < 0.1$ in bulk $WO_{3-\delta}$, the electrical and optical properties are dominated by localized electrons involved in polarons, which are quasiparticles consisting of a charge carrier and its polarization field in a lattice. Bulk $WO_{3-\delta}$ undergoes a metal-insulator transition at $\delta = 0.1$, as the localized polaronic wave functions begin to overlap and form delocalized states.[19] As a result, for $\delta > 0.1$ in bulk $WO_{3-\delta}$, the electrical and optical properties are dominated by free electrons. The metal-insulator transition has been firmly established in bulk $WO_{3-\delta}$ by a combination of temperature-dependent conductivity measurements,[20] reflectivity measurements of the bulk plasma frequency,[21] and X-ray photoelectron spectroscopy (XPS).[22] Thus, there is a wide range of known phenomena from the bulk that may exhibit interesting size- and shape-dependent behavior at the nanoscale.

To date, studies of nanoscale $WO_{3-\delta}$ have led to some contradictory results. For instance, $WO_{2.72}$ ($W_{18}O_{49}$) nanowires appear to be semiconducting on the basis of electrical transport[23] and photoluminescence studies;[24] it has been proposed that the blue color of nanoscale $WO_{2.72}$ may arise from polaron hopping. In contrast, $WO_{2.8}$ (W_5O_{14}) nanowires appear to be metallic on the basis of XPS and electrical transport measurements;[25] this material is also blue, but the origin of its optical absorption has not been discussed in the literature. We demonstrate in this communication that nanoscale $WO_{2.83}$ ($W_{24}O_{68}$) can support strong LSPRs and that these LSPRs account for a strong absorption feature ranging from the red edge of the visible to the near-IR (NIR).

4.3. Synthesis of structural characterization of tungsten oxide nanorods

$WO_{2.83}$ nanorods were prepared by hot injection of tungsten(V) ethoxide into a solvent mixture of oleic acid and trioctylamine at 315 ^oC under an inert atmosphere (Appendix A.3).[26] The recovered product exhibited a strong blue color (Figure 4.1a). Transmission electron microscopy (TEM) revealed a rod-like morphology (Figure 4.1b) with an average width of 5.4 nm and an average length of 62 nm (Appendix A.3). X-ray

diffraction (XRD) demonstrated that the particles have the monoclinic structure of $W_{24}O_{68}$ (Figure 4.1c), which corresponds to a stoichiometry of $WO_{2.83}$.[27] Like many nonstoichiometric TMOs, $WO_{3-\delta}$ has rich phase behavior, and the particular phase that is obtained depends significantly on the synthetic conditions used.

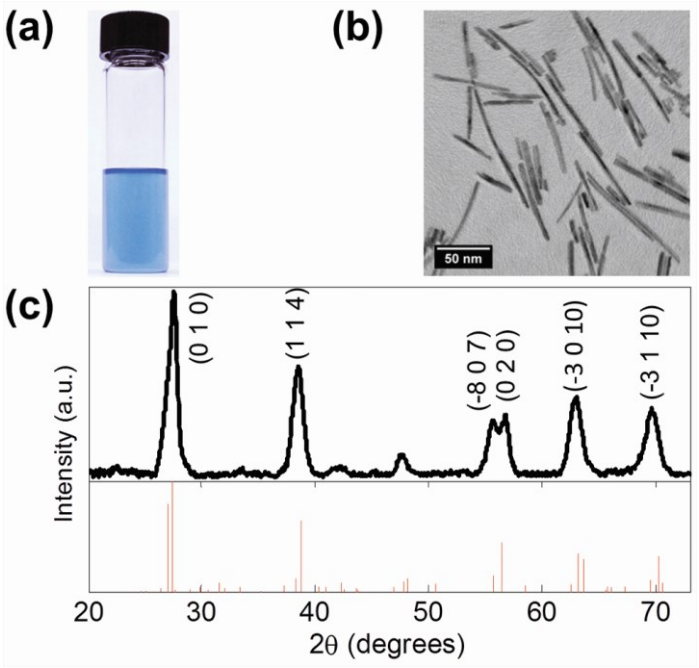

Figure 4.1. Morphology and structure of tungsten oxide nanorods. (a) Photograph of $WO_{2.83}$ nanorods in *N*-methylpyrolidone. (b) TEM micrograph of $WO_{2.83}$ nanorods. (c) XRD pattern of $WO_{2.83}$ nanorods (top) and the reference pattern for $WO_{2.83}$ (bottom).

4.4. Optical characterization of tungsten oxide nanorods

The optical absorption spectrum of our $WO_{2.83}$ nanorods has a peak centered at approximately 900 nm (Figure 4.2a). We used Mie-Gans theory[28] to predict the LSPR spectrum that we would expect for our $WO_{2.83}$ nanorods. The LSPR absorbance A of a solution of nanorods is given by

$$A \propto \omega \varepsilon_m^{\frac{3}{2}} \sum_j \frac{\left(\frac{1}{P_j^2}\right)\varepsilon_2}{\left(\varepsilon_1 + \frac{1-P_j}{P_j}\varepsilon_m\right)^2 + \varepsilon_2^2} \qquad (4.1)$$

where ω is the angular frequency of incident light, ε_m is the dielectric constant of the medium, ε_1 and ε_2 are the real and imaginary parts, respectively, of the dielectric function $\varepsilon(\omega)$ of $WO_{2.83}$, and the P_j are the depolarization factors for axes A, B, and C of the rod (A is the long axis, while B and C are the short axes). We assume that axes B and C have the same width for a rod. The depolarization factors in eq. 4.1 are given by:

$$P_A = \frac{(1-s^2)}{s^2}\left[\frac{1}{2s}\ln\left(\frac{1+s}{1-s}\right) - 1\right] \tag{4.2}$$

$$P_B = P_C = \frac{(1-P_A)}{2} \tag{4.3}$$

The geometric parameter s that appears in eq. 4.2 is

$$s = \sqrt{1-\left(\frac{1}{R}\right)^2} \tag{4.4}$$

where R is the aspect ratio of the rods. We approximate the dielectric function ε(ω) of $WO_{2.83}$ in eq. 4.1 as that of a free-electron gas in the energy range of interest:

$$\varepsilon(\omega) = \varepsilon_1 + i\varepsilon_2 = 1 - \frac{\omega_p^2}{\omega^2 + i\gamma\omega} \tag{4.5}$$

where ω_p is the bulk plasma frequency and γ is the collision frequency. The bulk plasma frequency ω_p in eq. 4.5 is

$$\omega_p = \sqrt{\frac{Ne^2}{\varepsilon_o m_e}} \tag{4.6}$$

where N is the charge carrier density, e is the elementary charge, ε_o is the permittivity of free space, and m_e is the effective mass of an electron. The collision frequency γ in eq. 4.5 is given by

$$\gamma = \frac{1}{\tau} = \frac{e^2 N}{\sigma\, m_e} \tag{4.7}$$

where τ is the scattering time of an electron and σ is the conductivity. We had to estimate several of the parameters in the above equations in order to calculate the LSPR spectrum of our $WO_{2.83}$ nanorods. From the TEM images of our nanorods, we know that the aspect ratio is R = 11 (Appendix A.3). If it is assumed that each oxygen vacancy generates two electrons, the charge carrier density in $WO_{2.83}$ is $N = 6.3*10^{21}$ 1/cm^3. The effective mass of $WO_{3-\delta}$ has been found to be in the range of m_o to $1.4m_o$, where m_o is the rest mass of an electron; hence, we used $m_e = 1.2m_o$.[29] The conductivity of $WO_{2.83}$ has been previously measured to be $\sigma = 2*10^3$ 1/(Ω cm).[19]

Using eq. 4.1, the parameters defined in eqs. 4.2-4.7, and the assumptions defined above, we calculated the absorption spectrum of $WO_{2.83}$ nanorods (Figure 4.2a). We found that Mie-Gans theory predicted the short-axis mode of $WO_{2.83}$ nanorods in *N*-methylpyrrolidone to occur at a wavelength of 860 nm, which is remarkably close to the experimentally observed wavelength of 900 nm. We expect that the experimentally observed short-axis mode is broader than predicted by Mie-Gans theory because of

sample inhomogeneity and damping of the plasmon arising from surface scattering of electrons.[30]

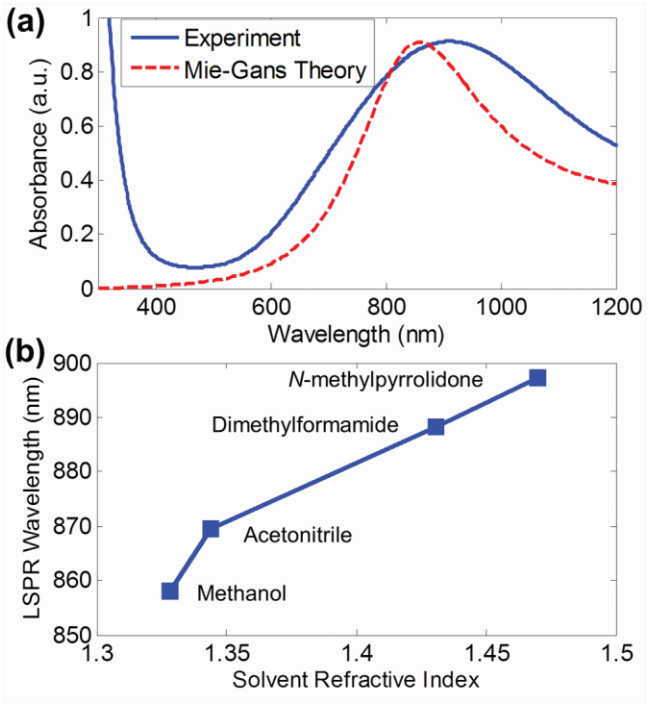

Figure 4.2. Optical absorption of tungsten oxide nanorods. (a) Comparison of experimentally observed and theoretically predicted absorption spectra of the short-axis mode of $WO_{2.83}$ rods in *N*-methylpyrrolidone. (b) Experimentally observed short-axis LSPR wavelength as a function of refractive index of solvent.

In a rod-shaped sample, the long-axis mode is ordinarily the easier mode to observe because of strong coupling to the electromagnetic field. However, in this case, the absorption due to the long-axis mode is expected to occur at very low energy and to be quite broad, rendering it difficult to observe; in fact, our calculations suggested that for a high enough aspect ratio, the long-axis mode does not exhibit a maximum in absorption (Appendix A.3). In contrast, the short-axis mode is quite strong and readily observable in the near-IR to visible regime.

The observed decrease in the LSPR energy with increasing refractive index of the medium is consistent with what we would expect for an LSPR (Figure 4.2b). The magnitude of the experimentally observed shift in the LSPR energy as the solvent was changed from methanol to *N*-methylpyrrolidone was 40 nm, which is smaller than the shift of 60 nm predicted using eq. 4.1. This is reasonable since the solvent may not have complete access to the surface of the particle because of ligand coverage, leading to a weaker dependence of the LSPR energy on the solvent refractive index. Chemical interactions between the solvent and nanoparticle surface can also contribute to differences between the experimental and theoretical LSPR shifts. The complex effect of steric and chemical interactions on the magnitude of the LSPR shift has been well-

established for gold nanoparticles.[31] In addition, if some population of electrons are still involved in a polaronic transition,[19] there may be a polaronic contribution to the optical absorption in $WO_{2.83}$, which would also reduce the magnitude of the observed shift in the LSPR energy.

4.5. Tunability of plasmon mode of tungsten oxide nanorods

The plasmon energy of $WO_{2.83}$ particles could be tuned by heating in an oxidizing environment. When a solution of particles in *N*-methylpyrolidone was heated at 175 °C in air, we observed a red shift and a decrease in the intensity of the plasmon (Figure 4.3a). We expect that the plasmon is red shifted and reduced in intensity due to the incorporation of oxygen into the lattice, leading to a decrease in the carrier concentration. We did not observe the same effect when the solution was heated under an argon atmosphere, suggesting that oxygen plays a key role in this process. The observed blue shift in the band-gap absorption upon heating (Figure 4.3a) is also consistent with oxygen incorporation, as it has been previously observed that the band gap of $WO_{3-\delta}$ is blue-shifted with decreasing δ. XRD of the heated particles suggested that they have a disordered structure (Figure 4.3b), which demonstrates that although oxygen may enter the structure at a low temperature and annihilate the charge carrier, the particles do not fully retain their crystallinity. The disorder may also decrease the effective mass of the electron, further red-shifting the LSPR energy.

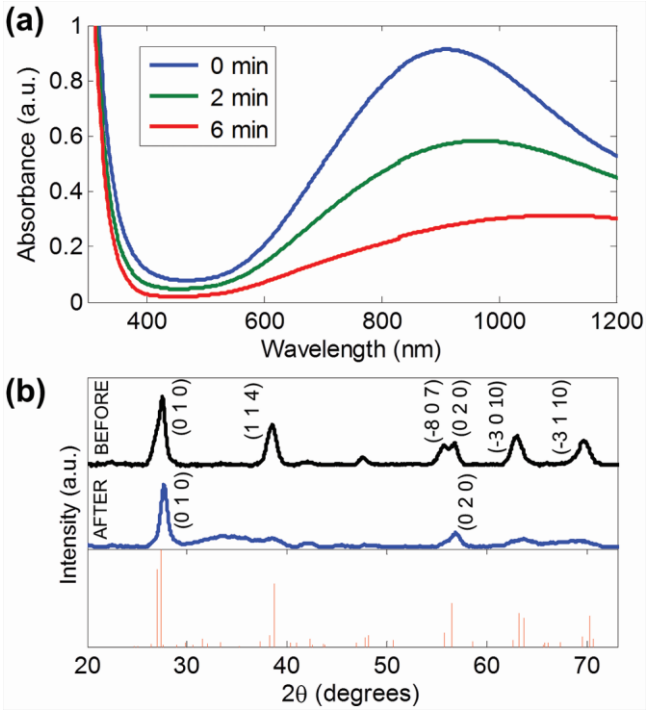

Figure 4.3. Tunability of optical absorption. (a) UV-vis-NIR absorption spectra of $WO_{2.83}$ nanorods in *N*-methylpyrrolidone upon heating at 175 °C in air for 0, 2, and 6 min. (b) XRD pattern of $WO_{2.83}$ nanorods in *N*-methylpyrrolidone (top) before and (middle) after heating at 175 °C for 6 min in air and (bottom) the reference pattern for $WO_{2.83}$ (bottom).

The short-axis mode of the $WO_{2.83}$ nanorods exhibited a high plasmonic sensitivity of 280 nm per refractive index unit (nm/RIU), which is comparable to those of silver nanoprisms (200 nm/RIU for prisms of 50 nm height and 100 nm width),[32] gold nanoshells (130 to 360 nm/RIU for nanoshell thickness to core radius ratios of 3 to 0.1, respectively),[33] and spherical $Cu_{2-x}S$ (350 nm/RIU).[8] Normalizing the plasmonic sensitivity by the LSPR line width gave a sensing figure of merit of 0.5. The quality factor, defined as the ratio of the LSPR energy to the line width was 1.6, which is less than those of gold and silver nanostructures.[34] The quality factor serves as an indicator of the local electric field enhancement. As a result, the electric field in the vicinity of a $WO_{2.83}$ nanoparticle is expected to be weaker than that of gold and silver nanoparticles.

4.6. Conclusion

The high energy of the $WO_{2.83}$ LSPR relative to other identified semiconductor LSPRs, which arises from the high charge carrier density of $N = 6.3*10^{21}$ $1/cm^3$, opens up many practical applications for semiconductor plasmons in the areas of bioimaging, sensing, and light harvesting. The plasmon energy of $WO_{2.83}$ is especially desirable for in vivo bioimaging, as it falls in the "therapeutic window" in which light has a large penetration depth in tissue.[35] In addition, nanostructured $WO_{3-\delta}$ has been investigated for gas sensing applications, as the selectivity for various gases can be tuned by adjusting the stoichiometry of $WO_{3-\delta}$.[36] With increasing interest in the use of nanostructured tungsten oxide as an anode in photoelectrochemical cells, it will be important to pay attention to how oxygen deficiency impacts its photocatalytic properties. Previous studies have used nanostructured $WO_{3-\delta}$ for photocatalysis, as it is stable under photocatalytic conditions and its band gap may be tuned by changing the stoichiometry.[37] The new understanding of the LSPR mode present in $WO_{2.83}$ may provide a better understanding of these previous results and enable the rational design of new plasmonically enhanced tungsten oxide nanostructures for bioimaging, sensing, and light harvesting.

4.7. References

(1) Jain, P. K.; Huang, X.; El-Sayed, I. H.; El-Sayed, M. A. *Plasmonics* **2007**, *2*, 107.

(2) West, J.L; Halas, N. J. *Annu. Rev. Biomed. Eng.* **2003**, *5*, 285.

(3) Atwater, H. A.; Polman, A. *Nature Mater.* **2010**, *9*, 205.

(4) Nutz, T.; Felde, U.; Haase, M. *J. Chem Phys.* **1999**, *110*, 12142.

(5) Kanehara, M.; Koike, H.; Yoshinaga, T.; Teranishi, T. *J. Am. Chem. Soc.* **2009**, *131*, 17736.

(6) Garcia, G.; Buonsanti, R.; Runnerstrom, E. L.; Mendelsberg, R. J.; Llordes, A.; Anders, A.; Richardson, T. J.; Milliron, D. J. *Nano Lett.* **2011**, *11*, 4415.

(7) Li, S. Q.; Guo, P.; Zhang, L.; Zhou, W.; Odom, T. W.; Seideman, T.; Ketterson, J. B.; Chang, R. P. H, *ACS Nano*, **2011**, *11*, 9161.

(8) Zhao, Y.; Pan, H.; Lou, Y.; Qiu, X.; Zhu, J.; Burda, C. *J. Am. Chem. Soc.,* **2009,** *131*, 4253.

(9) Luther, J. M.; Jain, P. J.; Ewers, T.; Alivisatos, A. P. *Nature Mater.* **2011**, *10*, 361.

(10) Dorfs, D.; Hartling, T.; Miszta, K.; Bigall, N. C.; Kim, M. R.; Genovese, A.; Falqui, A.; Povia, M.; Manna, L. *J. Am. Chem. Soc.* **2011**, *133*, 11175.

(11) Kriegel, I.; Jiang, C.; Rodriguez-Fernandez, J.; Schaller, R. D.; Talapin, D. V.; Como, E.; Feldmann, J. *J. Am. Chem. Soc.* **2012**, *134*, 1583.

(12) Buonsanti, R.; Llordes, A.; Aloni, S.; Helms, B.; Milliron, D. J. *Nano Lett.* **2011**, *11*, 4706.

(13) Boltasseva, A.; Atwater, H. A. *Science* **2011**, *331*, 290.

(14) Goodenough, J. B. *Prog. Solid State Chem.* **1971**, *5*, 145.

(15) Rini, M.; Cavalleri, A.; Schoenlein, R. W.; Lopez, R.; Feldman, L. C.; Haglund, R. F.; Boatner, L. A.; Haynes, T. E. *Opt. Lett.* **2005**, *30*, 558.

(16) Biswas, K.; Rao, C. N. R. *J. Phys. Chem. B* **2006**, *110*, 842.

(17) Hodes, G.; Cahen, D.; Manassen, J. *Nature* **1976**, *260*, 312.

(18) Deb, S. K. Sol. Energy Mater. Sol. Cells **1992**, 25, 327.

(19) Salje, E.; Guttler, B. *Phil. Mag. B* **1984**, *50*, 607.

(20) Sahle, W.; Nygren, M. *J. Solid State Chem.* **1983**, *48*, 154.

(21) Viswanathan, K.; Brandt, K.; Salje, E. *J. Solid State Chem.* **1981**, *36*, 45.

(22) Gehlig, R.; Salje, E. *J. Solid State Chem.* **1983**, *49*, 318.

(23) Shi, S.; Xue, X.; Feng, P.; Liu, Y.; Zhao, H.; Wang, T. *J. Cryst. Growth* **2008**, *310*, 462.

(24) Su, C.-Y.; Lin, H.-C. *J. Phys. Chem. C* **2009**, *113*, 4042.

(25) Remskar, M.; Kovac, J.; Virsek, M.; Mrak, M.; Jesih, A.; Seabaugh, A. *Adv. Func. Mater.* **2007**, *17*, 1974.

(26) Yella, A.; Tahir, M. N.; Meuer, S.; Zentel, R.; Berger, R.; Panthöfer, M.; Tremel, W. *J. Am. Chem. Soc.* **2009**, *131*, 17566.

(27) Booth, J.; Ekstrom, T.; Iguchi, E.; and Tilley, R. J. D. *J. Solid State Chem.* **1982**, *41*, 293.

(28) Link, S.; Mohamed, M. B.; El-Sayed, M. A. *J. Phys. Chem. B* **1999**, *103*, 3073.

(29) Molenda, J.; Kubik A. *Phys. Stat. Sol.* **1995**, *191*, 471.

(30) Alvarez, M. M.; Khoury, J. T.; Schaaff, T. G.; Shafigullin, M. N.; Vezmar, I.; Whetten, R. L. *J. Phys. Chem. B* **1997**, *101*, 3706.

(31) Ghosh, S. K.; Nath, S.; Kundu, S.; Esumi, K.; Pal, T. *J Phys. Chem. B.* **2004**, *108*, 13963.

(32) Malinsky, M. D.; Kelly, K. L.; Schatz, G. C.; Van Duyne, R. P. *J. Am. Chem. Soc.* **2001**, *123*, 1471.

(33) Jain, P. K.; Huang, W.; El-Sayed, M. A. *J. Phys. Chem C* **2007**, *111*, 17451.

(34) Sonnichsen, C.; Franzl, T.; Wilk, T.; Plessen, G.; Feldman, J. *Phys. Rev. Lett.* **2002**, *88*, 77402.

(35) Richards-Kortum, R.; Sevick-Muraca, E. *Annu Rev. Phys. Chem.* **1996**, *47*, 555.

(36) Berger, O.; Hoffman, T.; Fischer, W.-J. *J. Mater. Sci.* **2004**, *15,* 483.

(37) Sun, S.; Chang, X.; Dong, L.; Zhang, Y.; Li, Z.; Qiu, Y. *J. Solid State Chem.* **2011**, *184*, 2190.

Chapter 5.

Redox tunability of the plasmonic mode of copper sulfide nanocrystals

Reproduced in part with permission from: Prashant K. Jain, Karthish Manthiram, Jesse Engel, Sarah L. White, Jacob A. Faucheaux, and A. Paul Alivisatos, "Doped semiconductor nanocrystals as plasmonic probes of redox chemistry," *Angewandte Chemie International Edition* **2013**, *52*, 13671-13675. Copyright 2013 by Wiley-VCH.

Copper chalcogenides have been extensively explored as light absorbers for photovoltaics. We demonstrate how local chemical events in the vicinity of copper sulfide nanocrystals can be probed through their perturbation of the carrier density and plasmon mode. Examples demonstrate that redox processes and ligand chemistry can induce changes in the vacancy density within copper (I) sulfide nanorods, allowing such events to be detected by strong shifts in localized surface plasmon resonance.

5.1. Conventional plasmonic sensing through changes in refractive index

The use of nanostructured probes for chemical sensing has opened up the ability to detect ultra-low analyte volumes and achieve nanoscale spatial resolution. Metal nanoparticles exhibiting localized surface plasmon resonances (LSPRs) have been at the forefront of this research[1-5] for two reasons: (1) LSPR scattering can be routinely measured from single nanoparticle probes and (2) the frequency of the LSPR band is highly sensitive to the local refractive index (n_m) around the nanoparticle as per the resonance condition:[6,7]

$$\varepsilon_r(\omega) = -2n_m^2 \qquad (5.1)$$

where ε_r is the real part of the metal dielectric function as a function of optical frequency ω. Analytes, which induce a change in the local refractive index around the nanoparticle, are detected via shifts in the frequency of the LSPR scattering band. The method, while powerful, is limited: chemical events, which do not involve a large enough change in refractive index, go undetected.

5.2. Semiconductor plasmons for sensing local chemical events via changes in carrier concentration

Here, we describe LSPRs of doped semiconductor nanocrystals that are sensitive to redox and ligand binding processes. We take advantage of the fact that the LSPR frequency is proportional to the square root of the carrier concentration within the nanocrystal. We show, using a few different examples, that chemical events occurring locally on the nanocrystal can cause a change in the doping level and carrier concentration within the nanocrystal, resulting in large shifts in the LSPR. The basis of this sensitivity is therefore truly *chemical*, rather than *refractive index*-mediated, unlike conventional metal nanoparticle-based plasmonic probes.

5.3. Copper sulfide nanorods offer improved plasmonic tunability compared to metals

We employ nanorods of the semiconductor copper (I) sulfide, which the Alivisatos and Burda groups have shown to exhibit near-infrared LSPRs due to heavy p-doping resulting from a high level of copper vacancies.[8,9] Others have shown similar LSPRs in nanocrystals of copper (I) selenide and copper (I) telluride.[10-16] LSPR tunability by variation of the copper vacancy concentration has also been demonstrated by the Alivisatos and Manna groups: the greater the vacancy concentration, the higher the LSPR frequency.[9,10] Metal nanoparticles do not possess such tunability since their free carrier concentrations are large and difficult to perturb appreciably.

5.4. Chemistry of copper vacancies in copper sulfide

We exploit the well-known chemical sensitivity of copper (I) sulfide,[17] which can be summarized by the chemical reaction:[18]

$$Cu_{32}S_{16} \rightleftharpoons Cu_{32-n}S_{16} + nCu^0 \qquad (5.2)$$

The creation of one Cu vacancy per unit cell (n = 1) results in copper-deficient sulfide (with a unit cell of $Cu_{31}S_{16}$), which is thermodynamically more stable, by -7.3 eV, than the fully stoichiometric form (with a unit cell of $Cu_{32}S_{16}$). The reaction direction is, however, dictated by the chemical potential of Cu (μ_{Cu}) in the additional copper species formed on the right. In general, conditions which stabilize copper (i.e. lower μ_{Cu}) favor the forward reaction involving the formation of copper vacancies and valence band holes. For instance, copper is much more stable in the form of copper oxide compared to Cu^0; therefore, creation of copper vacancies is strongly favored (Figure 5.1a) in the presence of air or other oxidants:[9]

$$Cu_{32}S_{16} + \tfrac{1}{2}nO_2 \rightarrow Cu_{32-n}S_{16} + nCuO \qquad (5.3)$$

Along with CuO,[12] Cu_2O, known to be stable on the nanoscale[19], may also be formed. Reducing conditions, on the other hand, favor the backward reaction involving the filling of copper vacancies (Figure 5.1b). Due to the high diffusivity of copper atoms in copper (I) sulfide, a well-known solid-state ionic material,[20] reaction kinetics do not appear to be a limiting factor, especially in nanocrystals.

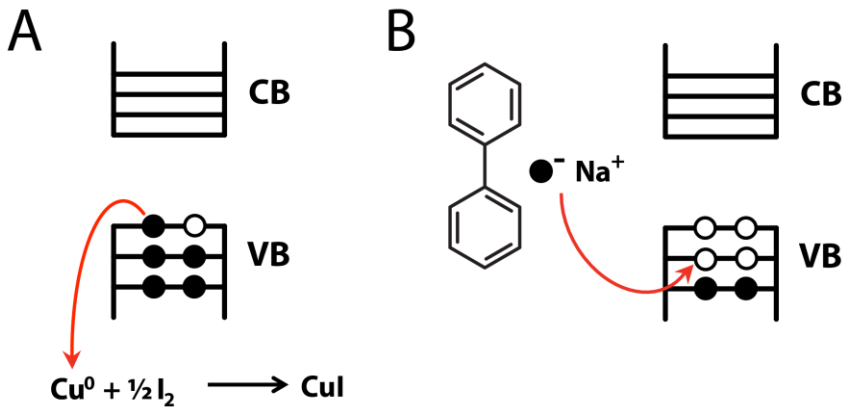

Figure 5.1. Chemical sensitivity of copper (I) sulfide. (a) Conditions such as the presence of oxidants like iodine favor the creation of copper vacancies resulting in holes in the valence band of copper (I) sulfide. (b) Conditions such as presence of electron donors like sodium biphenyl result in filling of the copper vacancies.

5.5. Ligand and redox mediated tuning of copper sulfide plasmons

In particular, we show that ligands such as alkylamines and oxidants such as iodine cause p-doping of the copper sulfide nanorods, manifested by strengthening of the LSPR band and a blue-shift. On the other hand, ligands such as thiols and electron donating reagents such as sodium biphenyl reduce the p-doping level of the nanorods, resulting in a red-shift and suppression of the LSPR. We corroborate by means of electrical measurements that shifts in carrier concentrations are indeed the cause of the observed LSPR changes. The p-type conductivity of copper (I) sulfide nanorod films is enhanced under oxidizing conditions. Application of reducing conditions causes a reversal of the conductivity increase. Our results suggest that doped semiconductor nanocrystals can be used for plasmonic detection of chemical events such as charge transfer, redox chemistry, doping, and ligand binding. In particular, the ability of common ligands such as amines and thiols to electronically dope quantum dots is verified by taking advantage of the optical and electrical sensitivity of the copper (I) sulfide system. We also characterize in detail chemical changes that accompany redox chemistry and doping of nanocrystals.

5.6. Sensing copper extraction via increase in plasmon energy

Copper(I) sulfide nanorods used for the studies here were obtained by the cation exchange of cadmium sulfide nanorods with excess Cu^+ (Appendix A.4), a method known to yield nanorods with negligible number of copper vacancies,[9] evidenced by the low electrical conductivity of the nanorods and lack of plasmonic absorption in the near-infrared region.

The equilibrium copper vacancy density and p-type doping of copper sulfide nanorods can be increased by addition of ligands or oxidants. We hypothesized that the addition of amines, which bind strongly to copper, should assist in extracting copper from the copper sulfide lattice, thus pushing the equilibrium indicated in reaction I to the right. More

copper-deficient stoichiometries ($Cu_{30}S_{16}$, $Cu_{29}S_{16}$, and so on...) are also possible.[21] Upon addition of amine to stoichiometric copper sulfide nanocrystals, we observed that a strong LSPR mode appeared. Copper appears to be removed from the lattice by way of formation of a copper:amine complex, detected by its absorption band at ca. 680 nm (Figure A.4.3b). The LSPR mode blue-shifted and increased in intensity upon each subsequent addition of decylamine (Figure 5.2a), demonstrating the use of the LSPR to monitor progressive changes in the carrier density.

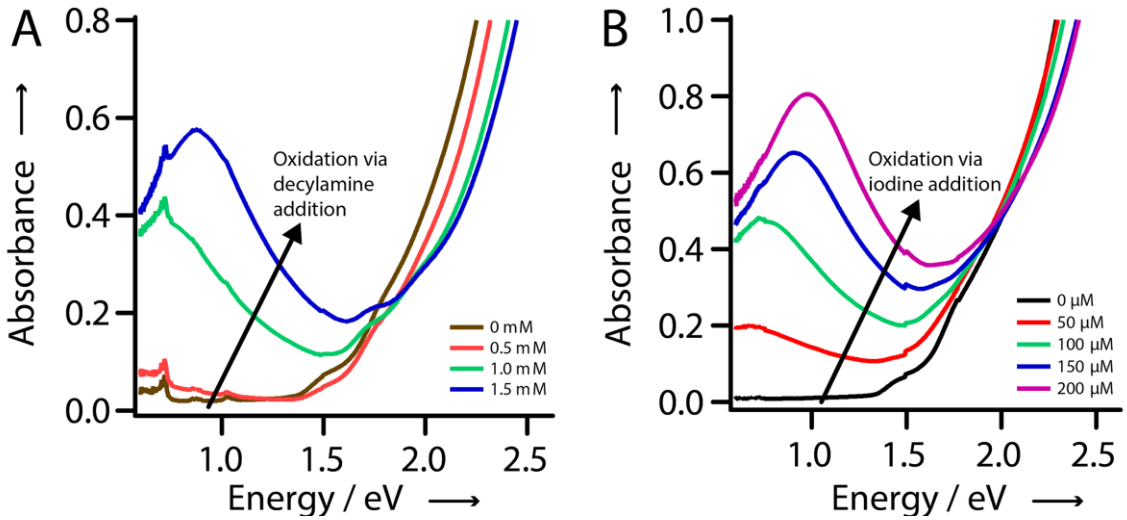

Figure 5.2. LSPR detection of vacancies formed in copper (I) sulfide nanorods by means of ligands or common oxidants. Addition of (a) decylamine or (b) iodine to fully stoichiometric copper sulfide nanorods results in the emergence of an LSPR mode due to the formation of copper vacancies and associated hole carriers. With increasing addition of amine or iodine, the vacancy concentration increases as manifested by a progressive blue-shift and increase in intensity of the LSPR band. The band-gap absorption onset and excitonic peak also blue-shift as expected from an increase in free carrier concentration (Moss-Burstein shift). The starting nanorods were prepared by the cation exchange of CdS with Cu^+ salt under air-free conditions, a method which yields fully stoichiometric or vacancy-free Cu_2S.

Given that copper extraction from copper sulfide is an oxidative process, we also hypothesized that common oxidants, like iodine, should be capable of oxidative extraction of copper ions from copper sulfide via formation of copper iodide as:

$$Cu_{32}S_{16} + \tfrac{1}{2}nI_2 \rightarrow Cu_{32-n}S_{16} + nCuI \qquad (5.4)$$

The addition of iodine to copper sulfide nanorods led to the emergence of an LSPR mode, which gradually blue-shifted and increased in intensity upon incremental iodine additions (Figure 5.2b). The ca. 1 eV peak position of the LSPR mode achieved by the addition of 200 µM iodine corresponds to a stoichiometry of $Cu_{29}S_{16}$ or $Cu_{1.8}S$ (Appendix A.4), known to be the digenite phase. Concomitant to copper extraction, copper iodide was

formed as verified by the appearance of its characteristic absorption band at 410 nm (Appendix A.4).

Thus, both oxidative and non-oxidative copper extraction can be detected via blue-shifts in the LSPR band. Upon copper extraction, the band-edge absorption also blue-shifts, known as a Moss-Burstein shift, as expected from an increase in the free carrier concentration within the nanocrystals. [9]

5.7. Sensing copper insertion via decrease in plasmon energy

Just as the equilibrium of reaction 5.2 can be driven to the right by addition of ligands or oxidants, we expected that the equilibrium could also be shifted to the left by addition of reducing agents. Thiols are known to be mild reducing agents; incremental addition of undecanethiol to air-oxidized copper(I) sulfide nanorods drove the filling of copper vacancies, as evidenced by a gradual shift in the LSPR to lower energies and a reduction in the intensity of the mode. A possible mechanism can involve either disulfide formation or co-ordination of the thiol to metal atoms on the nanocrystal surface as:

$$Cu_{32-n}S_{16} + nCuO + 2nRSH \rightarrow Cu_{32}S_{16} + nRS\text{-}SR + nH_2O \quad (5.5)$$

$$Cu_{32-n}S_{16} + nCuO + 2nRSH \rightarrow Cu_{32}S_{16} + 2nRS\text{-surface bound} + nH_2O \quad (5.6)$$

Similarly, addition of strong reducing agents such as sodium biphenyl (Figure 5.3b) also resulted in a red-shift and suppression of the LSPR band. Sodium biphenyl has been shown to inject electrons into nanocrystals[22] which serves to reverse the hole vacancies in the lattice (Figure 5.1b), although it is unclear as to whether the vacancy is filled by a sodium ion or a copper ion: [23]

$$Cu_{32-n}S_{16} + nNa(C_6H_5\text{-}C_6H_5) \rightarrow Cu_{32-n}Na_nS + n(C_6H_5\text{-}C_6H_5) \quad (5.7)$$

$$Cu_{32n}S_{16} + nCuO + 2nNa(C_6H_5\text{-}C_6H_5) \rightarrow 2nNa_2O + Cu_{32}S_{16} + 2n(C_6H_5\text{-}C_6H_5) \quad (5.8)$$

The absorption band-edge also shifted to lower energies upon addition of either reducing agent, as expected from a decrease in the carrier concentration within the nanocrystals. Complete reversal to Cu_2S did not appear possible (Figure 5.3a), at least with the mildly reducing thiol. Near-complete suppression of the LSPR was, however, observed (Figure A.4.4) with the stronger reducing ability of sodium biphenyl and another reagent cobaltocene, probably when employed in excess. [24] Copper oxide or copper iodide could present a physical barrier, in the form of a thick shell over the nanorod, or a chemical barrier against complete vacancy filling. Also, copper oxide and iodide are p-type semiconductors, whose electronic properties can complicate plasmonic spectra of the nanorods. But, the influence of a copper oxide or iodide shell on the NIR LSPR of the nanorods is estimated to be a small non-resonant dielectric effect, since both these semiconductors have band-to-band transitions in the visible region (Figure A.4.5). Also,

the hole-density of either p-type semiconductor is not adequate to support a NIR intraband absorption or LSPR of its own.

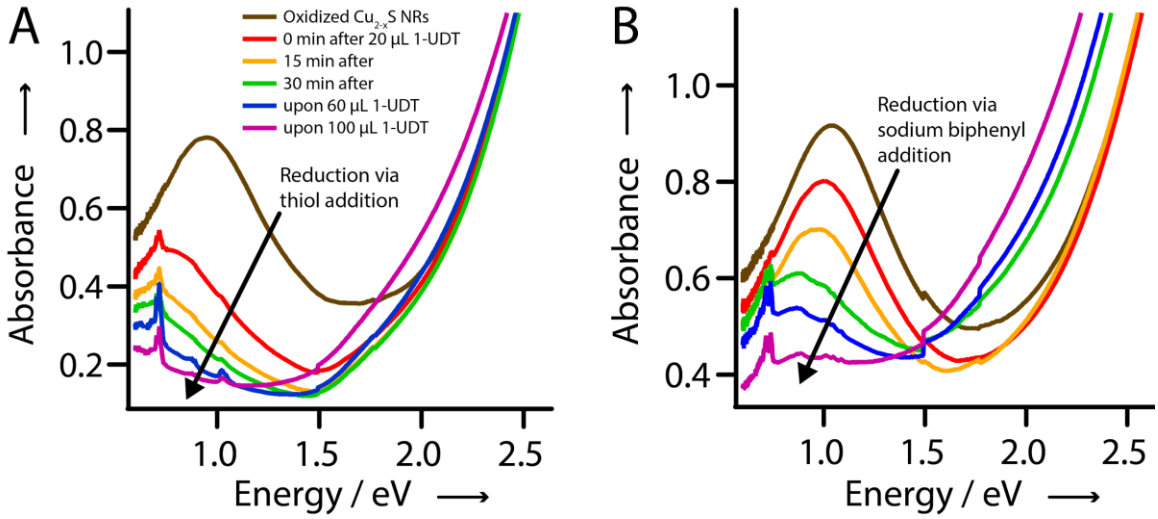

Figure 5.3. LSPR detection of vacancy filling in copper (I) sulfide nanorods by (a) reduction with thiol or (b) electron injection with sodium biphenyl. The addition of undecanethiol or sodium biphenyl to a solution of copper (I) sulfide nanorods results in a progressive red-shift of the LSPR mode and a reduction in its intensity. A concomitant red-shift of the band-edge absorption onset is also seen, i.e., a reverse Moss-Burstein shift. These effects are a manifestation of the progressive filling of vacancies in the nanorod lattice, due to the reducing ability of the thiol or the electron injecting ability of the sodium biphenyl. Note, features around 0.72 eV, 0.87 eV, and 1.0 eV are due to ligand/thiol vibrational absorption. The sharp step at 1.5 eV is an instrumental artifact due to a spectrophotometer grating change. Copper-deficient copper (I) sulfide nanorods were prepared by oxidation of fully stoichiometric Cu_2S nanorods in air. Reduction experiments were carried out in air-free environment in tetrachloroethylene or carbon tetrachloride, solvents with low near-infrared absorbance. The concentration of undecanethiol or sodium biphenyl added to achieve complete reversal was ca. 100 mM.

Electrical measurements serve to directly confirm that the chemical events responsible for LSPR changes indeed modulate the doping level and carrier concentration within the nanocrystal.[25] The conductivity of a nanocrystal film scales monotonically with the free carrier concentration of the effective media:

$$\sigma = N e \mu \qquad (5.9)$$

where N is the majority free carrier density, e is the elemental charge, and μ is the free carrier mobility. Equation 5.9 assumes ohmic conduction and carrier concentration-independent mobility, which are reasonable approximations for a heavily doped transistor device.[26] Moreover, regardless of the assumptions, conductivity still varies monotonically with the free carrier concentration.

5.8. Electrical measurements confirm carrier behavior

We investigated the effects of redox doping on the electrical properties of nanorod films through field-effect transistor (FET) measurements. Films of freshly exchanged copper (I) sulfide nanorods were drop-cast from solution onto highly doped silicon substrates with 300 nm of thermally grown gate oxide and patterned gold contacts. Film thicknesses were estimated at ~150 ± 50 nm from profilometry. After drop-casting, films were initially soaked in a solution of 1 mM ethanethiol (EtSH) in ethanol to permit exchange with the native long-chain oleic acid or phosphonic acid ligands, decrease interparticle spacing, and increase conductivity.[27] Typical for heavy doping, films exhibited large linear conductivity and no transconductance modulation with applied gate voltage, prohibiting the extraction of field-effect mobilities (Appendix A.4).

As shown in Fig. 3a, the small-field (10 mV source-drain) conductivity of the initial film increases dramatically upon exposure to air, rising over two orders of magnitude over 40 hours as oxygen creates copper vacancies within the nanocrystals (reaction 5.3). Fig. 3b demonstrates a complete reversal of this trend upon soaking of the film in 1 mM ethanolic solution of EtSH, a reducing agent. These oxidation and reduction steps are shown to be reversible and repeatable (Figure 5.4c), exhibiting near identical response upon consecutive treatments. In nanoparticle films treated with thiols, oxidation can often lead to a lowering of effective mobility as surface oxides can increase quantum confinement and edge-edge hopping distances. [26] While it is infeasible to deconvolute changes in mobility and carrier concentration for these heavily doped films, the changes in conductivity likely represent a lower bound for the relative changes in doping level. If the redox processes do introduce changes in effective mobility, they also must be reversible, as Figure 5.4c shows the conductivity to be sequentially reversible on the same device. Irreversible chemical changes likely do not play a large role in these treatments, demonstrating the thermodynamic nature of copper vacancy formation and reversal.

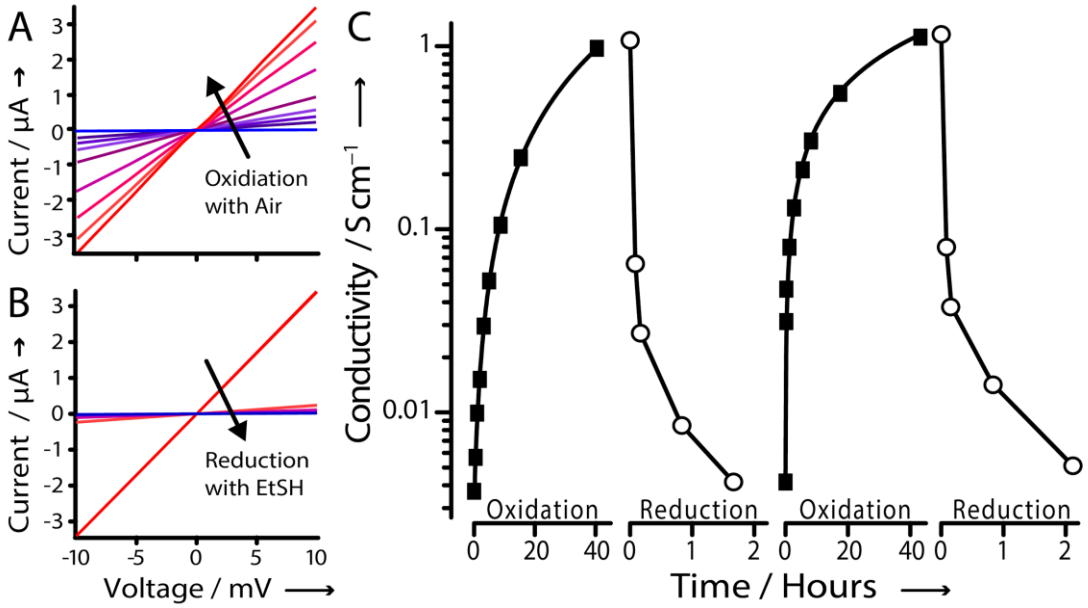

Figure 5.4. Reversible formation and filling of vacancies in copper (I) sulfide nanorod films probed electrically. The small-field conductivity of copper (I) sulfide nanorod thin-film FETs (a) increases over two orders of magnitude upon exposure to air and (b) completely reverses upon soaking in a solution of 1 mM ethanethiol (EtSH) in ethanol. (c) Conductivity measurements on a single device demonstrate reversible vacancy-formation and filling via sequential oxidation and reduction steps. For the measurements, films were initially soaked in EtSH solution to displace long-chain ligands and boost interparticle conductivity. The oxidation steps were performed in air with continuous measurement on an open-air probe station. The reduction steps were performed in an argon glovebox. Conductance was measured between patterned gold contacts with channel lengths of 10 μm and widths of 250 μm.

5.9. Sensing of single chemical events using semiconductor plasmons

A doped semiconductor nanocrystal may potentially be used to achieve plasmonic detection of a single molecule or a single chemical event. This is possible by using a nanocrystal of small-enough size. For instance, in a 4-nm nanocrystal, which has a volume of 34 nm^3, creation of a single copper vacancy is equivalent to an increase dN in the carrier concentration by 3 x 10^{19} cm^3. For a nominally copper-deficient nanocrystal, with a carrier concentration N of 1.5 x 10^{21} cm^3, this is equivalent to a 2% increase in carrier concentration. Since the LSPR wavelength is related to carrier concentration as:[7]

$$\lambda_{sp} \propto \frac{1}{\sqrt{N}} \qquad (5.10)$$

we have:

$$\frac{d\lambda_{sp}}{\lambda_{sp}} \propto -\frac{dN}{2N} \tag{5.11}$$

Thus, the formation of a single copper vacancy would result in a blue-shift in the LSPR wavelength by 1%, which is about 15-20 nm in the 2- μm spectral region. Such shifts can be measured without difficulty, allowing quantized events to be detected on a nanocrystal. While the acquisition of single-particle LSPR scattering spectra in the near-infrared remains a challenge, the approach is feasible, in principle.

5.10. Conclusion

In summary, our work demonstrates qualitatively the ability to use semiconductor nanocrystals for plasmonic probing of processes such as redox reactions, electrochemical charging or discharging, ligand binding, and impurity doping occurring in nanoscale volumes. In the past, such probing has been carried out by means of electrical detection on nanostructures, [28] to which optical detection serves as a complimentary method. Detection of single-molecule events also seems feasible by use of small nanocrystals. Given the promise, there is a need to explore a wider range of chemical and redox processes beyond the limited examples we have provided in the current work.

5.11. References

(1) Sun, Y.; Xia, Y. *Anal. Chem*. **2002**, *74*, 5297–5305.

(2) McFarland, A. D.; Van Duyne, R. P. *Nano Lett.* **2003,** *3*, 1057-1062.

(3) Tam, F.; Moran, C.; Halas, N. J. *J. Phys. Chem. B* **2004**, *108*, 17290–17294.

(4) Willets, K. A.; Van Duyne, R. P. *Annu. Rev. Phys. Chem*. **2007**, *58*, 267-97.

(5) Yan, B.; Boriskina, S. V.; Reinhard, B. M. *J. Phys. Chem. C*, **2011**, *115*, 24437-24453.

(6) Underwood, S.; Mulvaney, P. *Langmuir* **1994**, *10*, 3427–3430.

(7) Jain, P. K.; El-Sayed, M. A. *J. Phys. Chem. C* **2007**, *111*, 17451–17454

(8) Zhao, Y.; Pan, H.; Lou, Y.; Qiu, X.; Zhu, J.; Burda, C. *J. Am. Chem. Soc*. **2009**, *131*, 4253–4261.

(9) Luther, J. M.; Jain, P. K.; Ewers, T. E.; Alivisatos, A. P. *Nature Mater.* **2011**, 10, 361-366.

(10) Choi, J.; Kang, N.; Yang, H. Y.; Kim, H. J.; Son, S. U. *Chem. Mater.* **2010**, *22*, 3586–3588.

(11) Hessel, C. M.; Pattani, V. P.; Rasch, M.; Panthani, M. G.; Koo, B.; Tunnell, J. W.; Korgel, B. A. *Nano Lett*. **2011**, *11*, 2560–2566.

(12) Dorfs, D.; Härtling, T.; Miszta, K.; Bigall, N. C.; Kim, M. R.; Genovese, A.; Falqui, A.; Povia, M.; Manna, L. *J. Am. Chem. Soc.* **2011**, 133, 11175–11180

(13) Scotognella, F.; Valle, G. D.; Kandada, A. R. S.; Dorfs, D.; Zavelani-Rossi, M.; Conforti, M.; Miszta, K.; Comin, A.; Korobchevskaya, K.; Lanzani, G.; Manna, L.; Tassone, F. *Nano Lett*., **2011**, *11*, 4711–4717.

(14) Routzahn, A. L.; White, S. L.; Fong, L.-K.; Jain, P. K. *Israel J. Chem*. **2012**, *52*, 983-991.

(15) Kriegel, I.; Jiang, C.; Rodríguez-Fernández, J.; Schaller, R. D.; Talapin, D. V.; da Como, E.; Feldmann, J. *J. Am. Chem. Soc*. **2012**, *134*, 1583–1590.

(16) Kriegel, I.; Rodríguez-Fernández, J.; Wisnet, A.; Zhang, H.; Waurisch, C.; Eychmüller, A.; Dubavik, A.; Govorov, A. O.; Feldmann, J. *ACS Nano*, **2013**, *7*, 4367-4377.

(17) Lotfipour, M.; Machani, T.; Rossi, D. P.; Plass, K. E., *Chem. Mater*. **2011**, *23*, 3032-3038.

(18) Lukashev, P.; Lambrecht, W. R. L.; Kotani, T.; van Schilfgaarde, M. *Phys. Rev. B* **2007**, *76*, 195202.

(19) Yin, M.; Wu, C.-K.; Lou, Y.; Burda, C.; Koberstein, J. T.; Zhu, Y.; O'Brien, S. *J. Am. Chem. Soc*. **2005**, 127, 9506-9511.

(20) Knauth, P.; Tuller, H. L. *J. Am. Ceram. Soc.* **2002**, *85*, 1654-1680.

(21) Putnis, A. *Am. Mineralogist* **1977**, *62*, 107-l 14.

(22) Shim, M.; Guyot-Sionnest, P. *Nature* **2000**, *407,* 981-983.

(23) Kim, J. S.; Kim, D.-Y.; Cho, G.-B.; Nam, T.-H.; Kim, K.-W.; Ryu, H.-S.; Ahn, J.-H.; Ahn, H. J. *J. Power Sources* **2008**, *189*, 864-868.

(24) Koh, W.-K.; Koposov, A. Y.; Stewart, J. T.; Pal, B. N; Robel, I.; Pietryga, J. M.; Klimov, V. I. *Sci. Rep.* **2013**, *3*, 2004.

(25) Klem, E. J. D.; Shukla, H.; Hinds, S.; MacNeil, D. D.; Levina, L.; Sargent, E. H. *Appl. Phys. Lett*. **2008**, *92*, 212105.

(26) Zarghami, M. H.; Liu, Y.; Gibbs, M.; Gebremichael, E.; Webster, C.; Law, M. *ACS Nano* **2010**, *4*, 2475–85.

(27) Luther, J. M.; M. Law, M.; Song, Q.; Perkins, C. L.; Beard, M. C.; Nozik, A. J. *ACS Nano* **2008**, *2*, 271–80.

(28) Cui, Y.; Wei, Q.; Park, H.; Lieber, C. M. *Science* **2001**, *293*, 1289-1292.

Appendix.

A.1. Supporting information for enhanced electrochemical methanation of carbon dioxide with a dispersible nanoscale copper catalyst

Synthesis of copper nanoparticles

Copper nanoparticles capped with tetradecylphosphonate and suspended in hexane were synthesized following a literature method.[1] Briefly, 10 mL of trioctylamine (Sigma Aldrich, 98%) was heated in a 25 mL three neck flask equipped with a condenser and stir bar to 130 ^{o}C under argon for 1 h in order to dry the solvent. The trioctylamine was then cooled to room temperature; while keeping the flask purged with argon,123 mg of copper (I) acetate (Sigma Aldrich, 97%) and 139 mg of n-tetradecylphosphonic acid (TCI Synthesis, Lot No. 808002N09) were added to the trioctylamine. The solution was then rapidly heated to 180 ^{o}C under argon, swirled briefly to release any precursors adhered to the walls of the flask, and kept at this temperature for 30 min. The solution was rapidly heated to 270 ^{o}C and held at that temperature for 30 min. After cooling to room temperature, the copper particles were removed using air-free techniques and transferred to a glovebox. Just prior to electrode fabrication, 0.15 mL of the as-synthesized particles in trioctylamine was diluted with 0.75 mL of hexane, and then precipitated by adding 1.4 mL of isopropanol, under air-free conditions. The particles were separated by centrifuging at 8000 rpm for 8 min. The solvent was decanted under ambient conditions, and the particles were resuspended in 1 mL of hexane by vortexing. The volume of hexane in which the particles are resuspended can be changed in order to optimize the particle loading on glassy carbon; this is critical for achieving high methanation yields.

Glassy carbon plates (Type 2, Alfa Aesar) with 5.2 cm^2 of active surface area were polished using 1 μm alpha alumina (CH Instruments) and 50 nm gamma alumina (CH Instruments). The plates were rinsed with Milli-Q water, sonicated briefly, and blown dry with nitrogen. 600 μL of copper nanoparticles suspended in hexane were deposited on the substrate, which was then spun at 1000 rpm on a spin-coater for 60 s. 600 μL of ethanol was deposited on the substrate, which was allowed to sit for 30 s, and then spun at 1000 rpm for 60 s. Then, for trimethylsilyl chloride-treated electrodes, the substrate was covered in 600 μL of 2 wt % trimethylsilyl chloride in hexane and spun at 1000 rpm for 60 s, which was repeated once; then, the substrate was covered in 600 μL of ethanol and spun at 1000 rpm for 60 s, which was also repeated once.

Fabrication of evaporated copper electrodes

Glassy carbon plates were polished as described above. A thermal evaporator (Edwards Auto 500, FTM7) in an argon glovebox was used to evaporate copper films on the glassy carbon, using a high-purity copper source (99.9999%, Alfa Aesar). The films ranged in thickness from 3 to 21 nm, as measured using a quartz crystal monitor, and were deposited at a rate of approximately 3 nm/min. The plates were transferred under ambient conditions for use in the electrochemical cell.

Preparation of copper foil electrodes

High-purity copper foils were wet-sanded using 1500 grit sandpaper (Norton Blackice), rinsed with Milli-Q water, dipped in 8% nitric acid for 30 s, rinsed again with Milli-Q water, and then blown dry with nitrogen.

Microscopy of electrodes

As synthesized copper nanoparticles were imaged by drop-casting on a TEM grid (Electron Microscopy Sciences, CF-400-Cu) and acquiring images on a 200 kV Tecnai G2 20 S-TWIN with a Gatan SC200 CCD camera. After polarization, glassy carbon electrodes were rinsed with Milli-Q water and blown dry with nitrogen. Particles were transferred from the glassy carbon electrode to a TEM grid by placing a grid on top of the electrode and applying pressure to the grid using a glass microscope slide for a few seconds. SEM images of electrodes were acquired using a Zeiss Ultra 55 field emission scanning electron microscope with an InLens detector, 5 kV accelerating voltage, and 5 mm working distance.

Electrochemical methods

Electrochemical measurements were conducted in a two-compartment electrochemical flow cell fabricated from polychlorotrifluoroethylene (Kel-F), similar to a design used in the literature.[2] The working electrode compartment and counter electrode compartment, which each had an electrolyte volume of 5 mL and a gas headspace of ~1 mL, were separated by a Selemion membrane (AMV, AGC Engineering). A Ag/AgCl reference electrode (BASi, RE-6), which was stored in saturated KCl when not in use, was used; all measured potentials were converted to the RHE scale. The current densities measured for nanoparticle electrodes were normalized by the copper surface area; the surface area was determined by measuring the diameter of particles using SEM and calculating their surface area by treating them as spheres. For copper foils, the geometric surface areas were used, such that the reported current densities serve as upper bounds for the activity of copper foils. 0.1 M $NaHCO_3$ in Milli-Q water was used as the electrolyte, which was prepared by bubbling CO_2 (Praxair, CD M-50, >99%) through a solution of half the molarity of Na_2CO_3 (99.9999%, Sigma Aldrich), producing a solution of pH 6.8 after approximately 2 h. The electrochemical cell was continuously purged with CO_2 at a flow rate of 20 mL/min and a pressure of 1.2 atm; cells were purged for at least 5 min following assembly and before electrochemical polarization. For the experiments where CO_2 partial pressure was varied, the total flow rate and pressure of CO_2 were kept constant, while adding in a diluent stream of argon. Potentiostatic experiments were conducted by stepping to the desired potential, holding at that potential for 10 min, and sending a sample to the gas chromatograph (SRI Instruments, MG #3 Configuration) at the end of the 10 min interval. The gas chromatograph was equipped with TCD and FID detectors, a methanizer, and Molsieve 13x and Hayesep D columns.

Morphological evolution in the absence of carbon dioxide

We polarized copper nanoparticles supported on glassy carbon in 0.1 M potassium phosphate buffer (pH 7) under argon gas in order to understand how the morphological evolution proceeds in the absence of carbon dioxide; we find that the final morphology is similar with and without carbon dioxide (Figure A.1.1).

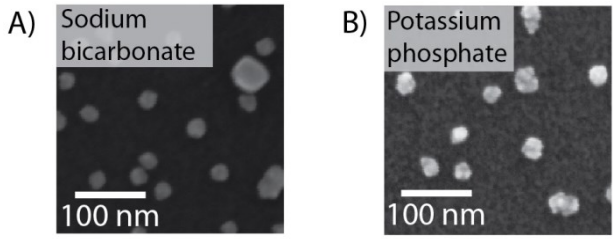

Figure A.1.1. SEM of n-Cu/C electrode following polarization for 10 minutes at -1.25 V in (a) CO_2 saturated sodium bicarbonate and (b) Ar saturated potassium phosphate (pH 7), demonstrating that the morphological evolution is similar in both buffers.

Electrode stability over time

The relative stability of the electrodes over time was quantified by plotting the normalized current expressed as a percentage (Figure A.1.2).

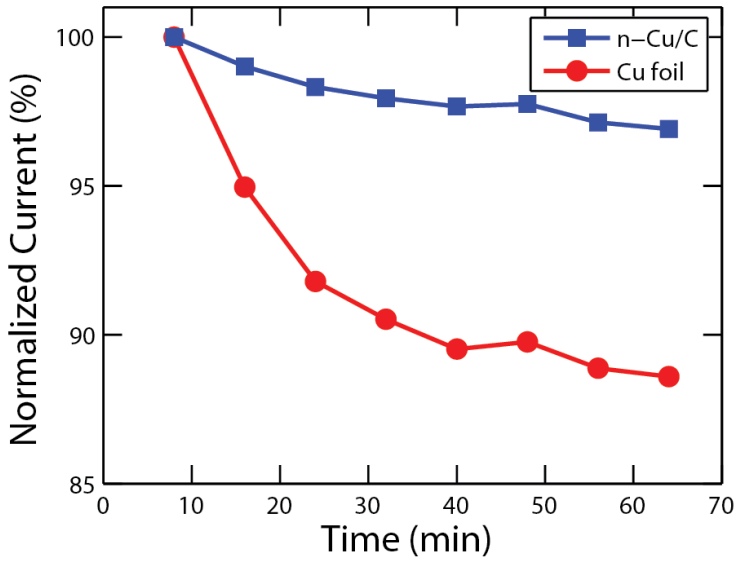

Figure A.1.2. Normalized current for n-Cu/C and copper foil expressed as a percentage.

Dependence of methanation current on bicarbonate concentration

The n-Cu/C catalyst shows no clear order dependence on the concentration of the sodium bicarbonate buffer (Figure A.1.3). The optimal buffer concentration for methanation activity on n-Cu/C is at approximately 130 mM sodium bicarbonate, at which we achieve a Faradaic efficiency for methanation of 86%. The methanation current on the copper foil catalyst exhibits a clearer order dependence on bicarbonate of 1.56 ± 0.03.

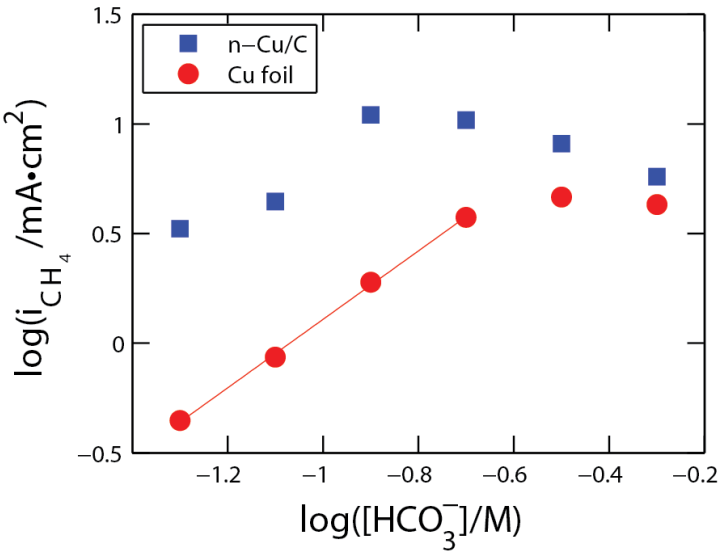

Figure A.1.3. Methanation current density as a function of concentration of sodium bicarbonate buffer, for both n-Cu/C and copper foil catalysts at -1.25 V.

Faradaic efficiencies

We have quantified the Faradaic efficiencies for minor products, including CO and C_2H_4, on n-Cu/C (Figure A.1.4).

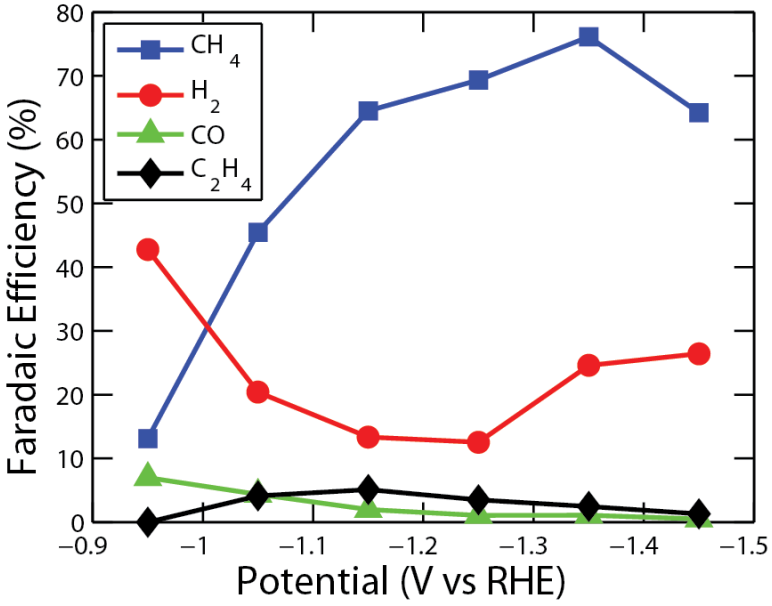

Figure A.1.4. Faradaic efficiencies for CH_4, H_2, CO, and C_2H_4 on n-Cu/C.

Surface coverage of CO_2 radical

For the pre-equilibrium step, the currents in the forward and reverse direction are equal, and we may write[3]:

$$k_1 p_{CO_2}(1-\theta)\exp\left(\frac{\beta F\eta}{RT}\right) = k_{-1}\,\theta\exp\left(\frac{-(1-\beta)F\eta}{RT}\right) \quad \text{(A.1.1)}$$

where k_1 and k_{-1} are the forward and reverse rate constants, respectively, for the pre-equilibrium step, p_{CO2} is the partial pressure of CO_2, θ is the surface coverage of the adsorbed CO_2 radical as a fraction of the total sites available for CO_2 radical binding, β is the symmetry factor, F is Faraday's constant, η is the overpotential, R is the gas constant, and T is the temperature. Equation S1 can be rearranged yielding:

$$\frac{\theta}{1-\theta} = K_1 p_{CO_2}\exp\left(\frac{F\eta}{RT}\right) \quad \text{(A.1.2)}$$

where K_1 is the equilibrium constant for the pre-equilibrium step. In the limit that $\theta \ll 1$, we obtain:

$$\theta = K_1 p_{CO_2}\exp\left(\frac{F\eta}{RT}\right) \quad \text{(A.1.3)}$$

Excluding alternative mechanisms

The gathered electrochemical data allows us to exclude several potential mechanisms (Table A.1.1), following the same type of derivation as shown in the manuscript.

Table A.1.1. Alternative mechanisms for the early steps of CO_2 reduction and the corresponding Tafel slope and order dependence of methanation current on p_{CO2}, demonstrating that these mechanisms are inconsistent with the experimental data.

Mechanism	**Order dependence on p_{CO2}**	**Tafel Slope**
$CO_2 + e^- \overset{RLS}{\rightarrow} CO_2^{-\cdot}{}_{ads}$	1	120 mV/decade
$CO_2 + e^- \leftrightarrows CO_2^{-\cdot}{}_{ads}$ $2CO_2^{-\cdot}{}_{ads} \overset{RLS}{\rightarrow}$ ...	2	30 mV/decade
$CO_2 + e^- \leftrightarrows CO_2^{-\cdot}{}_{ads}$ $CO_2^{-\cdot}{}_{ads} + CO_2 + e^- \overset{RLS}{\rightarrow}$ ...	2	40 mV/decade

A.2. Supporting information for dendritic assembly of gold nanoparticles during fuel-forming electrocatalysis

Synthesis of gold nanoparticles

Gold nanoparticles were produced by sodium borohydride reduction of an aqueous solution of tetrachloroauric acid with a polymeric dodecylthioether end-functionalized poly(methacrylic acid) ligand, based on a previously published protocol.[4]

Briefly, the dodecylthioether end-functionalized poly(methacrylic acid) was prepared by adding 5 g methacrylic acid, 1.17 g dodecanethiol, and 95 mg 2,2'-azobisisobutyronitrile to 25 mL of ethanol in a 3 neck flask with a reflux condensor. The solution was heated to 75 ^{o}C under argon for 5 hours with stirring. Once the solution cooled to room temperature, the polymer was precipitated using cold diethylether and collected by filtration on a Buchner funnel. The product, dodecylthioether end-functionalized poly(methacrylic acid), was allowed to dry under vacuum at 45 ^{o}C overnight. The polymeric stabilizer was dissolved in Milli-Q water (Millipore) at a concentration of 66 mg/mL.

17 μL of the polymeric stabilizer solution was added to 20 mL of a 0.5 mM solution of tetrachloroauric acid in Milli-Q water. After allowing the solution to stir for 1 hour, 2 mL of a freshly prepared 50 mM solution of sodium borohydride in Milli-Q water was injected into the gold-polymer solution; the injection was done in two aliquots of 1 mL each in rapid succession. The solution was allowed to stir for 4 hours.

The aqueous particles were then ligand exchanged to dodecanethiol or dodecylamine. 10 mL of the aqueous gold nanoparticle solution was mixed with 10 mL of 1% v/v dodecanethiol in ethanol. The solution was allowed to stir overnight. Then, after adding 2 mL of hexane to the solution, it was mixed by inversion, and centrifuged at 2000 rpm for 2 minutes to create a clean interface between the two phases. The top hexane layer containing the gold nanoparticles was removed using a pipette. To prepare dodecylamine-capped particles, the same procedure was used as for dodecanethiol-capped particles, except that the 1% v/v dodecanethiol in ethanol was substituted with 1% w/w dodecylamine in ethanol.

Preparation of working electrodes

Glassy carbon plates (Type 2; Alfa Aesar) were used as electrodes. The electrodes were polished using 1500 grit sandpaper (Norton Blackice), 1 μm alpha alumina (CH Instruments), and 50 nm gamma alumina (CH Instruments). The electrodes were then sonicated in Milli-Q water for 30 seconds and blown dry with nitrogen.

Electrodes consisting of only gold nanoparticles on glassy carbon were prepared as follows. Gold nanoparticles in hexane were diluted to an optical density of 0.32 at the absorption maximum of 515 nm. The glassy carbon substrate was placed on a spin-coater, covered in gold nanoparticle solution (100 μL/cm^2) while stationary, and then immediately spun at 1000 rpm for 60 seconds. The substrate was then covered in ethanol (100 μL/cm^2) while stationary for 30 seconds and spun at 1000 rpm for 60 seconds in order to remove any excess ligand.

Electrodes consisting of a composite of gold nanoparticles, high surface area carbon, and a binder were prepared as follows. Dodecanethiol-capped gold nanoparticles in hexane were cleaned by adding 1.5 times the volume of ethanol and centrifuging at 8000 rpm for 6 minutes and then redispersing in hexane. 600 μL of gold nanoparticles in hexane of OD 2.2 were then mixed with 60 μL of a 1 mg/mL solution of >99.9% purity acetylene black (Alfa Aesar) in hexane and 6 μL of a 1 mg/mL solution of poly(vinylidene fluoride) (VWR) in hexane. The mixture was sonicated for 10 minutes. The glassy carbon substrate was placed on a spin-coater, covered in this mixture (100 μL/cm^2) while stationary, and then immediately spun at 1000 rpm for 60 seconds.

Gold foil working electrodes of 99.9975% purity (Alfa Aesar) were polished using 1500 grit sandpaper, dipped in freshly prepared aqua regia for 30 seconds, rinsed with Milli-Q water, and then blown dry with nitrogen. Dodecanethiol SAMs on gold foils were prepared by then immersing the gold foil in a 10 mM dodecanethiol solution in ethanol for 1 hour, rinsing the foil with ethanol thoroughly, and then blowing dry with nitrogen.[5]

Electrochemical analysis

All electrochemical measurements were performed using a CH Instruments 760D potentiostat and a three electrode setup, consisting of a 99.99% platinum foil (Alfa Aesar) counter electrode, Ag/AgCl reference electrode (BASi, RE-6) stored in saturated KCl, and the desired working electrode. The reference electrode was positioned at the edge of the working electrode about 2 mm from its surface. In a typical experiment using 0.1 M $NaHCO_3$, the IR loss in the cell was approximately 5 Ω which was compensated for using the automated IR compensation algorithm built into the potentiostat. All measured potentials were converted to the reversible hydrogen electrode scale (RHE) scale using the following formula:

$$V_{RHE} = V_{Ag/AgCl} + 0.2 + 0.059 * pH \qquad \text{(A.2.1)}$$

where V_{RHE} is the potential versus RHE and $V_{Ag/AgCl}$ is the potential versus Ag/AgCl.

The defined electrode area for the counter and working electrodes was 3.5 cm^2. A two-compartment electrochemical cell was fabricated from polychlorotrifluoroethylene (Kel-F), with an electrolyte volume of 15 mL and a gas headspace of 3 mL in each chamber. CO_2 was bubbled through the working electrode chamber at 6 mL/min and a pressure of 1.2 atm. The counter electrode chamber was open to atmosphere. The two compartments were separated by a Selemion membrane (AGC Engineering). The standard electrolyte used was 0.1 M $NaHCO_3$, except where noted; the electrolyte was produced by bubbling CO_2 through a Na_2CO_3 (Sigma Aldrich, 99.9999% purity, batch number BCBJ6089V) solution of half the molarity until the solution was saturated, as determined by measuring the pH. The pH of the saturated solution was 6.8. For experiments conducted in 0.1 M H_2SO_4, 0.5 M H_2SO_4, 0.1 M KOH, and 0.5 M KOH as the electrolyte, argon was continuously bubbled through the electrolyte at 10 mL/min. The measurements were conducted at room temperature. Potentiostatic measurements were conducted by first purging the electrochemical cell using CO_2 for 10 minutes at open circuit and then stepping to the desired potential (Figures A.2.1 and A.2.2).

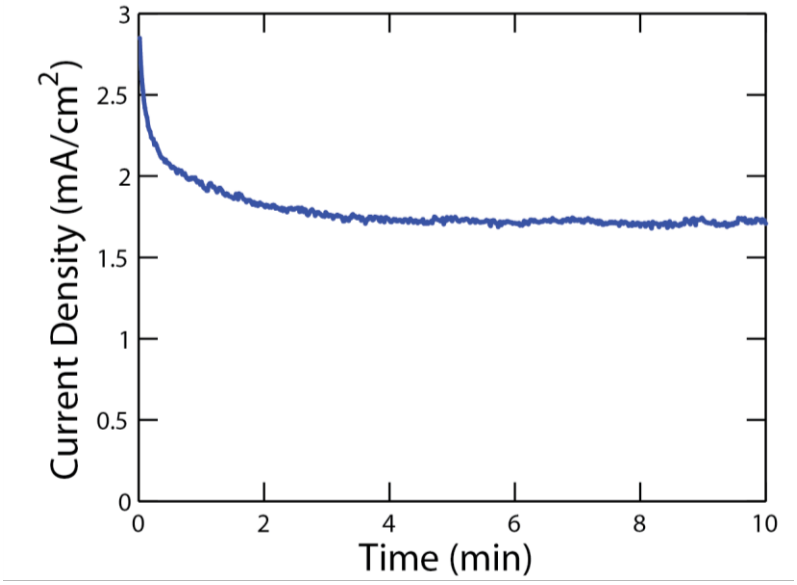

Figure A.2.1. Current density versus time for dodecanethiol-capped gold nanoparticles polarized to -1.2 V in 0.1 M $NaHCO_3$ buffer.

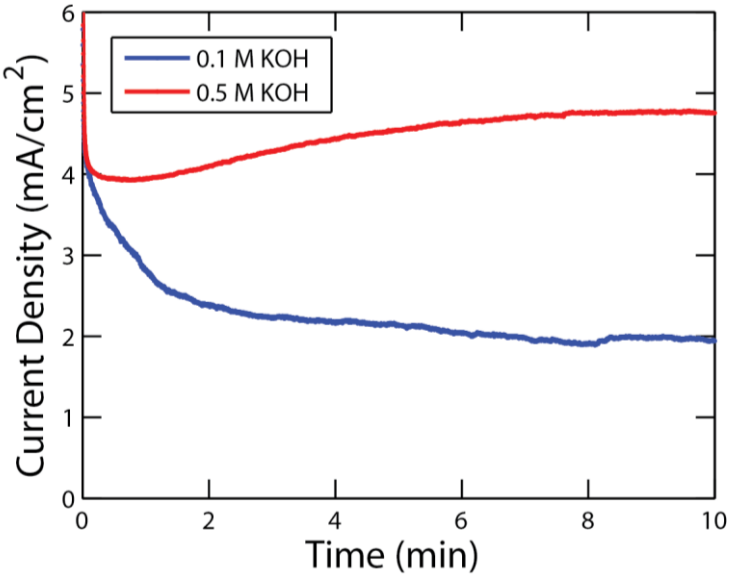

Figure A.2.2. Current density versus time for dodecanethiol-capped gold nanoparticles polarized to -1.2 V in 0.1 and 0.5 M KOH.

Although the initial currents are similar in potassium hydroxide buffer at 0.1 M and 0.5 M concentrations, the currents at the end of the polarization step are much greater in 0.5 M KOH than 0.1 M KOH, reflecting the greater catalyst surface area in the higher electrolyte strength due to reduced dendritic assembly.

Plots of current versus voltage were determined by stepping through the range of potentials beginning from -0.2 V and ending at -1.2 V, holding at each potential for 20 seconds, recording the stable current at the end of each 20 second step, and then immediately repeating this current staircase ten times total.

From the particle coverage determined by scanning electron microscopy (SEM) and the average particle diameter determined by transmission electron microscopy (TEM), it was calculated that the surface area of the gold nanoparticles prior to polarization is approximately one seventh that of the geometric area of the electrode. This calculated surface area was used to correct the measured geometric current densities for the dodecanethiol-capped gold nanoparticles so that the current density per unit area of gold could be determined. Because the surface area of the gold nanoparticles decreases during polarization, the corrected current density serves as a lower-bound for the current per unit area of gold.

We observe comparable current densities for pristine gold foils and gold foils decorated with dodecanethiol self-assembled monolayers (SAM) suggesting that adsorbed thiols do not strongly inhibit charge transfer at the gold surface under strongly reducing conditions (Figure A.2.3). Dodecanethiol-capped nanoparticles display higher current densities than dodecylamine-capped nanoparticles (Figure A.2.3), consistent with their higher surface area (Figure A.2.6). While dodecanethiol-capped gold nanoparticle electrodes display lower geometric current densities than gold foils, the activity normalized to the initial

surface area of the nanoparticles (as determined by SEM, see above) is slightly greater than that of the foils (Figure A.2.3). This surface area normalized activity likely represents a lower bound because particle coalescence decreases the electroactive surface area over the course of the measurement. The products of CO_2 reduction at gold foil electrodes have been thoroughly characterized at a potential of -0.74 V, at which the faradaic efficiencies are 87% CO, 10% H_2, and <1% HCOOH.[6] In contrast, the faradaic efficiencies of dodecanethiol-capped gold nanoparticles are 49% CO, 48% H_2, and <1 % HCOOH. Although the selectivity for CO is lower compared to gold foils[6] and oxide-derived gold nanoparticles,[7] the mixture of CO and H_2 can be used as synthesis gas. In comparison to other metals, the dodecanethiol-capped gold nanoparticles exhibit higher Faradaic efficiencies for reducing CO_2 to CO than palladium (28.3%) and gallium (23.2%) but lower than that of silver (81.5%) and zinc (79.4%).[6]

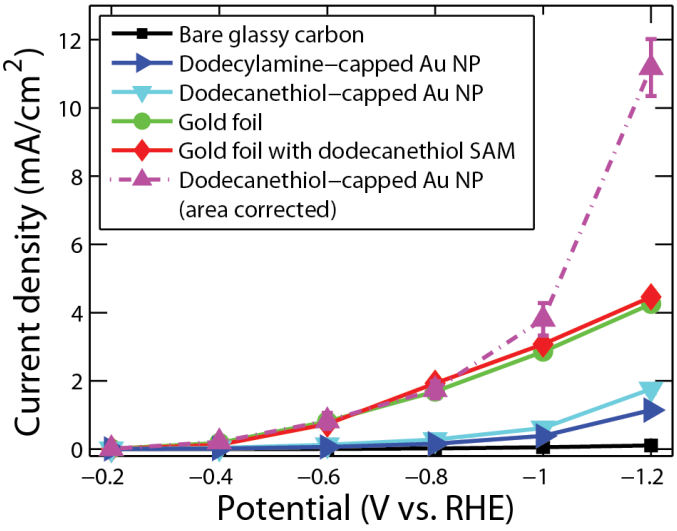

Figure A.2.3. Steady-state geometric current density versus potential in 0.1 M $NaHCO_3$ buffer for a bare glassy carbon electrode, dodecanethiol- and dodecylamine-capped gold nanoparticles (Au NP) cast on a glassy carbon support, and a gold foil with and without a dodecanethiol SAM. For the dodecanethiol-capped gold nanoparticles, the current density is also plotted after correcting for the initial surface area of the gold.

Product analysis using gas chromatography and NMR

Gas phase products in the reactor effluent were quantified using a SRI Gas Chromatograph with Hayesep D and MoleSieve 13x columns, a methanizer, and TCD and FID detectors. Formic acid was quantified using a Bruker AVB-400 NMR Spectrometer, following a previously published protocol.[2] Briefly, following polarization at -0.74 V for 10 minutes (total charge passed is approximately 0.5 C), 720 µL of the electrolyte was mixed with 80 µL of a standard solution of 10 mM DMSO and 50 mM phenol in D_2O in an NMR tube. A proton spectrum was acquired for 1 hour. The concentration of formic acid was determined by measuring the ratio of the area of the formic acid singlet at 8.33 ppm versus the phenol triplet at 7.2 ppm and comparing to the ratio of areas observed for standard solutions.

Microscopy of electrodes

Following polarization, electrodes were rinsed with Milli-Q water and blown dry with nitrogen. SEMs of electrodes were acquired using a Zeiss Ultra 55 Field Emission Scanning Electron Microscope with an InLens detector, 5 kV accelerating voltage, and 5 mm working distance.

As-synthesized gold nanoparticles were imaged by casting on a TEM grid (Electron Microscopy Sciences, CF-400-Cu). Dendrites were transferred to a TEM grid by placing the grid on a glassy carbon substrate and applying gentle pressure with a glass microscope slide for a few seconds. TEMs were acquired using a 200 kV Tecnai G2 20 S-TWIN with a Gatan SC200 CCD camera.

X-Ray photoelectron spectroscopy

X-Ray photoelectron spectroscopy was conducted on electrodes prior to and following polarization at -1.2 V for 10 minutes in 0.1 M $NaHCO_3$. A Kratos Analytical AXIS Ultra DLD X-Ray Photoelectron Spectrometer was used with an Al Kα source. 5 sweeps with a 50 meV step size and 300 ms dwell time were used to record the Au 4f and S 2p spectra (Figure A.2.4), and 1 sweep with a 1000 meV step size and a 100 ms dwell time was used to record the survey spectra (Figure A.2.5). The sulfur peak is still present following polarization (Figure A.2.4), consistent with the fact that the alkanethiol influences assembly behavior even beyond the thiol stripping potential of -0.6 V. We anticipate that although the alkanethiol may be soluble in the boundary layer due to the locally increased pH in the vicinity of the electrode under polarization, when the polarization is released, the thiols physisorb onto the electrode surface.

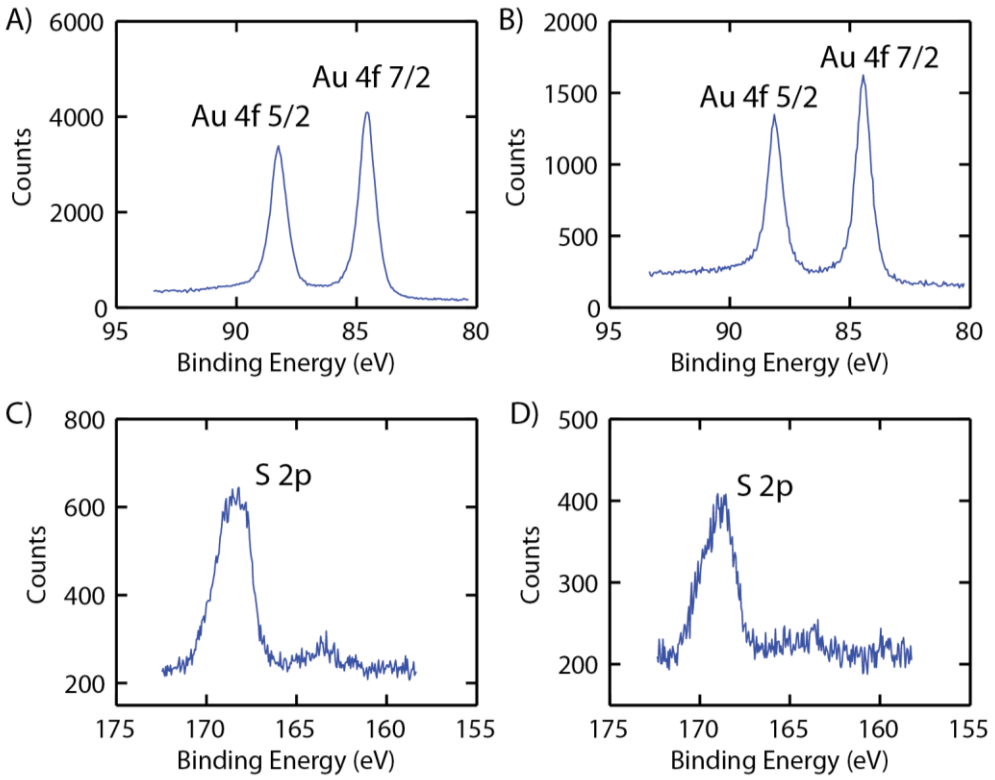

Figure A.2.4. XPS of gold nanoparticles on glassy carbon before and after polarization at -1.2 V for 10 minutes in 0.1 M $NaHCO_3$. Au 4f spectrum (a) before and (b) after polarization, and S 2p spectrum (c) before and (d) after polarization.

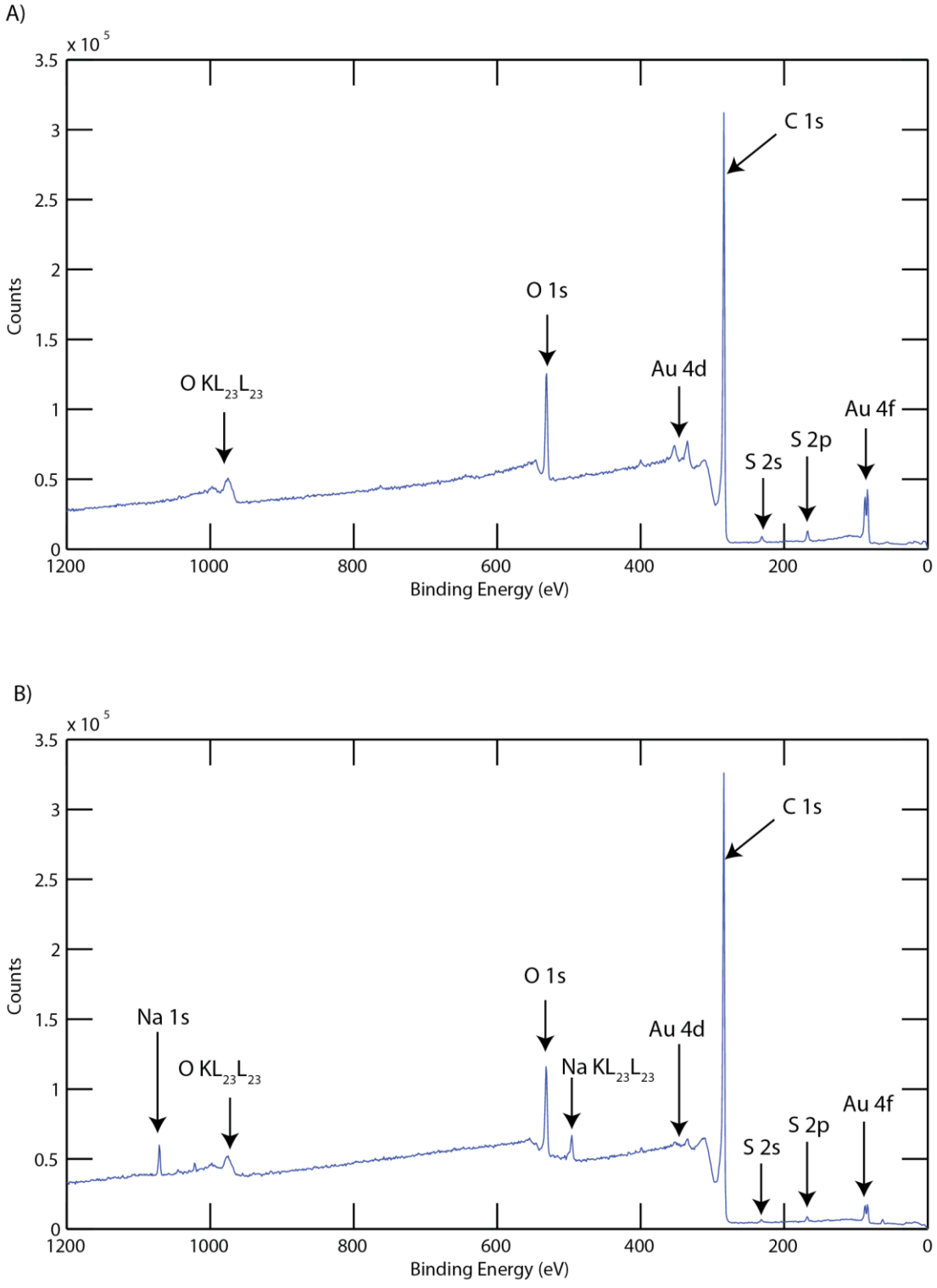

Figure A.2.5. XPS survey of gold nanoparticles on glassy carbon (a) before and (b) after polarization at -1.2 V for 10 minutes in 0.1 M $NaHCO_3$.

Comparison of dodecylamine and dodecanethiol

Solubility arguments can also be used to rationalize why dodecanethiol is a more effective ligand for retarding dendritic assembly relative to dodecylamine (Figure A.2.6). Dodecylamine is charged at intermediate pH values and is therefore more soluble than dodecanethiol under the conditions of electrochemical CO_2 reduction catalysis and less effective at hindering particle fusion.

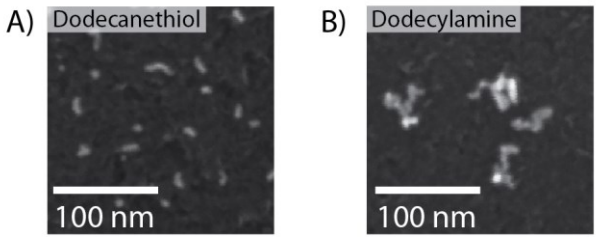

Figure A.2.6. SEMs of dendrites produced from (a) dodecanethiol- and (b) dodecylamine-capped gold nanoparticles after polarization at -1.2 V for 10 minutes in 0.1 M $NaHCO_3$ buffer.

Random walk simulations

Random walk simulations were conducted using Matlab (Mathworks, R2013b). A 500 x 500 square lattice with periodic boundary conditions was randomly populated with 10,000 isolated particles, corresponding to a fractional coverage of 0.04. For each particle, a pair of random coordinates were generated and a particle was placed at that site if the site was not occupied and the site had no neighbors in the four surrounding sites; if these criteria were not satisfied, a new set of random coordinates for the particle were generated until these criteria were satisfied. The simulation was conducted on a square lattice, as it has been previously shown that the results obtained on square lattices are comparable to those obtained on off-lattice simulations.[8]

An individual particle or dendrite was randomly selected, using a random number generator, and took a unit step with a probability that is inversely proportional to its size, 1/n, where n is the number of particles in the dendrite. This scaling assumes a constant average force associated with the particle displacements, which when divided by the mass of a dendrite, provides the acceleration of the particle. The mass of a dendrite is directly proportional to the number of particles in the dendrite. For a uniform acceleration beginning from zero velocity, the displacement is then inversely proportional to the number of particles in the dendrite. There were five equally weighted outcomes for a step, including staying at the current site or moving to any of the four neighboring sites. Following a step, if a particle or dendrite came into contact with another particle or dendrite, the two fused irreversibly with a probability given by the sticking coefficient multiplied by the number of nearest neighbors; if there were *n* contact points between a dendrite that collided with another dendrite, then the sticking coefficient was multiplied by *n* to determine the probability of a fusion event. If the fusion event did not occur, the

particle was returned to its original location before it took a unit step, prior to the collision.

In all cases, because the fusion events were irreversible, there were no further changes to the internal structure of a dendrite following a fusion event. The simulations were halted when the system no longer evolved in time, which was the case when dendrites could not move, or once the average of the maximum caliper diameters of the dendrites was the same as the average of the maximum caliper diameters after 100 minutes of polarization at -1.2 V. The maximum caliper diameter of the dendrites were calculated by measuring the distance between the two furthest points within a single dendrite and the area was calculated by counting the number of particles contained in the dendrite.

Image analysis

SEMs of dendrites after 100 minutes of polarization at -1.2 V were analyzed in order to determine the maximum caliper diameter and area of individual dendrites. The Image Processing Toolbox in Matlab was used to identify individual dendrites in the image by finding the edge of each dendrite using the Sobel method, dilating the edge, and filling interior gaps – this methodology is described in detail in in the Matlab R2013b Image Processing Toolbox documentation, in the example titled “Detecting a Cell Using Image Segmentation.” The maximum caliper diameter was calculated by determining the distance between the two furthest points within the dendrite and the area was calculated as the number of pixels within the dendrite.

A.3. Supporting information for tunable localized surface plasmon resonances in tungsten oxide nanocrystals

Synthesis

The synthesis of tungsten oxide rods was carried out by adapting a procedure reported by Yella et al.[9] All steps were carried out with standard Schlenk line techniques. 12.5 mL of oleic acid (Sigma Aldrich, Technical Grade, 90%) and 17.5 mL of trioctylamine (Sigma Aldrich, 98%) were mixed in a 100 mL 3-neck flask and degassed under vacuum at 150 ^{o}C for 1 h. The flask was then placed under flowing Ar and heated to 335 ^{o}C for 3 h. It is important to use a bump trap as the contents of the flask could bump during this step. The solution was then cooled to 315 ^{o}C and 0.5 mL of tungsten (V) ethoxide (Alfa Aesar, 94%) was rapidly injected; the solution boiled vigorously following the injection. The reaction was held at 315 ^{o}C for 5 min and then cooled to room temperature before exposing to air. 15 mL of ethanol was added to the reaction, followed by centrifugation at 4000 rpm. The pellet was then resuspended in acetone and centrifuged at 4000 rpm; the acetone washing step was repeated. After decanting the solvent, the final product was left as a moist powder and stored at ambient conditions.

Characterization

The powder was resuspended in various polar solvents, including *N*-methylpyrollidone, dimethylformamide, acetonitrile, and methanol, with the assistance of brief sonication. Spectra were acquired using a Shimadzu UV3600 spectrophotometer. Transmission electron microscope (TEM) images were taken with a 200 kV Tecnai G220 S-TWIN with a Gatan SC200 CCD camera. X-Ray Diffraction (XRD) patterns were acquired with a Bruker GADDS Hi-Star D8 diffractometer using Co Kα radiation (1.79 Å). The patterns were background-subtracted and matched with standard patterns in the Joint Committee of Powder Diffraction Standards (JCPDS) Database.

Absorption due to short and long axis modes as a function of aspect ratio

We calculated the absorption due to the short- and long-axis modes as a function of aspect ratio (Figure A.3.1). We found that the short-axis mode shifts over a small wavelength range due to changes in the aspect ratio. However, the aspect ratio significantly impacts the energy of the long-axis mode. We found that Mie-Gans theory predicts that the peak of the long-axis mode may be observed for shorter aspect ratios; for longer aspect ratios, the long-axis mode contributes to the optical absorption at very small energies but does not pass through a maximum.

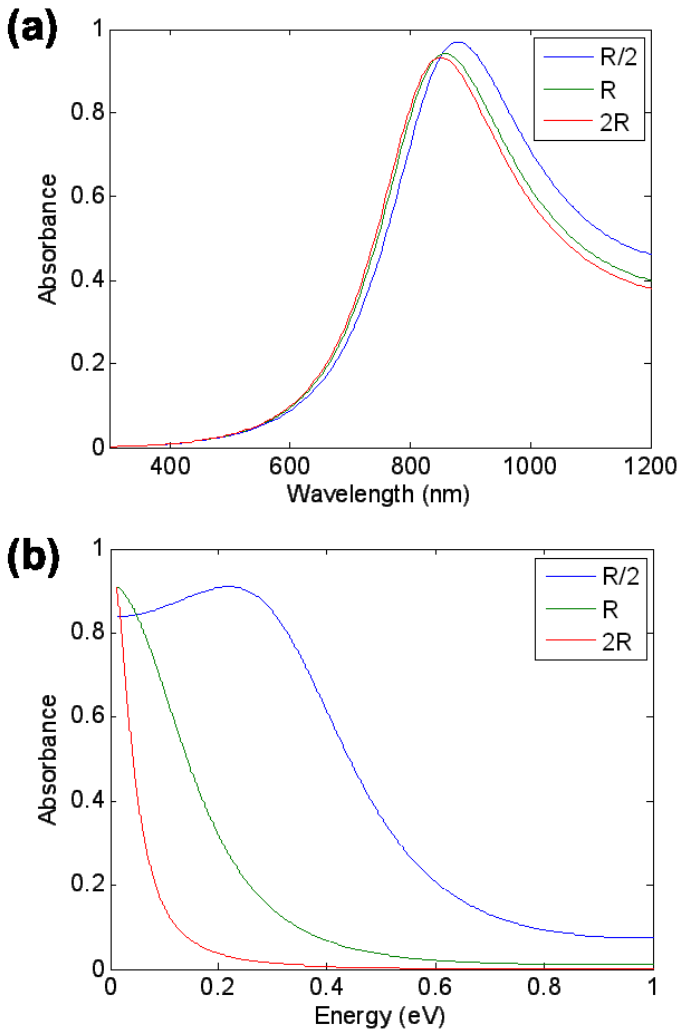

Figure A.3.1. Calculated absorption of tungsten oxide nanorods for aspect ratios of R/2 = 5.5, R = 11, and 2R = 22, for both (a) the short-axis mode and (b) the long-axis mode. The x-axis in the plot of the short-axis mode is provided in units of wavelength. The plot of the long-axis mode is normalized at the maximum absorption for each individual curve and the x-axis is provided in units of energy to facilitate visualization of the data.

High resolution transmission electron microscopy

High resolution TEM (HRTEM) images of tungsten oxide nanocrystals were acquired both before and after heating in NMP at 175 ºC for 6 minutes. The HRTEM demonstrates that the growth direction is along the (0 0 4) direction, which has a lattice spacing of 4.1 Å, similar to the experimentally observed values (Figure A.3.2). We see that fringing is evident both before and after heating in NMP, suggesting that some degree of crystallinity is retained during the heating process.

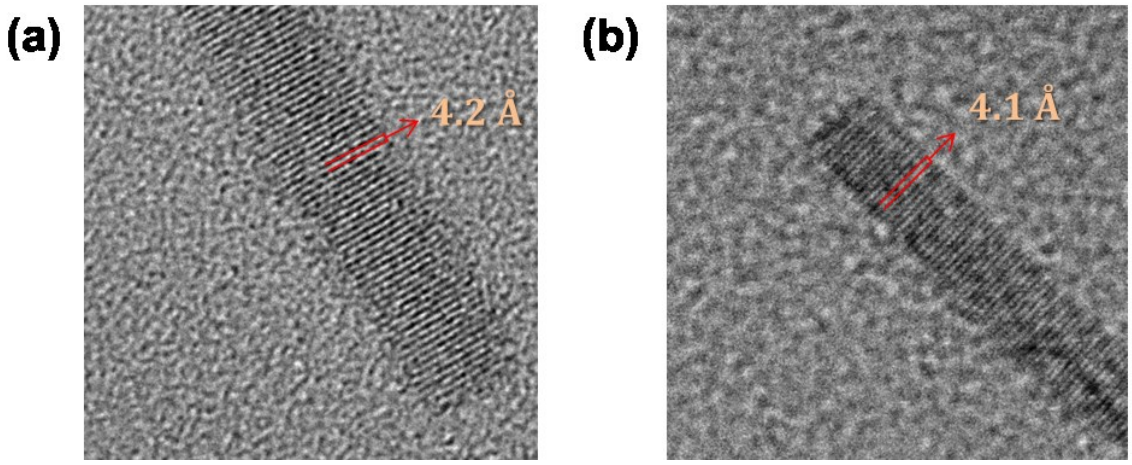

Figure A.3.2. **HRTEM of tungsten oxide nanorods** (a) before and (b) after heating in NMP at 175 ºC for 6 minutes.

Size distribution

The length and width distributions of the tungsten oxide nanorods were determined by measuring the dimensions of more than 50 particles using ImageJ (Figure A.3.3). The average width was 5.4 nm and the average length was 62 nm. The ratio of the length and width leads to an aspect ratio of R = 11.

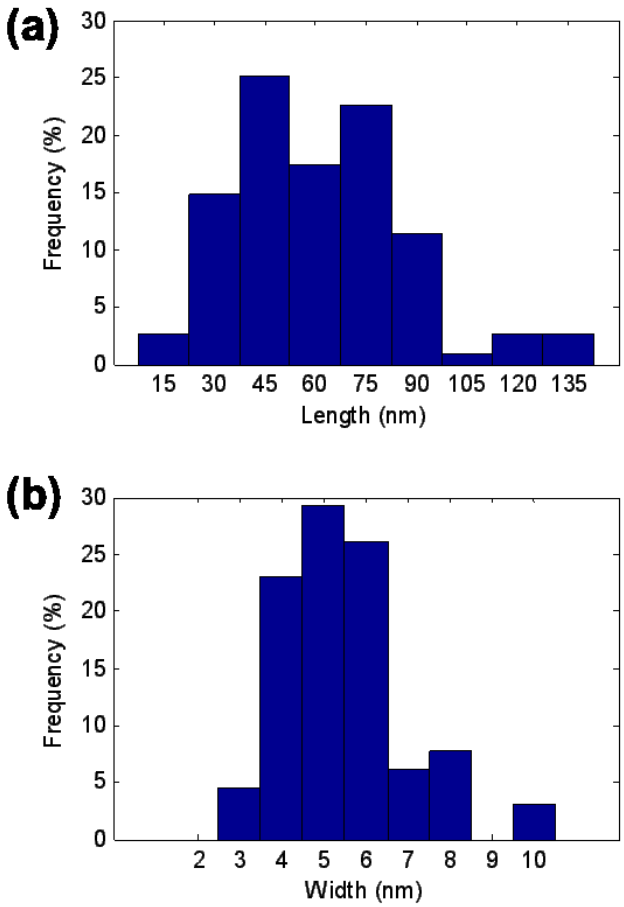

Figure A.3.3. **(a) Length and (b) width distributions of tungsten oxide nanorods.**

A.4. Supporting information for redox tunability of the plasmonic mode of copper sulfide nanocrystals

Synthesis and characterization of copper (I) sulfide nanorods

Copper (I) sulfide nanorods were prepared by the cation exchange of CdS nanorods with excess Cu ions. The method yields nanorods with negligible copper vacancies, as established in a past study.[10]

CdS nanorods were synthesized as per a procedure adapted from Sadtler et al.[11] 0.207 g of CdO, 1.08 g of octadecylphosphonic acid (ODPA), 0.010 g of propylphosphonic acid (PPA), and 2.75 g of trioctylphosphine oxide (TOPO) were loaded into a 25 mL three-neck flask and heated to 120°C for 1 h under vacuum. The mixture was heated to 320°C under flowing argon to produce an optically clear solution. After the CdO completely dissolved, the solution was cooled to 120°C and put under vacuum for 1 h for the removal of water, after which it was heated to 320°C under flowing Ar. At this time, 2 g of TOP was injected and the flask was allowed to return to 320°C. TOP:S was prepared by reacting equimolar amounts of TOP and elemental sulfur under an inert atmosphere. 1.3 g TOP:S was rapidly injected into the flask at 320°C. The reaction temperature was adjusted to 305°C, and the reaction proceeded for 20 min, followed by an additional injection of 0.65 g TOP:S. The reaction was stopped after a total of 45 min by the removal of heat and the injection of 4 mL of anhydrous toluene once the reaction had cooled below 100°C. The nanorods were isolated and cleaned by a few cycles of precipitation with isopropanol/acetone as non-solvent and re-dissolution in toluene/hexane, with alternating addition of 1-2 mL of octylamine and nonanoic acid. Precipitation was achieved by centrifugation at 4000 rpm for 10-15 min. Typically, this procedure yields CdS nanorods approximately 4 nm in diameter and 50 nm in length.

Cation exchange was carried out at room temperature in an oxygen- and moisture-free environment in the glove-box. The Cd^{2+} concentration of the CdS nanorods was estimated from the absorbance (OD) of the sample at 400 nm as per the formula:[12]

$$[Cd^{2+}] \text{ in ppb} = 82043.2*OD - 694.9 \qquad (A.4.1)$$

We typically exchange a nanorod solution ($[Cd^{2+}] \leq 10^{-3}$ M) with a 20x molar excess of Cu^{+} (10x stoichiometric excess since each Cd^{2+} ion needs to be replaced by two Cu^{+} ions). In a typical reaction, a solution of 11 mg tetrakis(acetonitrile)copper(I) hexafluorophosphate (30 μmol Cu^{+}) in 1 mL methanol was added drop-wise to a vigorously stirred solution of the seeded rods (1.5 μmol Cd^{2+}) in 2 mL toluene. Methanol solvates the divalent Cd^{2+} more strongly compared to Cu^{+}, driving the Cu(I) exchange reaction forward. An immediate (< 1 s) color change to golden brown was observed on addition, following which the exchange reaction was allowed to proceed for a few minutes. The Cu_2S rods were precipitated out by addition of 1-2 mL of methanol and centrifugation at 4000 rpm for 20 min. The supernatant containing excess unreacted Cu^{+}, released Cd^{2+}, and surfactants was discarded and the nanorods were redispersed in 3 mL

tetrachloroethylene or carbon tetrachloride, both with high transmission throughout the near-infrared.

Electron microscopy

Transmission electron microscopy images of copper (I) sulfide nanorods were acquired on a FEI Tecnai G2 20 200 kV LaB_6 transmission electron microscope. Samples were prepared by drop-casting a few drops of the nanorod solution on amorphous carbon on Cu grids or ultrathin carbon (< 3 nm) over holey carbon film, followed by rinsing with methanol and drying in the glovebox. The nanorods are about 4 nm in width and 20-30 nm in length. Using electron microscopy, we find that the nanorods maintain their morphology and crystallinity throughout vacancy formation (oxidation) and reversal (reduction) processes.

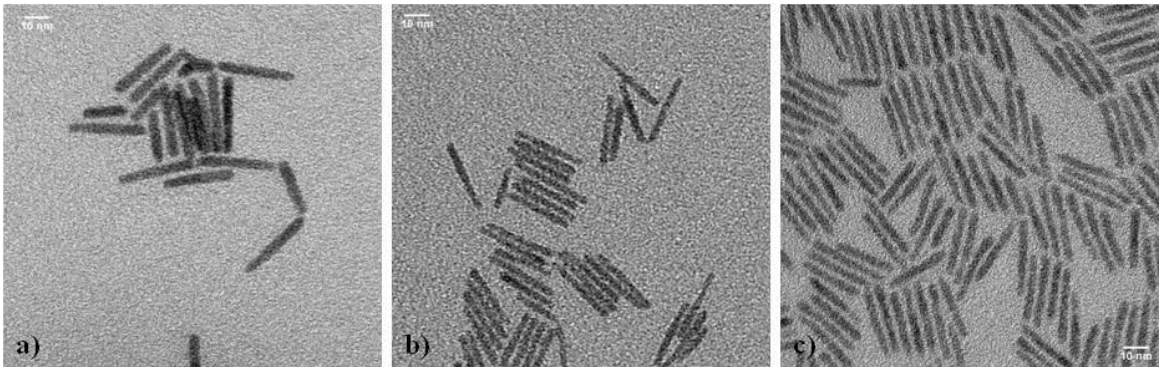

Figure A.4.1. TEM images before and after copper extraction and insertion. TEM images of (a) copper (I) sulfide nanorods obtained from cation exchange and (b) after amine treatment for creation of copper vacancies followed by (c) thiol treatment for filling of vacancies. The images show that the overall morphology of the nanorods is conserved throughout the copper vacancy formation and reversal processes. The scale bar represents 10 nm.

Optical spectra

UV-visible-NIR absorption spectra were acquired in infrared-transparent quartz cuvettes sealed to prevent exposure to oxygen or moisture. Spectra of the CdS nanorods were measured in toluene or hexane in the visible region (300-800 nm). Spectra of the copper (I) sulfide nanorods were measured in anhydrous tetrachloroethylene or carbon tetrachloride in the visible and near-infrared region (300-3300 nm). A Shimadzu UV-3600 scanning spectrophotometer (full range: 185–3300 nm) was used with 1-nm step size and the appropriate solvent as background. Nanorods obtained from exchange were ensured to have negligible absorption in the near-infrared region (1200-3000 nm), signifying that the nanorods are unoxidized and/or free of copper vacancies.

Electrical transistor measurements

All fabrication and measurement were carried out in an argon glovebox. Patterned gold electrodes were deposited onto p+-doped (<5 mW-cm) silicon wafers with 300 nm of gate oxide (Addison Engineering) using standard photolithography techniques. Contacts were comprised of a 5 nm titanium adhesion layer, topped with 45 nm of gold. Channel lengths and widths were 10 μm and 250 μm respectively. Nanocrystal thin-films were fabricated via layer-by-layer drop-casting with sequential ligand exchange. Dilute solutions of Cu_2S nanorods in hexane (<5 mg/ml) obtained from cation exchange were deposited onto transistor substrates and allowed to dry fully. To achieve ligand exchange, the films were dipped into a solution of 1 mM ethanethiol in ethanol. The process was repeated several times to build up a smooth thin film (~150 ± 50 nm, measured using a Tencor AS500 Profilometer) of nanoparticles.

Electrical measurements were conducted using a Keithley 2636a dual source-meter unit, controlled with a home-built LabView (National Instruments) program. Substrates were contacted using a home-built probe station enclosed in an argon glovebox. The oxidation steps were performed in air with continuous measurement on an open-air probe station. The reduction steps were performed in an argon glovebox.

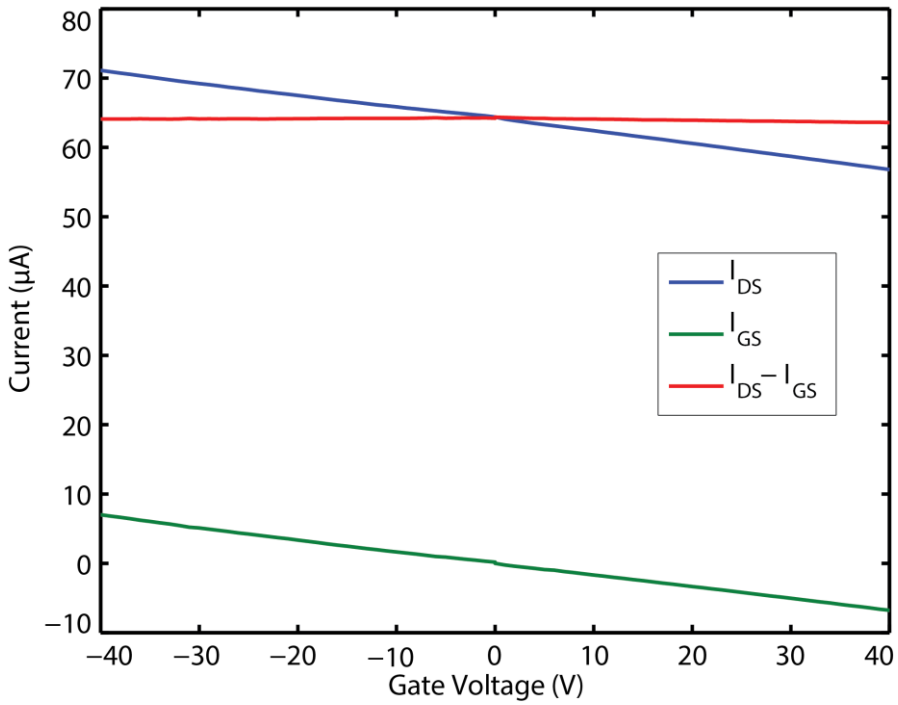

Figure A.4.2. Gate transconductance for a copper (I) sulfide nanorod film FET. Due to the high degree of doping within the film, the change in conductance induced by the gate is small and is overwhelmed by the gate leakage current, preventing extraction of field-effect mobilities. Source-drain bias is 1 V and contact length and width are 5 μm and 750 μm, respectively.

Formation of copper iodide and copper amine complex

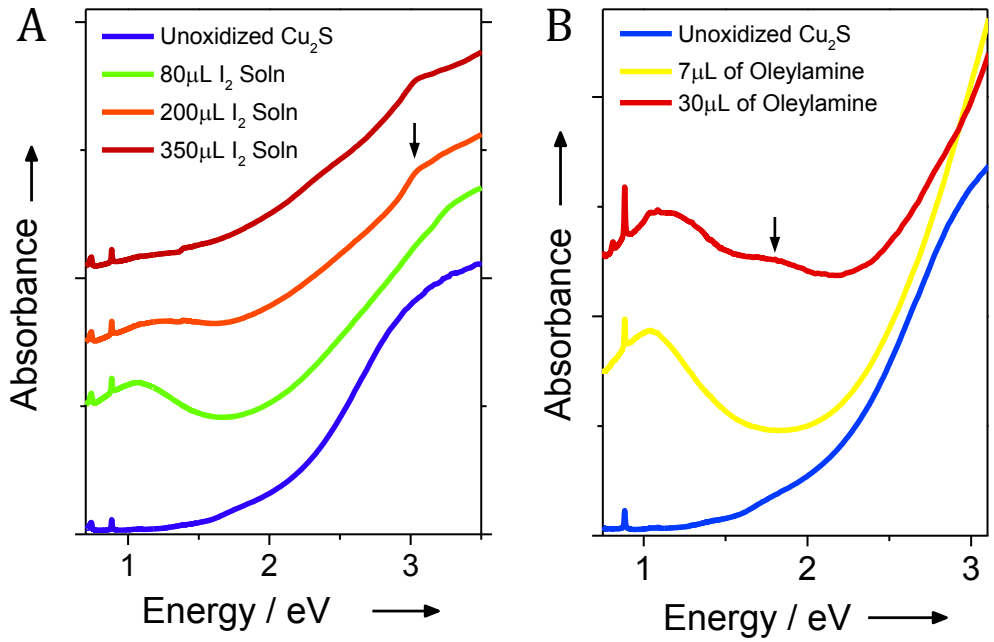

Figure A.4.3. Formation of copper iodide and copper amine complex. (a) Experimental spectra indicate that I_2 removes copper atoms from the copper(I) sulfide NRs through the formation of copper iodide. As I_2 is added, a NIR LSPR develops due to the creation of copper vacancies. Concomitantly, an absorption band attributable to copper iodide[13] develops at 3 eV (410 nm) as indicated by the arrow. The band becomes prominent when excess iodine is added, however the LSPR feature weakens, likely due to bulk conversion of copper(I) sulfide to copper iodide. (b) Similarly, oleylamine removes copper atoms from the lattice of the NRs by formation of a copper:amine complex. Upon addition of oleylamine, an LSPR develops. Simultaneously, a peak attributable to a copper-amine complex[14,15] develops at 1.8 eV (680 nm), as indicated by the arrow. Experiments were performed with copper(I) sulfide NRs dispersed in tetrachloroethylene in air-tight cuvettes. The sequence of spectra in each plot corresponds to a single titration. Where appropriate, spectra were scaled and overlayed for presentation.

Reversibility of LSPR absorption

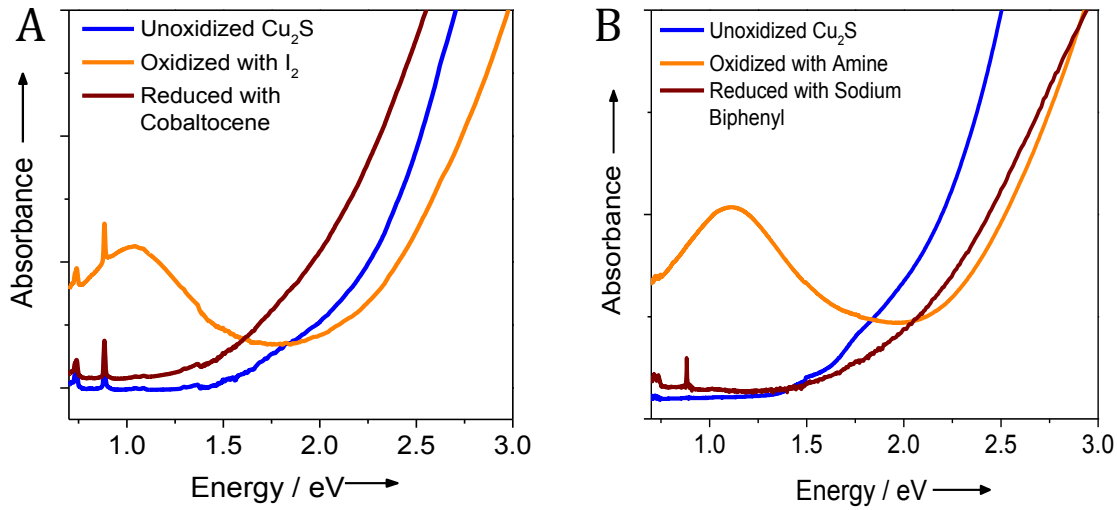

Figure A.4.4. Reversibility of LSPR absorption. The NIR LSPR can be completely reversed through the addition of strong reducing agents such as (a) cobaltocene and (b) sodium biphenyl, which inject electrons into the NR lattice filling vacancies. Experiments were performed with copper(I) sulfide NRs dispersed in tetrachloroethylene in air-tight cuvettes. The sequence of spectra in each plot corresponds to a single titration.

Effect of copper oxide shell on LSPR spectra of copper(I) sulfide nanorods

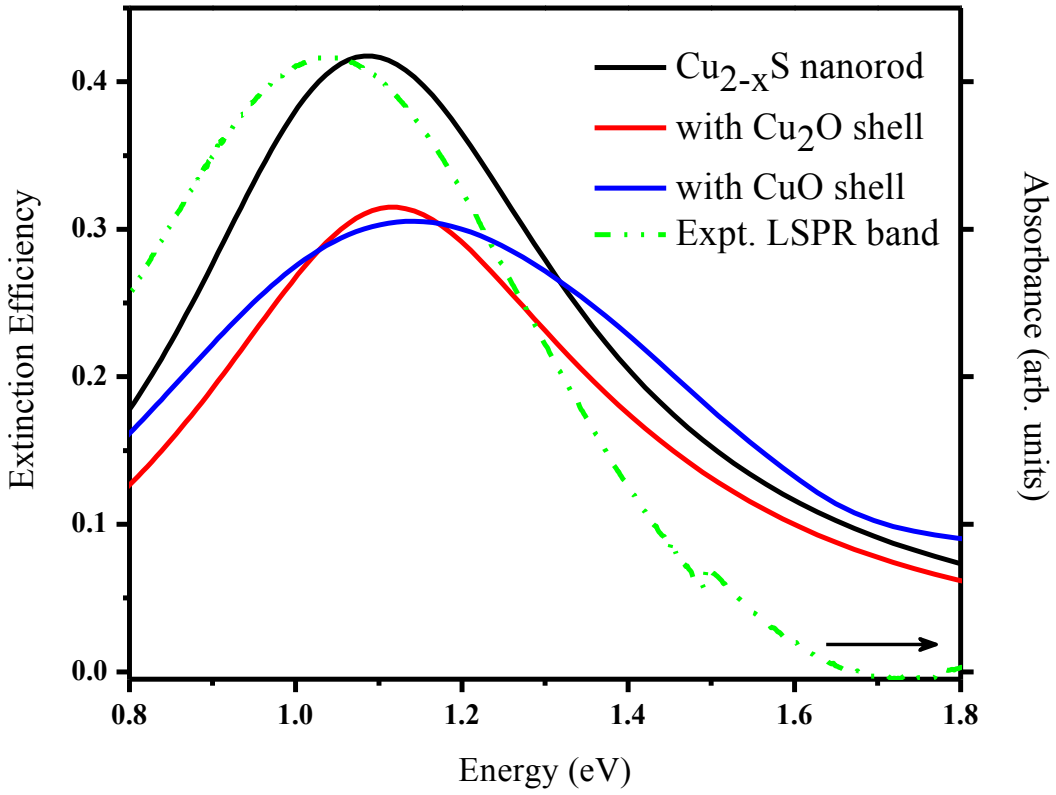

Figure A.4.5. Effect of copper oxide shell on LSPR spectra of copper(I) sulfide nanorods. Extinction efficiency spectra of $Cu_{2-x}S$ nanorods calculated by discrete dipole approximation. Spectra of 4-nm diameter and 40-nm length $Cu_{2-x}S$ nanorods, $Cu_{2-x}S$ nanorods with a 0.25-nm thick shell of Cu_2O, and $Cu_{2-x}S$ rods with a 0.25-nm thick shell of Cu_2O are shown. For comparison, we show the experimental absorbance spectrum of $Cu_{2-x}S$ nanorods exhibiting a band due to the transverse LSPR mode.

In order to probe the effect of a copper oxide shell on the plasmonic properties of copper (I) sulfide, nanorod spectra were calculated using the discrete dipole approximation (DDA) with a 0.25-nm dipole spacing and light polarization along the nanorod short axis. The dielectric function (ε_r+i.ε_i) of the $Cu_{2-x}S$ in the near-infrared (NIR) is dominated by the free carrier contribution, so it can be modeled by the Drude model as follows:

$$\varepsilon_r = \varepsilon_\infty - \frac{\omega_p^2}{\omega^2+\gamma^2} \qquad \text{(A.4.2)}$$

$$\varepsilon_i = \frac{\omega_p^2 \gamma}{\omega(\omega^2+\gamma^2)} \qquad \text{(A.4.3)}$$

where, ε_∞ is the high frequency dielectric function chosen to be 3.[16] The damping constant γ was determined from the FWHM (0.49 eV) of the experimental spectrum fit to a Gaussian. The plasma frequency ω_p was chosen to have a value of 3.13 eV to closely fit the experimental LSPR frequency. ω_p is dependent on the hole density N as per the relation:

$$N = \frac{\omega_p^2 \varepsilon_0 m_h}{e^2} \qquad \text{(A.4.4)}$$

where e is the electronic charge, ε_0 is the free space permittivity, m_h is the hole effective mass in $Cu_{2-x}S$ known to be 0.8 times the free electron mass.[17] The above value of ω_p corresponds to a hole density N of 4.7 x 10^{21} cm^{-3} assuming. This value of N is equivalent to 11% copper vacancies (assuming all vacancies are ionized) resulting in a stoichiometry close to the digenite phase ($Cu_{1.8}S$).

$Cu_{2-x}S$ rods with a 4-nm diameter and 40-nm in length were modeled with and without oxide shells. Nanorods were assumed to have a cylindrical shape. Bulk dielectric functions of Cu_2O and CuO were taken from Ching, Xu, and Wong and used without modification.[18] In thin shells, quantum size effects and surface electron scattering would result in a modified dielectric function. However, these non-trivial corrections were not employed here; therefore, our calculations are not meant to be strictly quantitative. Oxide shells of both Cu_2O and CuO were taken to be 0.25 nm in thickness. This thickness is close to the value of ca. 0.2 nm estimated from the calculated number of copper atoms removed from the $Cu_{2-x}S$ nanorod, based on the copper vacancy concentration of 11%. Upon formation of the thin copper oxide shell, the $Cu_{2-x}S$ nanorod LSPR band increases in linewidth and decreases in intensity but shows only a slight shift to lower energies (0.04 eV in the case of Cu_2O and 0.06 eV in the case of CuO). These changes in the LSPR are simply due to a non-resonant dielectric effect of the copper oxides, both of which have band-to-band transitions in the visible region, far away from the spectral location of the LSPR. A shell of copper iodide, which has its band-edge transition in the visible region (3.1 eV), can be expected to have similar effects on the $Cu_{2-x}S$ LSPR.

A.5. References

(1) Hung, L.-I.; Tsung, C.-K.; Huang, W.; Yang, P. *Adv. Mater.* **2010**, *22*, 1910.

(2) Kuhl, K. P.; Cave, E. R.; Abram, D. N.; Jaramillo, T. F. *Energy Environ. Sci.* **2012**, *5*, 7050.

(3) Gileadi, E. *Physical Electrochemistry: Fundamentals, Techniques and Applications*; 1st ed.; Wiley-VCH: Weinheim, Germany, 2011.

(4) Hussain, I.; Graham, S.; Wang, Z.; Tan, B.; Sherrington, D. C.; Rannard, S. P.; Cooper, A. I.; Brust, M. *J. Am. Chem. Soc.* **2005**, *127*, 16398.

(5) Love, J. C.; Estroff, L. A.; Kriebel, J. K.; Nuzzo, R. G.; Whitesides, G. M. *Chem. Rev.* **2005**, *105*, 1103.

(6) Hori, Y. In *Modern Aspects of Electrochemistry*; Vayenas, C. G.; White, R. E.; Gamboa-Aldeco, M. E., Eds.; Springer: New York, 2008; pp. 89–189.

(7) Chen, Y.; Li, C. W.; Kanan, M. W. *J. Am. Chem. Soc.* **2012**, *134*, 19969.

(8) Meakin, P. *Phys. Lett. A* **1985**, *107A*, 269.

(9) Yella, A.; Tahir, M. N.; Meuer, S.; Zentel, R.; Berger, R.; Panthöfer, M.; Tremel, W. *J. Am. Chem. Soc.* **2009**, *131*, 17566.

(10) Luther, J. M.; Jain, P. K.; Ewers, T.; Alivisatos, A. P. *Nat. Mater.* **2011**, *10*, 361.

(11) Sadtler, B.; Demchenko, D. O.; Zheng, H.; Hughes, S. M.; Merkle, M. G.; Dahmen, U.; Wang, L.; Alivisatos, a P. **2009**, 5285.

(12) Robinson, R. D.; Sadtler, B.; Demchenko, D. O.; Erdonmez, C. K.; Wang, L.-W.; Alivisatos, a P. *Science* **2007**, *317*, 355.

(13) Amalina, M. N.; Rusop, M. *2011 IEEE Symp. Ind. Electron. Appl. ISIEA 2011* **2011**, 440.

(14) Cuya Huaman, J. L.; Sato, K.; Kurita, S.; Matsumoto, T.; Jeyadevan, B. *J. Mater. Chem.* **2011**, *21*, 7062.

(15) Broome, F. K.; Ralston, a. W.; Thornton, M. H. *J. Am. Chem. Soc.* **1946**, *68*, 67.

(16) Rafea, M. A.; Farag, a. a. M.; Roushdy, N. *Mater. Res. Bull.* **2012**, *47*, 257.

(17) Zhao, Y.; Pan, H.; Lou, Y.; Qiu, X.; Zhu, J.; Burda, C. *J. Am. Chem. Soc.* **2009**, *131*, 4253.

(18) Ching, W. Y.; Xu, Y. N.; Wong, K. W. *Phys. Rev. B* **1989**, *40*, 7684.